



National Library
of Canada

Bibliothèque nationale
du Canada

Canadian Theses Service

Service des thèses canadiennes

Ottawa, Canada
K1A 0N4

NOTICE

The quality of this microform is heavily dependent upon the quality of the original thesis submitted for microfilming. Every effort has been made to ensure the highest quality of reproduction possible.

If pages are missing, contact the university which granted the degree.

Some pages may have indistinct print especially if the original pages were typed with a poor typewriter ribbon or if the university sent us an inferior photocopy.

Reproduction in full or in part of this microform is governed by the Canadian Copyright Act, R.S.C. 1970, c. C-30, and subsequent amendments.

AVIS

La qualité de cette microforme dépend grandement de la qualité de la thèse soumise au microfilmage. Nous avons tout fait pour assurer une qualité supérieure de reproduction.

S'il manque des pages, veuillez communiquer avec l'université qui a conféré le grade.

La qualité d'impression de certaines pages peut laisser à désirer, surtout si les pages originales ont été dactylographiées à l'aide d'un ruban usé ou si l'université nous a fait parvenir une photocopie de qualité inférieure.

La reproduction, même partielle, de cette microforme est soumise à la Loi canadienne sur le droit d'auteur, SRC 1970, c. C-30, et ses amendements subséquents.

UNIVERSITY OF ALBERTA

INVESTIGATIONS OF THE PROPERTIES OF SILICON DOPING SUPERLATTICES

BY

KOON HOO TEO



A THESIS

SUBMITTED TO THE FACULTY OF GRADUATE STUDIES AND RESEARCH

IN PARTIAL FULFILMENT OF THE REQUIREMENTS FOR THE DEGREE

OF DOCTOR OF PHILOSOPHY

DEPARTMENT OF ELECTRICAL ENGINEERING

EDMONTON, ALBERTA

FALL 1990



National Library
of Canada

Bibliothèque nationale
du Canada

Canadian Theses Service Service des thèses canadiennes

Ottawa, Canada
K1A 0N4

The author has granted an irrevocable non-exclusive licence allowing the National Library of Canada to reproduce, loan, distribute or sell copies of his/her thesis by any means and in any form or format, making this thesis available to interested persons.

The author retains ownership of the copyright in his/her thesis. Neither the thesis nor substantial extracts from it may be printed or otherwise reproduced without his/her permission.

L'auteur a accordé une licence irrévocable et non exclusive permettant à la Bibliothèque nationale du Canada de reproduire, prêter, distribuer ou vendre des copies de sa thèse de quelque manière et sous quelque forme que ce soit pour mettre des exemplaires de cette thèse à la disposition des personnes intéressées.

L'auteur conserve la propriété du droit d'auteur qui protège sa thèse. Ni la thèse ni des extraits substantiels de celle-ci ne doivent être imprimés ou autrement reproduits sans son autorisation.

ISBN 0-315-64786-8

Canada

UNIVERSITY OF ALBERTA

RELEASE FORM

NAME OF AUTHOR: KOON HOO TEO


TITLE OF THESIS: INVESTIGATION OF THE PROPERTIES OF SILICON DOPING
SUPERLATTICES

DEGREE: DOCTOR OF PHILOSOPHY

YEAR THIS DEGREE GRANTED: FALL 1990

Permission is hereby granted to THE UNIVERSITY OF ALBERTA LIBRARY to reproduce single copies of this thesis and to lend or sell such copies for private, scholarly or scientific research purposes only.

The author reserves other publication rights, and neither the thesis nor extensive extracts from it may be printed or otherwise reproduced without the author's written permission.

..........

#710, 8515 112 Street, Edmonton,
Alberta, Canada T6G 1K7

Date: June 12, 1990

THE UNIVERSITY OF ALBERTA
FACULTY OF GRADUATE STUDIES AND RESEARCH

The undersigned certify that they have read, and recommend to the Faculty of Graduate Studies and Research for acceptance, a thesis entitled INVESTIGATION OF THE PROPERTIES OF SILICON DOPING SUPERLATTICES submitted by KOON HOC TEO in partial fulfilment of the requirements for the degree of DOCTOR OF PHILOSOPHY in ELECTRICAL ENGINEERING.

.....*J.N. McMullin*.....
Dr. J.N. McMullin (Supervisor)

.....*W. Allegretto*.....
Dr. W. Allegretto

.....*M.J. Brett*.....
Dr. M.J. Brett

.....*F.L. Weichman*.....
Dr. F.L. Weichman

.....*I.D. Calder*.....
Dr. I.D. Calder (External Examiner)

Date: *June 12, 1990.*

DEDICATION

To My Late Father

Abstract

Silicon (Si) doping superlattices or nips have been successfully grown by molecular beam epitaxy (MBE) and selective ohmic contacts fabricated using the shadow mask technique. Experimentally, it was determined that the dominant recombination mechanism of the carriers is through the shunting effect due to junction defects or the substrate. The carrier lifetimes can therefore be estimated by taking the product of the junction capacitance and the effective small signal resistance of the nipi structure. Small signal AC measurements at different frequencies were carried out under reverse bias. A simple linear electrical circuit model was developed to interpret the AC characteristics and parameters such as capacitance, doping profile and estimated AC conductance.

Tunabilities of the effective bandgap and carrier concentration in structure with narrow n^+ -doped layers and wide p-doped layers were calculated and found to increase as doping of the n-layers increased or as temperature decreased. The exchange-correlation energy was included in the self-consistent calculation of the subband energies. It was determined that the exchange-correlation term is more important in Si than in GaAs nips. We developed a new method which uses a system of piecewise linear function and "finite box" to calculate self-consistently the density-of-states mass of holes in two-dimensional Si and Ge doping superlattices. It was determined that the doping level of the p-type layers is the leading parameter that affects the hole mass characteristics.

ACKNOWLEDGEMENTS

I wish to express my appreciation of and respect for Dr. J.N. McMullin and Dr. H.G. Schmidt-Weinmar for their active interest, advice and strong encouragement during the course of this work. I wish to also express my appreciation to the members of the examining committee for examining this work.

This project is the product of the joint effort of many individuals at the University of Alberta and the Division of Microstructural Science of the National Research Council in Ottawa. The accomplishments of this project would not be possible without the material and moral support that have been given to me by a great number of people. I would like to extend my words of thanks to the following people (in alphabetical order):

Dr. W. Allegretto (U. of A.) for his contribution in generating the method of piecewise linear function and finite box to calculate self-consistently the masses of holes, and also for his frequent advice and supervision in the process of working on the complex hole problem.

Dr. M.A. Buchanan (NRC) for her supervision and participation in this project, and also for her noted contribution in developing a suitable processing procedure for the mesa contacts.

P. Chow-Chong (NRC) for his skillful lithography processing work.

Dr. M.W. Denhoff (NRC) for the countless hours he put into the MBE growth of the doping superlattices and his noted contribution of designing the tantalum shims that separates the shadow mask from the wafer during oxide removal.

Dr. C. Dharma-wardana (NRC) for discussions and critical reading of our manuscripts on the hole problems.

Dr. D. Houghton (NRC) for project supervision.

Dr. T.E. Jackman (NRC) and Dr. J.A. Jackman (CANMET) for their contribution in the SIMS analysis.

Dr. P. Janega (NRC) for ohmic contact research and processing.

Dr. E. Kornelson (NRC) for project supervision.

Dr. D. Landheer (NRC) for his active supervision and participations in this project, and also for his noted contribution to the works in carrier lifetimes, absorption measurements and selective contacts of the superlattices.

P. Marshall (NRC) for microbonding and other technical assistance.

K. Marsh (U. of A.) for his technical assistance and moral support.

Dr. N.L. Rowell (NRC) for carrying out some initial photoluminescence measurements.

Dr. J.B. Webb (NRC) for supervision in the DLTS measurements.

Dr. F.L. Weichman (U. of A.) for his close supervision and active participation in the absorption and lifetime measurements, and also for his countless advice in the measurement techniques and the design and building of the photon counter.

Prof. S.X. Zhou (Fudan University) for critical reading of our manuscripts on the hole problems.

Dr. S. Zukotynski (U. of Toronto) for some DLTS measurements and discussions in the carrier lifetimes of superlattices.

I also wish to express my deepest gratitude to my research colleague, G.H. McKinnon for helping to establish the necessary ground work, and in particular the shadow mask, for the fabrication of the Si doping superlattices

My thanks are also extended to the Killam Trustees, the University of Alberta and the Scholarship Committee for the Izaak Walton Killam Memorial Scholarship and the Andrew Stewart Graduate Prize which have provided me and my family the much needed financial support. In addition this project is also supported by the Natural Sciences and Engineering Research Council of Canada.

TABLE OF CONTENTS

CHAPTER	PAGE
1. Introduction	1
2. Doping Superlattices: A Review	8
2.1 Basic Principles	10
2.1.1 Two Dimensional Properties	11
2.1.2 Carriers Lifetimes	17
2.2 Fabrication	19
2.2.1 Crystal Growth with Molecular Beam Epitaxy	19
2.2.2 Selective Ohmic Contacts	21
2.3 Electrical Properties	24
2.3.1 DC Characteristics	24
2.3.2 Tunable Conductivity	26
2.4 Optical Properties	29
2.4.1 Tunable Absorption Coefficients	29
2.4.2 Tunable Luminescence	33
3. Recombination Mechanisms and Carrier Lifetimes	37
3.1 Calculation of the Carrier Lifetimes	37
3.2 Experimental Results	41
3.2.1 Capacitance Measurement	42
3.2.2 Carriers Lifetimes Measurement by Photoconductivity Method	44
3.3 Discussion	49
4. Steady State Small Signal AC Analysis	50
4.1 Linear Electrical Lumped Circuit Model	51

4.2 AC Characteristics under Reversed Bias	56
4.2.1 Capacitance	57
4.2.2 AC Resistance	61
4.3 Experimental Results and Discussion	62
5. Two-Dimensional Properties of Electrons	75
5.1 Tuning the Effective Bandgap	76
5.1.1 Potential Wells in a Doping Superlattice	77
5.1.2 Calculation of the Self-Consistent Potential and the Tunability	80
5.1.3 Results and Discussion	87
5.2 Exchange-Correlation Energy in the Subbands	94
5.2.1 Freezing out of the Donors	95
5.2.2 Self-Consistent Calculations	97
5.2.3 Results and Discussion	98
6. Density-of-States Masses of Holes	107
6.1 Freezing out of the Acceptors	109
6.2 Method of Computation	111
6.3 Density-of-States Masses	118
6.3 Results and Discussion	119
7. Conclusions	143
8. References	149
9. Appendix A	155
Appendix B	156
10. Vitae	157

LIST OF TABLES

TABLE	PAGE
4.1 The values of the discrete circuit elements for cases A to G.	58
4.2 Values of the discrete circuit elements for samples 405B and 405C.	70
5.1 The exchange-correlation correction to the subband energies for different values of electron concentration in a pn^+p doping superlattice.	105
5.2 Same as Table 5.1 except for $pnpn$ and $nipi$ doping superlattices.	106
6.1 Doping levels for the formation and merging of the impurity bands.	110
6.2 Density-of-States masses in a (110) germanium doping superlattice with different doping level of the n-type bulk and for two different thicknesses of the p-type layers.	140

LIST OF FIGURES

FIGURE	PAGE
2.1 Composite and a doping superlattices.	9
2.2 Band diagram of a doping superlattice in real space.	12
2.3 A doping superlattice under external excitation.	15
2.4 A doping superlattice with selective contacts.	23
2.5 A doping superlattice with split selective contacts.	25
2.6 A doping superlattice with sandwiched contacts.	31
2.7 A real-space band diagram of a doping superlattice with sandwiched contacts.	32
2.8 A real-space band diagram of a hetero doping superlattice.	34
3.1 Equivalent circuit of a silicon nipi with external bias.	40
3.2 Circuit to measure $dn^{(2)}/dU$.	43
3.3 Schematic of carrier lifetime measurements.	45
3.4 Carrier lifetime as a function of bias at $T = 80^{\circ}\text{K}$.	47
3.5 Carrier lifetime as a function of temperature.	48
4.1 Electrical model for a diode under reverse bias.	52
4.2 Lumped electrical model for a doping superlattice.	53
4.3 Net equivalent circuit of a doping superlattice.	55
4.4 Calculated capacitance characteristics.	59
4.5 Calculated AC resistance characteristics.	60
4.6 Equivalent parallel capacitance and AC serial resistance as a function of frequency for sample 405B.	64

4.7	Equivalent parallel capacitance as function of reverse bias at different frequency for sample 405C.	65
4.8	Equivalent parallel AC resistance as function of reverse bias at different frequency for sample 405C.	66
4.9	Equivalent serial capacitance as function of reverse bias at different frequency for sample 405C.	67
4.10	Equivalent serial AC resistance as function of reverse bias at different frequency for sample 405C.	68
4.11	SIMS profile of a sample from wafer 405	72
4.12	Experimental DLTS spectra for traps	73
5.1	A doping superlattice structure with selective contacts for external biasing.	78
5.2	Energy diagram for a silicon doping superlattice.	81
5.3	Two-dimensional energy state densities of electrons.	84
5.4	Effective bandgap in a silicon doping superlattice.	88
5.5	Energy of subband edges versus the external bias.	90
5.6	Tunability of the effective bandgap as a function of the thickness of the n-doped layer.	91
5.7	Tunability of the effective bandgap as a function of the planar donor charge density.	92
5.8	Tunability of the effective bandgap as a function of temperature.	93
5.9	Subband energies calculated with and without the exchange energy in a Si pn^+p doping superlattice.	101
5.10	Subband energies calculated with and without the	

exchange energy in a GaAs pn^+p doping superlattice.	102
5.11 Self-consistent potential in a Si pn^+p .	103
5.12 Self-consistent potential in a GaAs pn^+p .	104
6.1 Piecewise linear function of ψ .	115
6.2 Density-of-states masses of a (110) Si MOS.	120
6.3 Density-of-states masses of a (100) Si MOS.	121
6.4 Self-consistent electric potential for (100) MOS.	122
6.5 Fermi contours for (100) MOS.	123
6.6 Electric potentials for a Si nipi.	125
6.7 Subband energies for a (110) Si nipi.	126
6.8 Subband energies for a (100) Si nipi.	127
6.9 Hole subband dispersions for a (110) Si nipi.	129
6.10 Hole subband dispersions for a (100) Si nipi.	130
6.11 Density-of-states masses of hole for (110) and (100) Si nipsis.	131
6.12 Density-of-states masses as function of thickness of p-type layers for (110) and (100) Si nipsis.	133
6.13 Density-of-states masses as function of doping level of p-type layers for (110) and (100) Si nipsis.	134
6.14 Subband energies for a (110) Ge nipi.	135
6.15 Density-of-states masses for (110) and (100) Ge nipsis.	137
6.16 Density-of-states masses as function of thickness of p-type layers for (110) and (100) Ge nipsis.	138
6.17 Density-of-states masses as function of doping level of p-type layers for (110) and (100) Ge nipsis.	139

LIST OF SYMBOLS

A_i	area of the i th Fermi contour
a	doping gradient
a^*	effective Bohr radius
C_{dpl}	depletion capacitance of superlattice
C_j	junction capacitance of p-n junction
C_j	lumped depletion capacitance of p-n junction
D_{ij}	density of states of the j th subband of the i th subband set
d_p, d_n	thickness of p-layer, n-layer
e	electronic charge
E_g^o	bulk energy bandgap
$E_g^{eff,1}$	effective bandgap
E_v, E_c	energy level of valence, conduction band
E_{ij}	j th subband energy of the i th set
E_{Fp}, E_{Fn}	Fermi energy with respect to the valence, conduction band edge
h	Plank's constant
I_{pp}, I_{nn}	currents in p-layers, n-layers
k_B	Boltzmann's constant
k	wave vector
m_o	free electron mass
m^*	effective mass of electrons or holes
m_l^*	density-of-states mass of the i th hole subband
n_i	intrinsic carrier concentration

n_{ij}	two-dimensional electron concentration for the j th subband of the i th subband set
$n^{(2)}, p^{(2)}$	two-dimensional density of electrons, holes
N	number of elements in a lumped circuit model
N_A, N_D	acceptor, donor concentration
P_I	doping concentration
r_o	Bohr radius
R_c	contact resistance
R_{cs}	resistance of the non-depletion regions of the n - and p -layers
R_{ext}	external resistance
R_i	$R_p R_n / (R_p + R_n)$
R_ℓ	lumped p - n junction AC resistance
R_p, R_n	lumped AC serial resistance of p -layers, n -layers
R_L	AC junction leakage resistance
R_{LS}	AC shunting leakage resistance
T_B, T_E	Tunablility of the effective bandgap, carrier concentration
U	external bias in volts
V_b	bare potential
V_{bi}	built-in potential in eV
V_{ex}	exchange-correlation potential
V_H	Hartree potential
V_{ss}	steady-state voltage
V_U	potential of the superlattice barrier
V^{exc}	potential of the superlattice barrier under excitation

z_A, z_D	maximum depletion width in p-layers, n-layers
α	occupancy factor
ϵ	dielectric constant
ψ_{ij}	envelope wavefunction of electrons or holes of the jth subband of the ith subband set
ϕ_p, ϕ_n	quasi Fermi level
τ	carrier recombination lifetime
τ_o	bulk carrier recombination lifetime
τ_{nipi}^{tun}	recombination lifetime via tunneling
τ_{nipi}^{th}	recombination lifetime via thermionic emission
μ_p, μ_n	electron, hole mobility

Chapter 1

Introduction

The development of semiconductor devices has made remarkable progress during the past three decades. The first semiconductor materials extensively used for commercial application were germanium (Ge) and silicon (Si). While Ge was initially the most commonly used material, the better temperature performance of Si coupled with its ability to dope small regions selectively provided advantages which led to becoming the material of choice for semiconductors. These advantages also allowed Si integrated circuits to progress from those in 1962, which contained a few transistors, to the circuits we have today, which may contain more than a million transistors.

Almost as significant as the invention and technological development of the transistor, was the invention of the semiconductor laser two decades ago. Semiconductor lasers provide light for today's information transmission. These lasers are not made from Si but from III-V compound semiconductors. In contrast to Si and Ge, many of the III-V compounds such as GaAs have a "direct bandgap", which leads to efficient electron-hole generation and radiative recombination. The high carrier mobility in GaAs has promoted the development of many high speed devices based on this material [1]. In addition, it is possible to achieve nearly perfect single crystal growth of layered structures with III-V compounds, particularly when their lattice constants are about the same.

For the last one and a half decades or so, there have been a number of surprising advances in the design of crystalline

semiconductor heterostructures with a specified bandgap. Due to the spectacular progress made, generally in fabrication technology, (particularly that of the Molecular Beam Epitaxy (MBE) technique), the thickness of deposited crystalline layers has been reduced to the order of 10\AA for the composite superlattices [2] and "sheet charges" as high as 10^{13}cm^{-2} have been achieved in the delta-doped superlattice structures [3]. Due to the mature III-V compound MBE technique, extensive studies on III-V superlattices have been made possible. Many new effects and properties such as negative resistance (as predicted by L. Esaki and Tsu in 1970 [4]), quantum size effect, tunable bandgaps, and increased carrier mobility were reported and experimentally verified by a number of research scientists [5,6] and by G.H. Döhler on the doping superlattice in particular [7]. These findings have motivated the development of a number of new devices such as the HEMT (high electron mobility transistor) [1], the quantum well laser [8], the resonant tunneling diode [9], the SEED (self electro-optic effect device) [10], and the stair-case avalanche photodetector [11].

The rapid progress in the MBE technique during the last decade led to the fabrication of strained layer superlattices in which the constituent semiconductor lattices, for example Si and Ge, do not match [2]. Work on strained layer heterostructures (composite superlattices), which initially began with the GaAs-GaAsP system, has recently been expanded to include Si-Ge systems, although these had already been suggested by Esaki and Tsu as early as 1970. Since the bandgap of Ge is smaller than the bandgap of Si, such structures provide the possibility of "bandgap engineering" towards the development of novel long wavelength photodetectors in silicon-based technology [12].

The doping superlattices, sometimes known as the nipi (a periodic sequence of layers of n-type, intrinsic, p-type, intrinsic material), were first studied by Döhler in 1972 [13]. Unlike the compositional semiconductor superlattices, the nipi has only one host material. The problems of strained layers can hence be disregarded. Research on this system first began with GaAs [14]. However, the possibility of combining novel electrical and optical properties of doping superlattices in a large-scale integrated circuit on Si substrates makes investigation into Si doping superlattices highly attractive. With the recent progress made in Si MBE, whereby slow growth rate and precise doping control are now possible [15], theoretical and experimental work on Si doping superlattices has begun [6,16,17]. Unlike GaAs, bulk Si has non-isotropic effective mass electrons and an indirect bandgap in k-space. As a result, the analysis of a Si doping superlattice is generally more complicated than its GaAs counterpart.

This work in the investigation of the properties of Si doping superlattices involved the collaboration of the University of Alberta and the Division of Microstructural Science at the National Research Council (NRC) in Ottawa. We first reported our self-consistent calculations of the subband energies in 1986 [16] and 1987 [18]. During the same period, studies of similar nature had been carried out independently by Wang et al. [17] and Priester et al. [19]. Subsequently, we have also included the exchange-correlation energy in the self-consistent calculations of the electron subband energies [20]. We developed a new method to calculate two-dimensional hole subband energies [21] and to determine the density-of-states masses of holes

[22]. The first experimental work in Si doping superlattices was reported by Nakagawa and Shiraki on enhanced carrier mobility [6]. Since then, the results of a number of studies have been published, such as our work on fabrications [23], absorption coefficients [24,25], selective contacts, DC characteristics [25,26], and carrier lifetimes [27,28] of Si doping superlattices. Experimental work by other groups on carrier lifetimes [29] and photoluminescence spectra has also been reported [30].

The history of this project is as follows. The project began with the objective of investigating the carrier lifetimes in a Si doping superlattice. According to Döhler's theory, recombination of carriers at low temperature depends on the extent of the overlapping of the electron and hole envelope wavefunctions. Therefore we were required first to investigate theoretically the two-dimensional properties of electrons and holes of a Si doping superlattice (which we began while the MBE system was being set up at NRC). After the first successful growth of a Si doping superlattice by the NRC, we proceeded with the design and creation of the selective ohmic contacts, which in fact turned out to be more complicated and time-consuming than initially anticipated. A novel method of making good selective contacts, known as the shadow mask technique, was first introduced by Döhler [31] on a GaAs doping superlattice. In collaboration with the NRC, we employed this method to make good selective contacts on Si doping superlattices. With good selective ohmic contacts, measurements of optical absorptions and carrier lifetimes were made by the photoconductivity method, as well as measurements on the DC characteristics of the doping superlattice were carried out. Our experimental work with

photoconductivity showed no noticeable difference in absorption characteristics from the bulk. This result caused us to change our initial plan to work on photoluminescence, for which we had already been building a photon counter to detect optical energy of wavelengths of up to $1.5\text{ }\mu\text{m}$. Our experimental results on the carrier lifetimes indicated that the dominant recombination mechanism of the carriers were not through the overlapping of electron and hole wavefunctions. Consequently, the study of the two-dimensional properties of holes took a new direction, concentrating instead on an investigation of the masses of holes as a function of the physical parameters of the doping superlattice. Since traps may influence the carrier lifetimes in a doping superlattice, attempts were made to measure the traps with the Deep Level Transient Spectroscopy (DLTS). As DLTS is basically a capacitance transient measurement technique, the experiment calls for a better understanding of the nature of the capacitances in the Si doping superlattice. As a result we were led to the study of the AC characteristics of the doping superlattice [32]. Our DLTS measurements have so far led to no conclusive results.

This thesis is basically a continuation of G.H. McKinnon's M.Sc. thesis [25], where some of the properties of Si doping superlattices have already been reported. In general, this thesis is organised as follows: Chapter 2 begins with a review of the basic principles about doping superlattices and their development in general. Particular attention is given to the GaAs doping superlattice, as it was the first to be studied and hence there are far more experimental and theoretical results associated with it. Also outlined is the time-consuming ground work of growing, designing and testing of the Si doping superlattices

with their selective ohmic contacts. Experimental and theoretical work that has been carried out on Si doping superlattices by our group is briefly mentioned in order to compare it with that which has already been done for the GaAs doping superlattice.

Chapter 3 deals with the measurement of the carrier lifetime in a Si doping superlattice by the photoconductivity method. The lifetimes, as a function of external bias and temperature, were measured and the results compared with the calculated values, estimated by using a simple diode equivalent circuit model.

Chapter 4 discusses the AC characteristics of doping superlattices with selective ohmic contacts and how they can be better understood with the help of a lumped circuit model. A simple linear electrical circuit model is developed. Small signal AC measurements at different frequencies were made under reverse bias. Parameters such as capacitance, doping profile and AC conductance of a doping superlattice are estimated.

Chapter 5 examines the tunability of the effective bandgap and carrier concentration in a Si doping superlattice with narrow n^+ -doped and wide p-doped layers. Quantitative tunability parameters are defined and their variation with dopant concentration and temperature are calculated self-consistently in the effective mass and Hartree approximations. The effect of the exchange-correlation energy on the subband energies are also studied at zero temperature. The self-consistent calculations of the energy subbands in three types (pn^+p , $pnpn$, $nipi$) of Si and GaAs doping superlattices are described.

Finally, Chapter 6 discusses the two-dimensional properties of holes in Si and Ge doping superlattices. We have developed a new

method for the self-consistent calculation of the density-of-states mass of holes for two-dimensional Si structures. The final part of the chapter investigates the masses of holes as a function of the physical parameters of both the Si and Ge doping superlattices. Superlattices with narrow p^+ -doped layers and wide n-doped layers are assumed in this analysis.

Chapter 2

Doping Superlattices: A Brief Review

Research on synthesized semiconductor superlattices was first started by Esaki and Tsu [4] in 1969-1970. It was theoretically shown that such a man-made system possesses unusual electronic and optical properties not seen in the host bulk semiconductors. These arise basically from the two-dimensional properties of the carriers, as well as from the quantum effect introduced by the very narrow potential well along the z direction. These periodic narrow potential wells of the superlattice may modify or perturb the band structure of the host materials. The extent of this modification will very much depend on the amplitude and periodicity of the potential. Similar to the lattice potential that creates the well-known Brillouin Zones in the bulk semiconductor, the superlattice periodic potential is responsible for the formation of subbands. The advantage of a superlattice is that its configuration, such as the period and the choice of materials, determines the structure of the subbands, which in turn dictates the electrical and optical properties.

Although Esaki and Tsu started out by classifying semiconductor superlattices into two main categories, doping and compositional, as shown in Figure 2.1, preference was given to the latter. This is because of the disadvantages attributed to the dopants as free carrier scattering centers and the practical problem of fabricating doping superlattices without serious diffusion of impurities. The latter disadvantage, however, has been overcome with advancements in molecular beam epitaxy technology. In 1972, Döhler [13] carried out

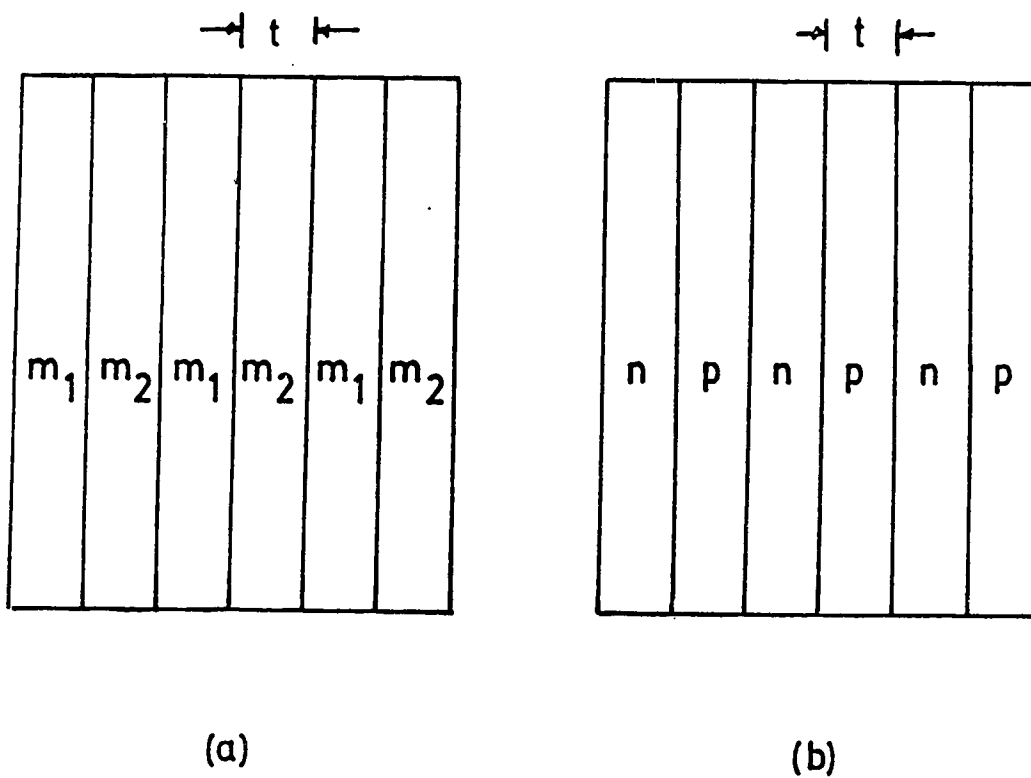


Fig. 2.1 Cross sectional view of (a) a composite superlattice and (b) a doping superlattice. m_1 and m_2 denote material of two different kind while n and p represent layer which are n- and p-doped, respectively. The thickness t ranges from 10\AA to 2000\AA .

detailed theoretical analysis of a doping superlattice and concluded that not only can two-dimensional subbands be obtained from such a structure but that it can also show very novel electronic and optical properties. As in the composite superlattices, a doping superlattice has the feature that electrical and optical properties can be "tailored". In addition, doping superlattices are unique in that some of these properties can be tuned. Döhler has identified "primary" and "secondary" tunability [33]. The tunability of the carrier concentrations, the carrier lifetimes, and the effective bandgap are considered primary. These lead to secondary tunability in quantities such as conductivity, luminescence spectra, absorption, and refractive index. The term "tunability" means that the electrical or optical behaviour of a given sample of doping superlattice can be varied over a wide range by external means. The term "tailoring" implies the setting of material parameters of superlattices by proper choice of the values of parameters such as doping level and layer thickness. Besides these parameters, there is the flexibility of using almost any semiconductor as the host material, which unlike the composite superlattice, is not limited by the lattice matching problem.

2.1 Basic Principles

The doping superlattice or nipi is a crystal semiconductor which consists of many alternate ultrathin layers of an n-doped, intrinsic and p-doped semiconductor. In most cases considered in this thesis, the undoped (or intrinsic) layers have zero thickness, so strictly speaking the superlattice should not be called a nipi. However, the principle behind the analysis of the two structures in question is

similar, with the only difference being in the formulation of the space charge potential.

2.1.1 Two Dimensional Properties

Assume a semiconductor with a static dielectric constant ϵ and a bandgap E_g^0 , which is modulated by periodic n- and p-doping in the z direction. Assume also that the doping in each layer is constant and that there are equal doping concentrations, $N_A = N_D$, within the p- and n-doped regions of thickness $d_p = d_n = d/2$. If all impurities are ionized in the ground state due to the recombination of the electrons from donors with the holes from the acceptors, a periodic parabolic space charge potential $V_0(z)$ is created whose amplitude is given by (see Figure 2.2) [34],

$$V_0 = \left(\frac{e N_D}{\epsilon} \right) \left(\frac{d}{4} \right)^2 \quad (2.1)$$

The motion of the charge carriers in the z direction is spatially restricted by this superlattice potential $V_0(z)$. In fact, if these wells are sufficient isolated, this motion becomes "quantized" giving discrete values of momentum in the z direction.

In the bulk semiconductor, the bandgap E_g^0 is determined by the material. Here, however, because of the potential wells given by (2.1), the effective bandgap $E_g^{\text{eff},1}$ is given by the difference between the bottom of the lowest conduction subband at the energy $E_{c,1}$ above the conduction band minimum and the top of the uppermost valence subband at $E_{v,1}$ below the valence maximum; this results in (see

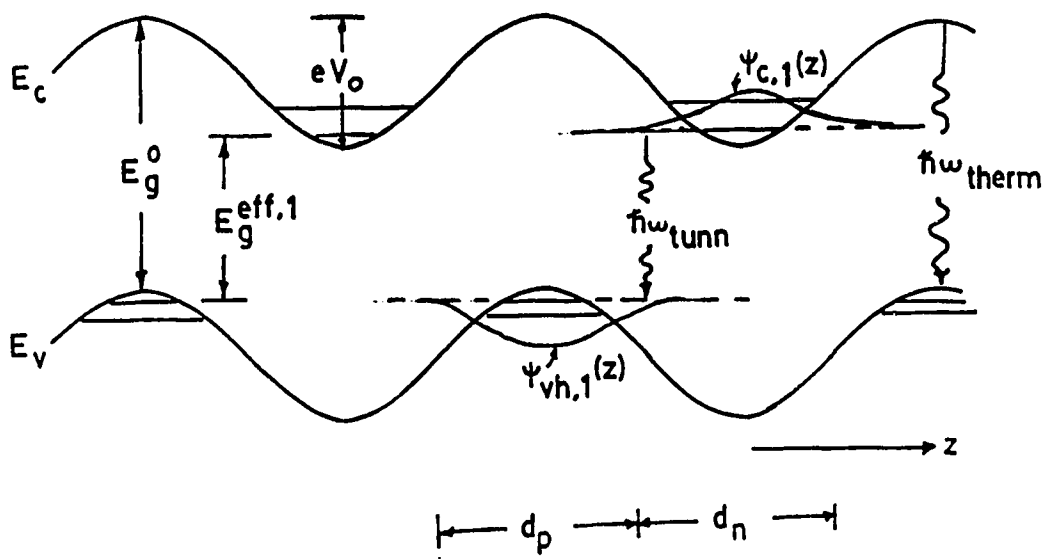


Fig. 2.2 The band diagram of a doping superlattice in real space [33].

Figure 2.2.

$$E_g^{eff,1} = E_g^0 - eV_0 + E_{c,1} + |E_{v,1}| \quad (2.2)$$

If the parabolic well shown in Figure 2.2 can be approximated by a harmonic oscillator, where in general,

$$V(z) = Cz^2/2 \quad (2.3)$$

and

$$E_j = (j - 1/2)\hbar\omega_0 \quad (2.4)$$

with $j = 1, 2, 3 \dots$, and

$$\omega_0 = (C/m^*)^{1/2} \quad (2.5)$$

then using (2.1), (2.3) to (2.5), we obtain

$$\omega_0 = \left(\frac{e^2 N_D}{\epsilon m_e^*} \right)^{1/2} \quad (2.6)$$

and

$$E_{c,j} = \hbar \left(\frac{e^2 N_D}{\epsilon m_e^*} \right)^{1/2} (j-1/2) \quad (2.7)$$

$$E_{v,\mu,\nu} = \hbar \left(\frac{e^2 N_A}{\epsilon m_{\mu,h}^*} \right)^{1/2} (\nu - 1/2) \quad (2.8)$$

where $j = 1, 2, 3, \dots$, and $\nu = 1, 2, 3, \dots$, and $E_{c,j}$ and $E_{v,\mu,\nu}$ are the energy eigenvalues of the electrons and holes, respectively, in a parabolic well. m_e^* is the conduction band electron mass and $m_{\mu,h}^*$ is the light or heavy hole (i.e., $\mu = l$ or h) valence band mass.

From Figure 2.2, it can be seen that $E_g^{\text{eff},1}$ represents an indirect gap in real space since the electron states are shifted by one-half a superlattice period with respect to the hole states. This property implies the possible physical isolation of electrons from the holes and generally at low temperature, recombination will only take place via tunneling of the carriers through the potential barriers.

As the subbands are populated by charge carriers, the electric field of the carriers strongly modifies the "bare" space charge potential $V_0(z)$ of the impurities. The result is a strong change of the amplitude V^{exc} of the space charge potential (see Figure 2.3), due to a compensation of, for example, the positive donor space charges by the negatively charged electrons in the n-layers. The same also applies to holes in the p-layers. This results in a change of the effective bandgap energy $E_g^{\text{eff},1}$. In other words, by variation of the number of free electrons and holes per layer, one can modulate or "tune" the effective bandgap $E_g^{\text{eff},1}$ of the nipi crystal. A computation of the effect on the space charge by the mobile charge carriers can be done using wave mechanics.

Using the effective mass approximation, Schrödinger's equation is given by:

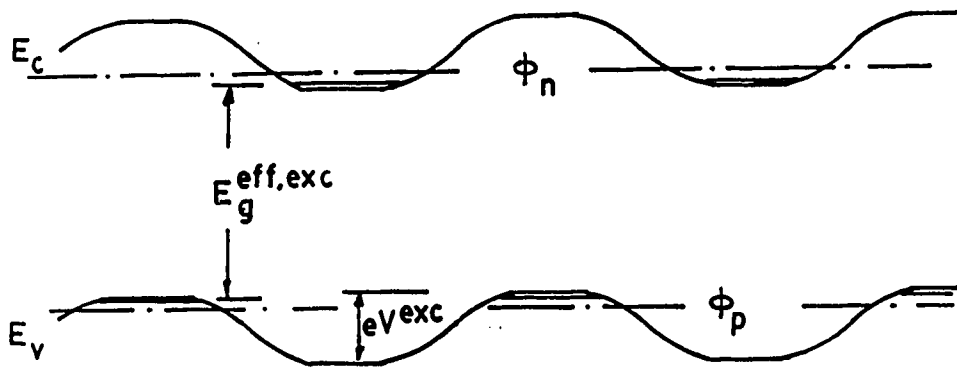


Fig. 2.3 A doped superlattice which is being excited by external optical or electrical energy. ϕ_n and ϕ_p are the quasi-Fermi energies of the electrons and holes, respectively [33].

$$\left\{ - \left(\frac{\hbar^2}{2m^*} \right) \left(\frac{\partial^2}{\partial z^2} \right) + eV_0(z) + eV_H(z) \right\} \psi_j(z) = E_j \psi_j(z) \quad (2.9)$$

Here, $V_0(z)$ represents the space charge potential, and m^* is the effective mass of the charge carrier. $V_H(z)$ is given by:

$$\frac{\partial^2 V_H(z)}{\partial z^2} = - \frac{en(z)}{\epsilon} \quad (2.10)$$

subject to the boundary condition

$$\left. \frac{\partial V_H(z)}{\partial z} \right|_{z=0} = 0 \quad (2.11)$$

and

$$V_H(0) = 0 \quad (2.12)$$

and

$$n(z) = \sum_{\substack{\text{occupied} \\ \text{subbands}}} n_j^{(2)} |\psi_j(z)|^2 \quad (2.13)$$

where $n_j^{(2)}$ is the two dimensional charge carrier concentration in the j th subband. At $T = 0^\circ\text{K}$, $n_j^{(2)}$ may be determined by the fact that all populated subbands have the same Fermi energy:

$$E_j + 2\pi n_j^{(2)} \left(\frac{\hbar^2}{2m^*} \right) = E_1 + 2\pi n_1^{(2)} \left(\frac{\hbar^2}{2m^*} \right) \quad (2.14)$$

where the effective mass, m^* of the charge carriers, is assumed isotropic, and motion in the x and y directions unrestricted.

Equations (2.9) and (2.10) have to be solved self-consistently as changes in $n(z)$ affect $V_H(z)$, which then influences the solutions for E_j , which in turn affects the electron distribution among the subbands, and thus the cycle repeats itself. In other words, the amount of carrier concentration $n(z)$ determines E_j and $V_H(z)$, which in turn determine the effective bandgap of the nipi crystal; the bandgap is "tunable".

The above discussions are applicable to a material such as GaAs where the effective mass of the electrons is isotropic. As for the two-dimensional properties of a Si doping superlattice, the problem is complicated by the multi-valley band structure and the non-isotropic effective mass of the electrons. The calculation of the hole subband energies is even more complicated by the complex hole band structure. The results of our calculations of the electron and hole subband energies are presented in Chapters 5 and 6.

2.1.2 Carriers Lifetimes

If the subbands are populated with charge carriers, then the electron wavefunctions have only an exponentially small overlap with the hole wavefunctions. Hence, in principle, the electron-hole recombination time can be very long. Its duration will depend on the width and the height of the potential barriers created by the space charge potential. In short, carrier lifetime becomes dependent on the "design parameters" of the doping superlattice.

In general, the lifetimes of the carriers are not infinite in duration; rather, these carriers can recombine either by tunneling through or, at higher temperatures, by thermal excitation over the

potential barrier, as shown in Figure 2.2.

A detailed numerical model of electron-hole recombination lifetimes in nipi superlattices has been developed by Clark et al. [35] but Döhler gave an approximate expression for the lifetime due to tunneling recombination as [34]

$$\frac{\tau_{\text{tun}}^{\text{nipi}}}{\tau^{\text{bulk}}} \cong \exp \left[\frac{4eV^{\text{exc}}}{\hbar(\omega_c + \omega_{\text{vh}})} \right] \quad (2.15)$$

where $\omega_c = \omega_o$ is given by (2.6) and

$$\omega_{\text{vh}} = \left(\frac{e^2 N_A}{\epsilon m_{\mu, h}} \right)^{1/2} \quad (2.16)$$

where m_c and $m_{\mu, h}$ are the isotropic effective masses of electrons and holes respectively, and V^{exc} is the effective potential in the excited state as shown in Figure 2.3. Whether light or heavy holes should be used will depend on the host material used and the temperature [34].

Döhler also gave an approximate expression for the recombination lifetime by thermally excited carriers for a given temperature,

$$\frac{\tau_{\text{th}}^{\text{nipi}}}{\tau^{\text{bulk}}} \cong \exp \left[\frac{eV^{\text{exc}}}{k_B T} \right], \quad (2.17)$$

Equations (2.15) and (2.17) imply that the lifetimes are exponentially dependent on V^{exc} , which can be tuned by external bias. Tunneling

recombination dominates when $k_B T$ is less than $\hbar(\omega_c + \omega_{vh})/4$. This also implies that this condition is in part dependent on the doping levels of the layers and independent of v^{exc} .

Lifetimes of the carriers as large as 10^3 sec ($T = 4.2^\circ K$) and 400 ns ($T = 120^\circ K$) for GaAs [36] and PbTe [37] respectively, have been reported. They are in fairly good agreement with theory.

Carrier lifetimes measurements were carried out independently by us at the University of Alberta [28] and by Leith at the University of Toronto [29]. Lifetimes of about 1 sec. were reported by both groups. The carrier lifetime measurement, carried out by our group, is reported in greater detail in Chapter 3.

2.2 Fabrication

2.2.1 Crystal Growth with Molecular Beam Epitaxy Technique

The first GaAs doping superlattice was grown by the MBE technique using Si and Be as dopants [38]. The technique of MBE has a number of special and rather unique features. It is by far one of the most established and reliable methods in satisfying the stringent requirements of a superlattice. The relatively low growth temperature minimizes the effect of diffusion and the slow growth rate greatly contributes to the much-needed precise thickness control. MBE also offers convenience in introducing various beams for compositional modulation. Basically, thermal or ion beams of atoms or molecules are directed at and react on a heated substrate in an ultra-high vacuum environment. MBE is a controlled and reproducible process by which epitaxial layers with thicknesses and doping profiles on the scale of atomic dimensions can be grown. Detailed information on this technique

is eloquently described by Cho [39], L.L. Chang [40], Ploog et al. [38], and Houghton et al. [41].

Zwacknagl et al. also reported the growth of GaAs nips by liquid phase epitaxy (LPE) [42], with Ge and Sn as dopants, where layers as thin as 200Å were fabricated. Hot wall epitaxy (HWE) was also employed for the fabrication of PbTe nipi by Kinoshita et al. [43] and by Clemens et al. [44]. As Bwell, nips of different host materials, grown with different techniques, have been reported; for example, InP by vapor-phase epitaxy (VPE) [45], InGaAs and GaAs by organometallic vapor-phase epitaxy (OMVPE) [46] and Si by MBE [41]. To date no comparative study has been made on the quality of the samples fabricated by these different growth techniques.

In the case of our Si nips, the epilayers were grown in a V.G. Semicon V80 Si MBE system at the National Research Council in Ottawa [23]. B_2O_3 coevaporated from a standard V.G. silicon nitride crucible was used to make boron doped p-layers and a V.G. semicon IBD-100 ion beam unit was used to produce 500 eV As^+ ions for n-doping. The substrates used, n-type (100) Si wafers, were given a 50 minute ultra-violet ozone treatment to remove carbon contamination before placement in the ultra-high vacuum system. The oxide was removed by heating the substrate to 900°C at pressures typically $< 10^{-9}$ torr. The substrate was then cooled to growth temperature and deposition proceeded at a typical rate of 0.3 nm/s. It was experimentally determined that the growth temperature of 650°C could be used to maintain an abrupt boron doping profile and to achieve low defect levels. Shutters on the doping sources were activated to create the doped layers. Secondary Ion Mass Spectrometer (SIMS) measurements

indicated that the rise and fall of doping concentration is smaller than 20 nm/decade.

Si nips were also grown independently by another group at the University of California. They used the solid phase epitaxy technique for the growth of the crystal and Ga and Sb as dopants. They were shown to have good crystal quality but had no selective contacts. Photoluminescence measurements were also done by the same group but the results showed no tuning of the effective bandgap [30].

2.2.2 Selective Ohmic Contacts

Conceptually, the making of selective contacts seems simple. However, it turned out that selective ohmic contacts with good ohmic and blocking properties, were difficult to achieve, particularly for samples with very high doping levels, where leakage due to tunneling current is high. The problem of achieving high quality ohmic contacts represents the greatest obstacle in the investigation of the physical phenomena of the doping superlattice.

The making of selective contacts on a GaAs doping superlattice, was first made possible by the alloying of small Sn and SnZn balls, which were diffused from the top layer through all the layers [47]. This method, however, suffers from high leakage current for samples with high doping levels. A major breakthrough in the selective contact technology was achieved by the introduction of the shadow mask technique [31]. The basic idea behind this technique is to use a Si mask with windows that are oriented such that the beam of the host material is normal to the substrate, whereas the dopant beams are incident under a certain angle of approximately 30° such that mesa-like

structures are grown. These angled beams of the dopants and the Si mask help to create a nipi structure in the centre and nini and pipi type structures towards the edges (see Figure 2.4). The metallic contacts to the nini and pipi regions can be done by standard methods. These nini and pipi regions (between 80 μm to 150 μm in width) at the edge of the mesa will serve to improve the quality of the selective contacts. Since the "intrinsic part" ($< 10^{15} \text{cm}^{-3}$) of the layer serves to reduce the leakage current in the contacts, the other major leakage currents are now contributed by the generation or recombination processes of the interlayer p-n junctions and between the bottom layer and the substrate.

During growth, the wafer was separated from the substrate with 0.01 mm tantalum shims to prevent fusion of the two pieces of Si during oxide removal. The mesas fabricated were 1.4 mm long and varied in width from 400 to 1000 μm . Layer thicknesses were determined by using a stylus profilometer to measure the mesa heights, assuming a constant deposition rate. Since they were not rotated during growth, there is a variation of dopant concentration and epilayer thickness across the wafers [27]. Immediately after growth, each wafer was covered with 500 nm of sputtered SiO_2 , and then windows were opened up at the edges for the contacts.

We have achieved good selective ohmic contacts for Si doping superlattices [26]. A 500Å layer of Pt was sputtered on and annealed at 500°C for 30 minutes to form PtSi contacts to the p-type layers along the pipi edge of the mesa. Since the PtSi has a high barrier height on n-type Si, it should provide a blocking contact to the substrate. To achieve this it was necessary to mask the mesas and etch

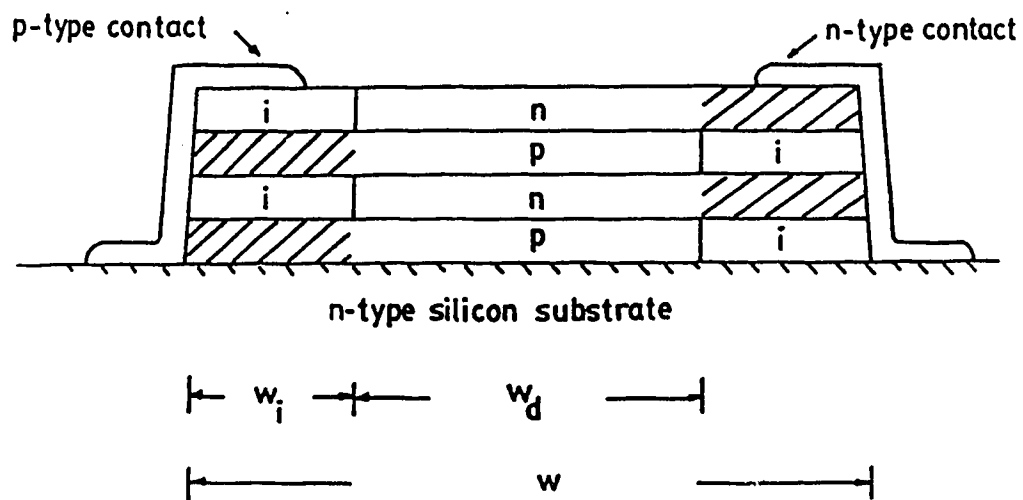


Fig. 2.4 Cross sectional view of a doping superlattice with selective contacts. Four layers are shown but usually 20 to 40 layers were grown. Apart from those between the p-n junctions, the shaded parts in the layers represent the undepleted regions of the layers.

back the surrounding substrate to remove adjacent doped regions which resulted from the previous dopant depositions.

For ohmic contacts at the n-type layers, we experimented with several different metals. The first was magnesium. A thermal evaporation technique was used to deposit about a 3000Å layer of magnesium on the nini edge of the mesa. A second layer of Al was added to prevent oxidation of the Mg and the whole contact was annealed at 300°C for 10 minutes. The problem with Mg₂Si contacts was that they were not physically even and, in some cases, were not ohmic. The second contact alloy used was AuSb (1% antimony) [23]. An 800Å layer was deposited and annealed at 400°C for 30 seconds. Using AuSb has the disadvantage that it can be easily peeled off Si and that the contacts are very sensitive to conditions such as timing and temperature of the annealing. The third contact alloy tried was Pt/Si/Er, in a three-layered structure [48]. Evaporation of Er, Si and Pt, of thicknesses of 300Å, 450Å and 750Å respectively, were done without breaking the vacuum, and annealed at 380°C for 10 minutes. This Pt/Si/Er contact has been shown to give good ohmic contact without the peeling problem.

As for those mesas with split contacts (see Figure 2.5), an area between the split contacts was etched away in a plasma etcher to remove the centre part of the nini and the p₁p₁ regions so that conduction between the contacts was through the fully doped part of the layers.

2.3 Electrical Properties

2.3.1 DC Characteristics

DC measurements of the quality of metal ohmic contacts and the

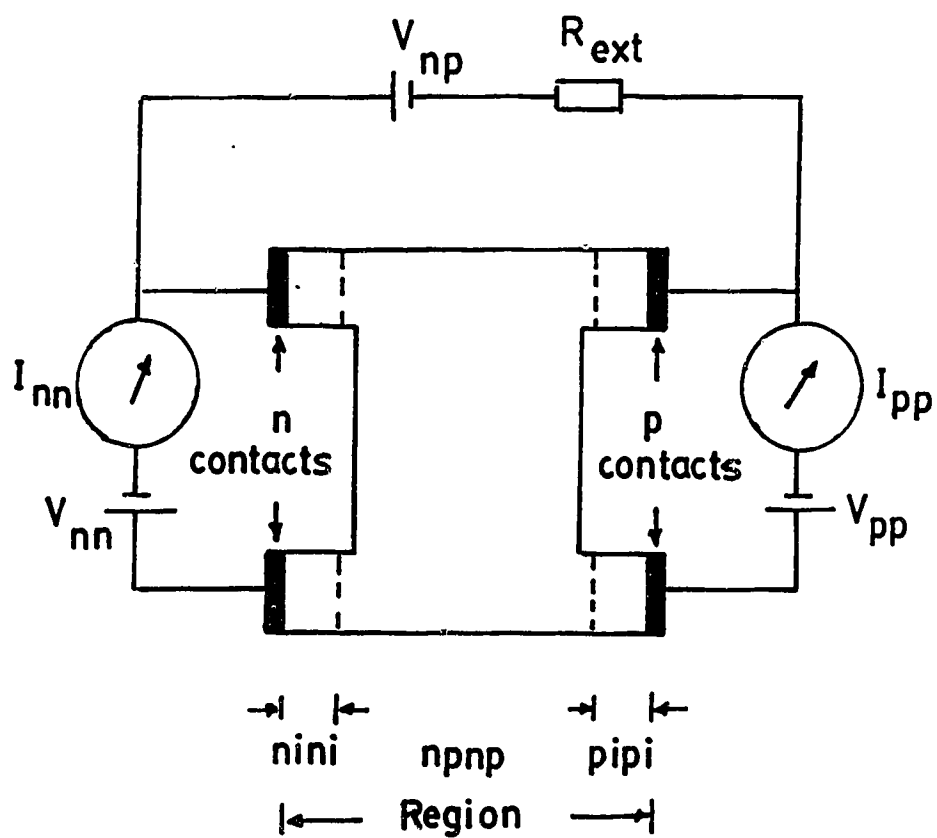


Fig. 2.5 Top view of a doping superlattice with split selective contacts.

I-V curve for the GaAs nipis were made [31]. The nipis exhibit diode-like characteristics which indicate that the selectivity of the contacts is good. For measuring the quality of the ohmic contacts, the contacts along nini and pipi edges were split at the centre so that the conductance of the n- and p-type layers could be measured separately, while adjusting the bias between the oppositely doped layers (see Figure 2.5). Our results for the measurement of DC resistance for Si nipis' show good linear I-V curves for both the n and p contacts [26].

Until now, no work has been reported on the analysis of AC characteristics of a doping superlattice. Chapter 4 will show an attempt to investigate the AC characteristics of doping superlattices using Si doping superlattices as case studies.

2.3.2 Tunable Conductivity

If the layer thickness is large ($> 1000\text{\AA}$), then the two dimensional electron and hole concentrations, $n^{(2)}$ and $p^{(2)}$, can be determined by the depletion approximation, where it can be shown that if $N_D \gg N_A$ then [49],

$$n^{(2)} = N_D d_n \left[1 - \left(\frac{V_{bi} - eU}{V_{bi} - eU^{th}} \right)^{1/2} \right] \quad (2.18)$$

where,

$$eU^{th} = V_{bi} - \frac{e^2}{8\epsilon} \frac{N_D}{N_A} (N_D + N_A) d_n^2 \quad (2.19)$$

and similarly if $N_A \gg N_D$ then,

$$p^{(2)} = N_A d_p \left[1 - \left(\frac{V_{bi} - eU}{V_{bi} - eU^{th}} \right)^{1/2} \right] \quad (2.20)$$

where,

$$eU^{th} = V_{bi} - \frac{e^2}{8\epsilon} \frac{N_A}{N_D} (N_A + N_D) d_p^2 \quad (2.21)$$

is the potential which, as usual the electron or hole concentration is reduced to zero and

$$V_{bi} = E_g - (E_c - \phi)_n - (\phi - E_v)_p \quad (2.22)$$

is the built-in potential which as per usual, is defined as the bulk energy gap E_g reduced by the quasi Fermi energy from the respective band edges in the n and p layers. eU is the external potential in eV.

Using $n^{(2)}$ as an example, and assuming $N_A = N_D$, the differentiation of (2.18) with respect to the external potential can be shown to be

$$\frac{dn^{(2)}}{dU} = \left[\frac{N_D \epsilon}{V_{bi} - eU} \right]^{1/2} \quad (2.23)$$

for $U < V_{bi}$. Equation (2.23) indicates that $dn^{(2)}/dU$ depends on the square root of N_D and this also holds true for the p layers.

The conductivity of the superlattice that is due to $n^{(2)}$ is

$$\sigma_e = e\mu_e n^{(2)}/d \quad (2.24)$$

where μ_e is the mobility of electrons and d is the period of the superlattice. Therefore, since $n^{(2)}$ depends on eU , the conductivity of the superlattice due to electrons can be tuned by an external bias.

The conductivity tunabilities of GaAs doping superlattices as a function of external bias and temperature in the range of 10°K to 300°K were experimentally determined [50]. The measured conductance in the n and p-doped layers are in agreement with the semi-classical theory outlined above. The carrier concentrations and mobilities as functions of external bias were also determined by Hall effect measurements. For the sample with $d_n = d_p = 70$ nm and $N_A = N_D = 7 \times 10^{17} \text{ cm}^{-3}$, the measured electron concentrations at $T = 77^\circ\text{K}$ for the voltage range of -0.5 to 0.5 V agreed well with the theoretical prediction. Below the voltage of -0.5V, the measured carrier concentration is higher than the theoretical prediction. This can be explained by an increased leakage current. The mobility data showed that the effective electron mobility decreases from the bulk value with the effective thickness of the layers. As the external voltage increases in reversed bias, the space charge region in the p-n junctions increases in thickness, effectively reducing the conducting thickness (effective thickness) of the p and n layers. This dependence of the effective carrier mobility on the effective thickness may be explained by the enhanced scattering in the space charge regions due to the reduced screening of the impurity potential in the space charge. On the other hand, for p-i-p-i or n-i-n-i structures, enhanced effective mobilities of carriers were also observed. This is again due to the reduced scattering of the intrinsic layers [6].

2.4 Optical Properties

2.4.1 Tunable Absorption Coefficients

In general, photon absorption at energies larger than the effective bandgap of the nipi is possible. Since this bandgap is tunable, it therefore follows that the absorption coefficient in a nipi is also tunable. Together with the possible long lifetimes of the carriers, this tunable absorption coefficient may also result in noticeable variation in the refractive index and strong optical nonlinearities [51].

The earlier analysis of tunable absorption coefficients in a nipi utilised the semiclassical theory. This treatment is valid for nipsis with very large periods where subband effects may be ignored. Absorptions beyond the fundamental edge, due to Franz-Keldysh effect were calculated for GaAs by Döhler et al. [52] and for Si doping superlattices by our group [24] and these results were compared with the experiments. There was good agreement between the theory and the experimental results for the tunability of the absorption coefficient in the GaAs nipi, but as yet we have observed no absorption shift in the Si nipi.

If the doping levels of the nipi are very high and the periods are short, subband effects on the absorption process can no longer be ignored. Calculations have shown that the absorption coefficients exhibit strong step-like characteristics as a function of energy [53].

In bulk semiconductors, a shift of the absorption edge is usually attributed to the band-filling effect, which in the case of a nipi can be controlled by tuning the quasi-Fermi energies of electrons and holes via external bias.

There have been reports on the design and feasibility of GaAs nipi photodetectors. Depending on the physical design, high photoconductivity gain, detectivity and large linearity range can be achieved when the nipi is reverse biased via a chosen value of serial external resistor R^{ext} . A gain-bandwidth product of 5 GHz has been reported for such a detector. A new design of the detector is presently being worked on to improve this gain-bandwidth product. The basic guidelines are that to improve gain, short transit times or short contact distances are required. Larger cross-sectional areas for absorption will improve detectivity but also increase capacitance [54].

Due to its ability to vary absorption coefficients via an external bias, a nipi can be used as a light modulator with electrical signal control. The only problem with the tuning of absorption coefficients via the selective ohmic contacts is the speed. Due to the relatively large capacitance of the p-n junctions of a nipi, the speed with which it can be modulated is limited by the RC time constant. To improve the speed, the nipi can be externally modulated by sandwich contacts as shown in Figure 2.6. The resistance of the sandwich contacts may be reduced to a small value if the multiple quantum wells are sandwiched by highly doped top and bottom layers. The capacitance is very much smaller compared to the selective contacts arrangement, due to the fact that the nipi structure behaves as a capacitance with a dielectric thickness given by the total thickness of the multiple quantum wells. The effective bandgaps, E_g^{eff+} and E_g^{eff-} , (see Figure 2.7) and hence the absorption coefficient are determined by the slope of the modulated potential, eFd [55], which in turn depends on the external bias [55].

A more complicated structure is the hetero-nipi, where a smaller

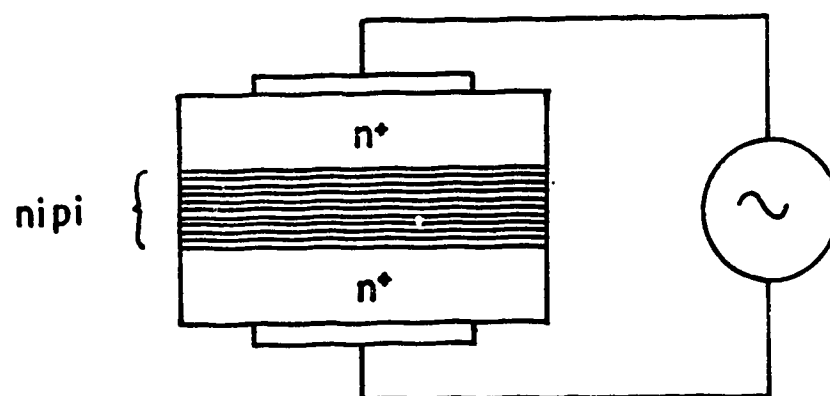


Fig. 2.6 A doping superlattice with sandwiched contacts [55].

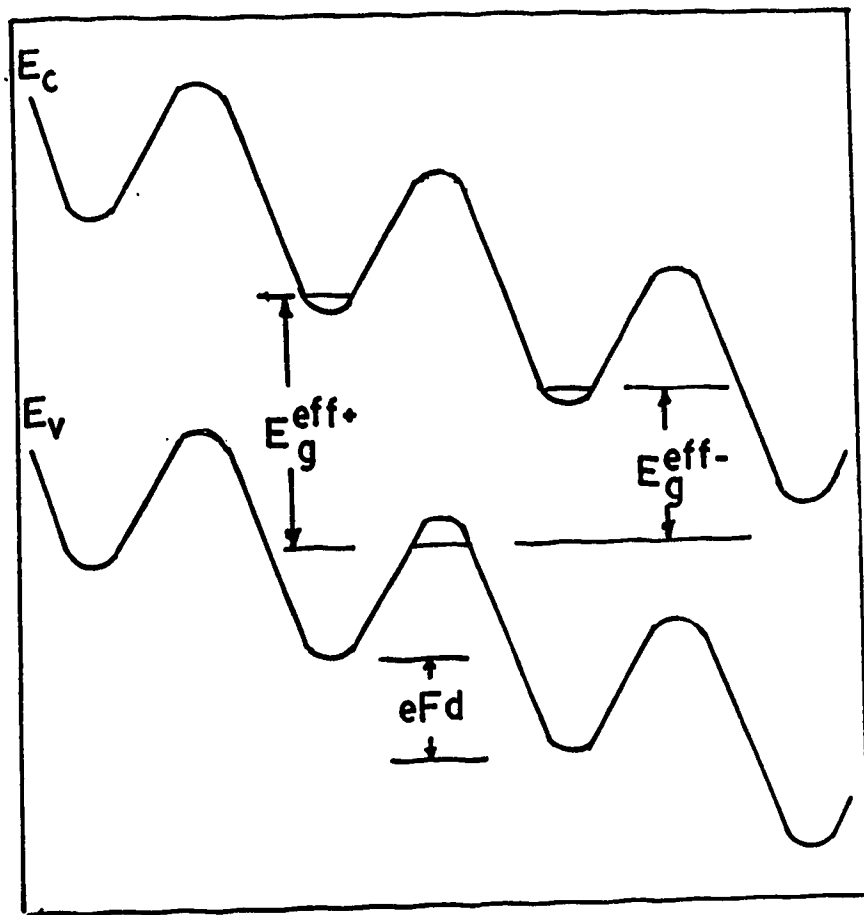


Fig. 2.7 A real-space band diagram of a doping superlattice under bias with sandwiched contacts [55].

bandgap material is sandwiched by a doped larger bandgap material. The energy band diagram is shown in Figure 2.8. Here the structure has the combined advantage of an undoped quantum well and the capability of tuning. Compared with the composite superlattice, the dark currents in the z-direction are small due to the larger barrier heights created by the doping regions [56].

One well-known application of the non-linear absorption properties of the multiple quantum well is the self electro-optic effect device (SEED) [57]. The basic structure of a SEED is similar to the one shown in Figure 2.6. It combines the properties of the quantum well modulators with photodetectors and some simple external circuit. Because of the non-linear absorption property of the quantum well, the photocurrent in the SEED can be in the high or low bistable states. The multiple quantum well may be either formed by the doping or the composite superlattice. So far, most of the experimental investigations on non-linear absorptions are carried out on composite superlattice [57,10]. Experimental work on non-linear absorptions in GaAs doping superlattices has recently been carried out by Ando et al. [51]. They have shown that a change of the absorption coefficient of greater than 4000/cm can be achieved with a weak excitation of 1 mW/cm^2 . The absorptive non-linearity is observed to be approximately one order of magnitude higher than the composite superlattice. This property will make nipi a potential candidate for applications in the SEED.

2.4.2 Tunable Luminescence

For optical emission to be tunable in wavelength, recombination

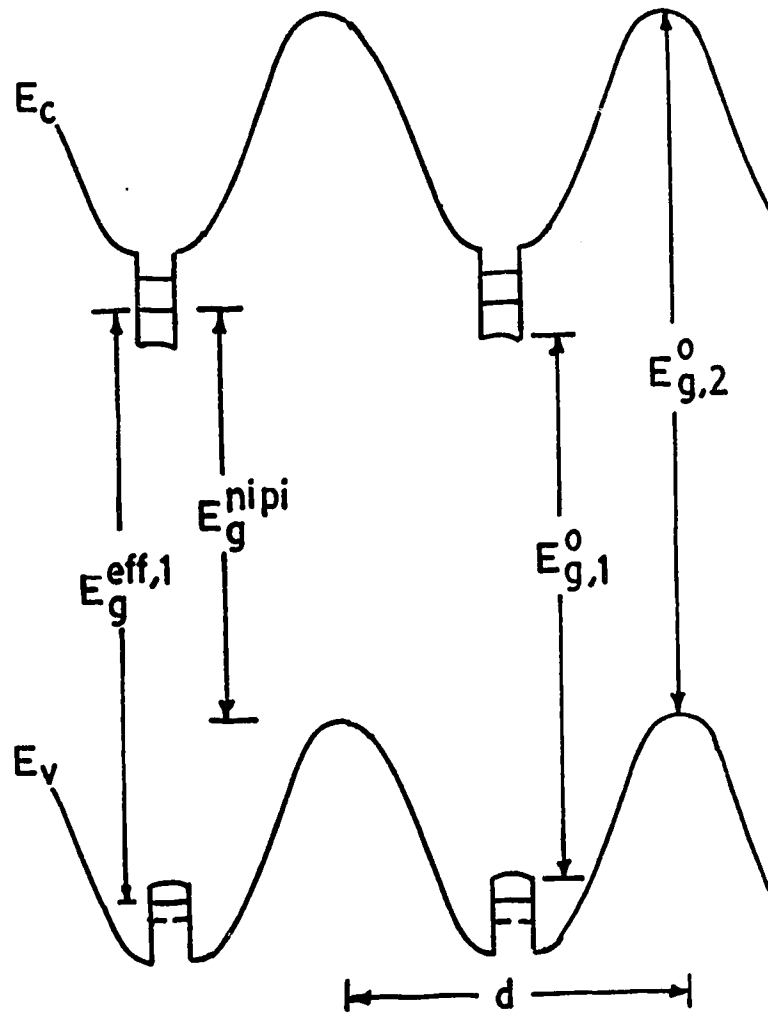


Fig. 2.8 A real-space band diagram of a hetero doping superlattice [34].

via the tunneling process must be dominant compared to thermally activated vertical recombinations. If thermal recombination strongly dominates, particularly at room temperature, then the wavelengths of the emitted photons will correspond to the bulk bandgap. For GaAs nipi, tunneling recombinations will dominate at room temperature provided the doping concentrations are higher than $3 \times 10^{18} \text{ cm}^{-3}$ [58,59].

Experiments have shown that the luminescence peak shifts as the excitation intensity is altered [59]. This shift, as a function of intensity agrees well with theoretical predictions both at room temperature and at low temperature. It also confirms that recombinations take place through the indirect bandgap in real space. The theory uses (2.15) to estimate the tunneling probability, where, at high and low temperatures, good agreement can be realised when light-hole mass and heavy-hole mass are used respectively in the calculations. At a higher temperature, the thermally-energized light holes dominate due to their larger overlap of wavefunctions with those of electrons.

The two-dimensional subband formation in GaAs doping superlattices was also verified by Raman measurements [60]. It was experimentally determined that the Raman peaks showed good agreement with the theoretical calculation of intersubband excitation.

The nipi can also be designed as an ultrafast modulator of photoluminescence using the circuit configuration as in Figure 2.6 [55]. Lasers based on GaAs nipi structures were also reported with emitted energy at 50 meV below the bulk bandgap [61,62]. They were operated at room temperature using pulse excitation and a minimum

threshold current density of 2.2 kA cm^{-2} .

Chapter 3

Recombination Mechanisms and Carrier Lifetimes

Carrier lifetime is one of the most important parameters that influences the primary and secondary properties of a doping superlattice [33]. The lifetimes of the carriers will affect the rate of change of the primary parameters such as the effective bandgap and carrier concentrations when the superlattice is under optical excitation.

The estimation of carrier lifetime in a doping superlattice has been discussed in Chapter 2. The recombination mechanisms are mainly attributed to tunneling and thermionic emission [33]. Temperature and the physical design of the doping superlattice will determine which mechanism dominates.

This chapter discusses the mechanisms of carrier recombination in a Si doping superlattice. It will be shown experimentally that recombination by tunneling and thermionic emission are not the dominant mechanisms. It is determined that carrier recombination via substrate shuntings and junction leakage due to defects are the dominant factors that limit the carrier lifetimes. A simple electrical model is used to estimate the carrier lifetimes for different temperatures and external bias. The theoretical estimates agree well with experiments. (A version of this chapter has been published. See Reference 28)

3.1 Calculation of the Carrier Lifetimes

In Section 2.1.2, it was mentioned that Döhler estimated the recombination lifetime in GaAs superlattices by thermionic emission of

carriers over the barriers between the n and p layers and by tunneling of the carriers through the barriers. These are the dominant recombination mechanisms in GaAs superlattices under no bias condition. With external bias through a very high impedance external circuit, the low generation-recombination currents in the depletion regions of the p-n junctions of the superlattice may be important in influencing the recombination processes in the superlattice. This is even more significant for a Si doping superlattice which has a smaller bulk bandgap compared to GaAs. Using the standard analysis of p-n junctions in the depletion approximation, the recombination current under forward bias is [63,64]

$$I_r \cong \frac{qA n_i W}{2\tau_o} \exp \left[\frac{eU}{2k_B T} \right] \quad (3.1)$$

where W is the depletion width, A is the cross sectional area of the p-n junction, and τ_o is the bulk recombination lifetime. If $r = dU/dI_r$ and c is given by the standard depletion capacitance, then it can be easily shown that the recombination lifetime attributed to the recombination current in the depletion region is given by

$$\tau = \frac{N_A \tau_o k_B T}{q n_i (V_{bi} - eU)} \exp \left[\frac{-eU}{2k_B T} \right] \quad (3.2)$$

If $N_A = N_D = 2 \times 10^{18} \text{ cm}^{-3}$, $\tau_o = 10^{-4} \text{ sec}$, $T = 300^\circ \text{K}$, $n_i \cong 10^{10} \text{ cm}^{-3}$ and $U = 0.5 \text{ V}$, then τ is about 38 ms. If one uses the thermionic emission expression of Döhler to calculate the lifetime, then τ_{th} is about $2 \times 10^6 \text{ s}$. Experimentally it was determined that the lifetime is about 1 ms at

a bias of 0.5 V. This result differs from the recombination current estimation by more than an order in magnitude and the thermionic emission by nine orders in magnitude.

Another possible mechanism of recombination, which may account for this difference, is the shunting of current through the defects in the p-n junctions (which will effectively reduce τ_0 of equation (3.2)), and/or in the substrate. A simple model to estimate the lifetime based on this assumption is presented in Figure 3.1.

At high doping ($>10^{18} \text{ cm}^{-3}$), each p-n interface in a Si doping superlattice with thick ($>800 \text{ \AA}$) layers will behave as an ordinary p-n junction. Hence for the capacitance per unit area of a superlattice with N periods, we may use the expression for the depletion capacitance of a linearly graded p-n junction [65]:

$$C/\text{area} = e \frac{dn^{(2)}}{dU} = (2N-1) \left[\frac{e a \epsilon^2}{12(V_{bi} - eU)} \right]^{1/3} \quad (3.3)$$

where $n^{(2)}$ is the total carrier concentration per unit area in the n-layers.

Figure 3.1 includes the equivalent circuit for a Si doping superlattice structure with an external bias U_{ext} connected through an external resistance R_{ext} . The capacitance between the n- and p-layers consists mainly of the junction capacitance $C_j(v)$ given above. $R_L(v)$ is the small signal resistance, dv/di_1 , seen by current flowing across the junction and may be determined from the I-V characteristics of the nipi. R_g is the contact resistance in series with the resistance between contacts parallel to the Si doping superlattice layers. R_{LS} is

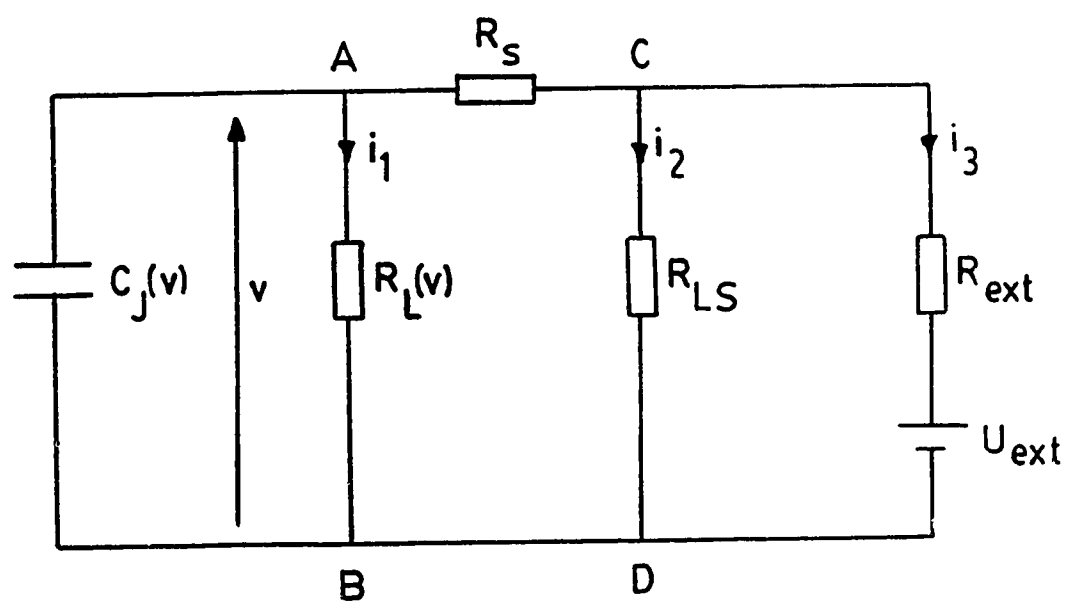


Fig. 3.1 Equivalent circuit of a Si n+p1 with external bias.

the resistance associated with the leakage current through defects and/or the substrate. Our method of measuring the recombination lifetime involves generating a small charge ΔQ with an optical pulse and observing the decay of the nipi voltage V back to the steady-state voltage V_{ss} ,

$$V - V_{ss} = \frac{\Delta Q}{C_J(v)} \exp(-t/R_{TOT} C_J(v)) \quad (3.4)$$

where

$$(R_{TOT})^{-1} = [R_L(v)]^{-1} + \{R_s + (R_{LS} R_{ext} / (R_{LS} + R_{ext}))\}^{-1} \quad (3.5)$$

An alternative method is to monitor the resistance of the n or p layers through split contacts. In either case, if the current from the generated charge is small enough, the potential across each junction will not deviate far from its steady-state value and the junction resistance may be found from $1/R(v) = di_1/dv$ evaluated at $V = V_{ss}$. In practice, $R(v)$ cannot be measured directly; but provided R_s is small and R_{LS} is large, $R_L(v)$ may be estimated from the I-V measurements carried out at points CD in Figure 3.1. With external biasing, R_{ext} should be normally large.

3.2 Experimental Results

The nipi (sample 405A) was designed to have 10 n layers and 10 p layers separated by thin intrinsic layers. However, the intrinsic layers were washed out during the boron doping. As will be shown in the next chapter, for the range of bias that is being used in the experiment, the doping profile of the sample is approximately linearly

graded. Accounting for the variation of deposition rates and dopant concentration over the wafer, as deduced from SIMS measurements in control wafers, it is estimated that sample 405A has a doping gradient between $8 \times 10^{23} \text{ cm}^{-4}$ and $4 \times 10^{24} \text{ cm}^{-4}$, such that the corresponding V_{bi} may be between 0.88V and 0.91V. The maximum doping levels of both the n and p layers range from $2 \times 10^{18} \text{ cm}^{-3}$ to $8 \times 10^{18} \text{ cm}^{-3}$ and the thickness per layer is about 120nm, sufficient enough to prevent full depletion in the layers for the bias that is considered in the experiment.

3.2.1 Capacitance Measurement

The measurements of $dn^{(2)}/dU$ were carried out at 80°K using the arrangement shown in Figure 3.2. At this temperature, the recombination lifetime of the carriers is sufficiently long and shunting current sufficiently negligible to allow injected charge into the nipi to be measured with accuracy. The net injected charge can be obtained by observing the difference in voltage that developed across the 1 M Ω resistor. The voltage developed across the nipi is then measured by the oscilloscope with a 10 M Ω input. Hence, the change of $n^{(2)}$ with respect to the change in the potential can be determined. Using a 0.5 ms pulse that is produced from a pulse generator, and the nipi at 0 V bias, $\Delta Q/\Delta U$ is measured to be approximately $4.6 \times 10^{-8} \text{ C/volt}$ or 46 nF. If the effective area of the nipi is assumed to be 1 mm² then $dn^{(2)}/dU$ is approximately $2.88 \times 10^{17} / \text{m}^2 / \text{volt}$. Measurements at other values of bias become less accurate due to higher leakage. However, the capacitance at other values of biases may be determined theoretically by the proportionality of $(V_{bi} - U)^{-1/3}$ where V_{bi} is assumed 0.9V. Due to the cube root function, the accuracy of the value

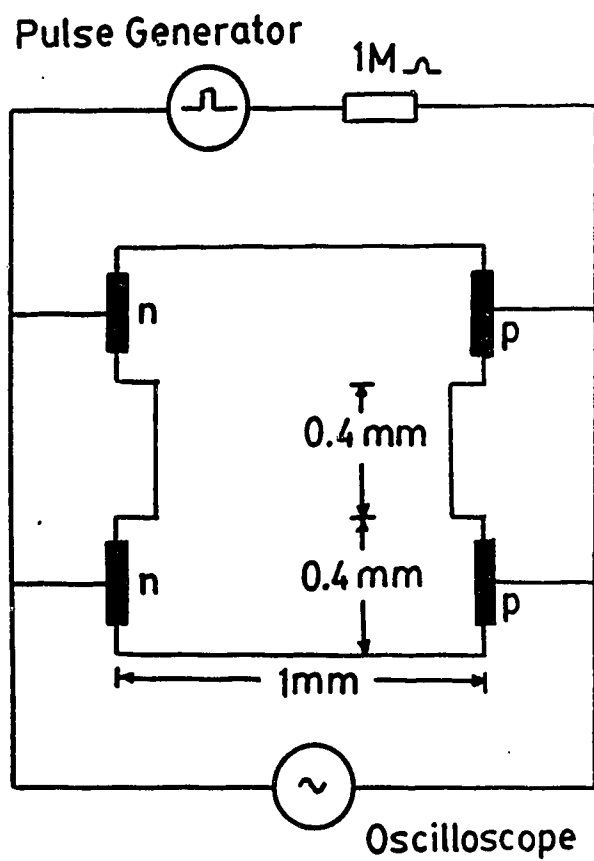


Fig. 3.2 Circuit to measure $dn^{(2)}/dU$.

of V_{bi} is not very critical.

3.2.2 Carrier Lifetimes Measurement by Photoconductivity Method

The carrier lifetimes were measured with the photoconductivity method shown in Figure 3.3. The measuring system is modified from a system which was originally used for photo-induced transient spectroscopy (PITS) [66]. As the photoconductive signal from the sample was less than one mV, a multiple stage DC amplifier with gain was used to amplify the signal to a level which is acceptable to the 12 bit A/D converter (DAS 1128). The A/D converter can accept voltages in the range of ± 5 V. The amplified photoconductive signal is digitised by the A/D converter and stored in the computer for further processing.

The vacuum system used for low temperature measurements utilised mercury diffusion pumps in addition to a mechanical pump. The temperature of the system was controlled by the combination of a local heater and the manual control of the rate of flow of liquid nitrogen. For the measurement of carrier lifetimes as a function of temperature, the rate of temperature increase was less than or equal to $1^\circ/\text{min}$.

The carrier lifetimes were measured as a function both of external bias and temperature using the arrangement shown in Figure 3.3. The former were measured at 80°K . The carrier density was inferred from the conductance across the p layers after the mesa was illuminated with $0.5 \mu\text{W}$, 10 msec pulses from a HeNe laser operating at 633 nm. The voltage across the p-type layers and n-type layers was kept to a small fraction of a volt in order to avoid serious voltage differential developing across the nipi structure. The rise and fall times of the pulses of 0.1 msec were produced by chopping. The DC bias across the

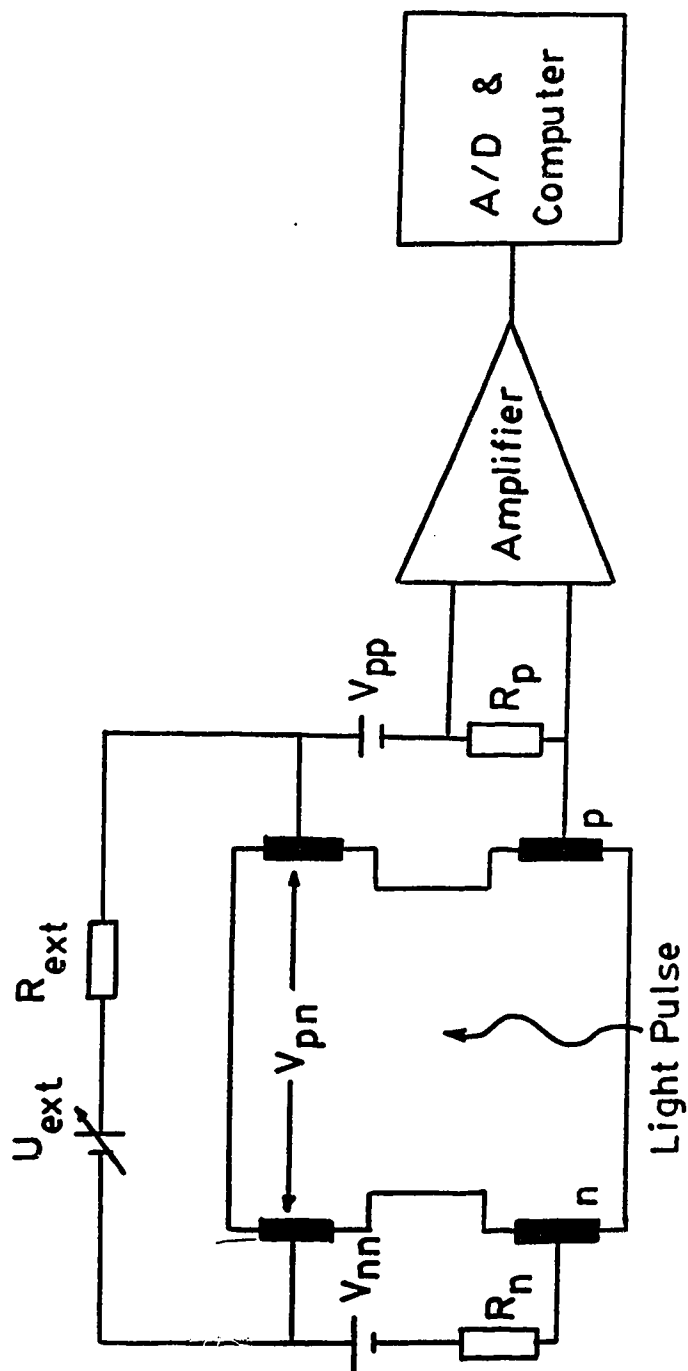


Fig. 3.3 Schematic of carrier lifetime measurements. $V_{pp} = 0.12V$ to give a potential across the p- and the n-split contacts of $0.1V$. $R_{ext} = 10 \text{ Mohms}$.

nipi was provided by varying the voltage U_{ext} . The small signal resistance across the nipi structure was also estimated from the I-V characteristics for various values of DC bias and the capacitance of the nipi was determined from the above. Finally the lifetime $R_{TOT}C_J(v)$ was computed. The results are shown in Figure 3.4.

Next, the lifetime as a function of temperature, was measured with U_{ext} and V_{nn} disconnected and the two n contacts shorted. Since the resistance of the p layers changed with temperature, R_p was varied to achieve efficient power transfer. The lifetime was first measured using the HeNe laser at 633 nm and then repeated with 560 nm light from a LED, but with longer 40ms pulses to compensate for the lower light intensity. The results are shown in Figure 3.5. The small signal resistance across the nipi as a function of temperature was also estimated from current measurements carried out at bias of -15 mV and 15mV. Since the capacitance of the nipi does not change greatly with temperature, the value of 46 nF was used throughout to calculate the values of $R_{TOT}C_J(v)$ for various temperatures.

To determine whether traps have any influence on the carrier lifetime, more measurements were made with all n layers and p layers shorted out. This was achieved by separately shorting the upper and lower opposite n and p contacts pairs of the mesa. Any free carriers generated by the illumination will recombine through the external short circuit path, leaving the traps to dictate the characteristics of the conductance. The lifetime observed was about 2 msec at 80°K and 0.5ms at room temperature indicating that traps could not strongly influence the measured lifetimes.

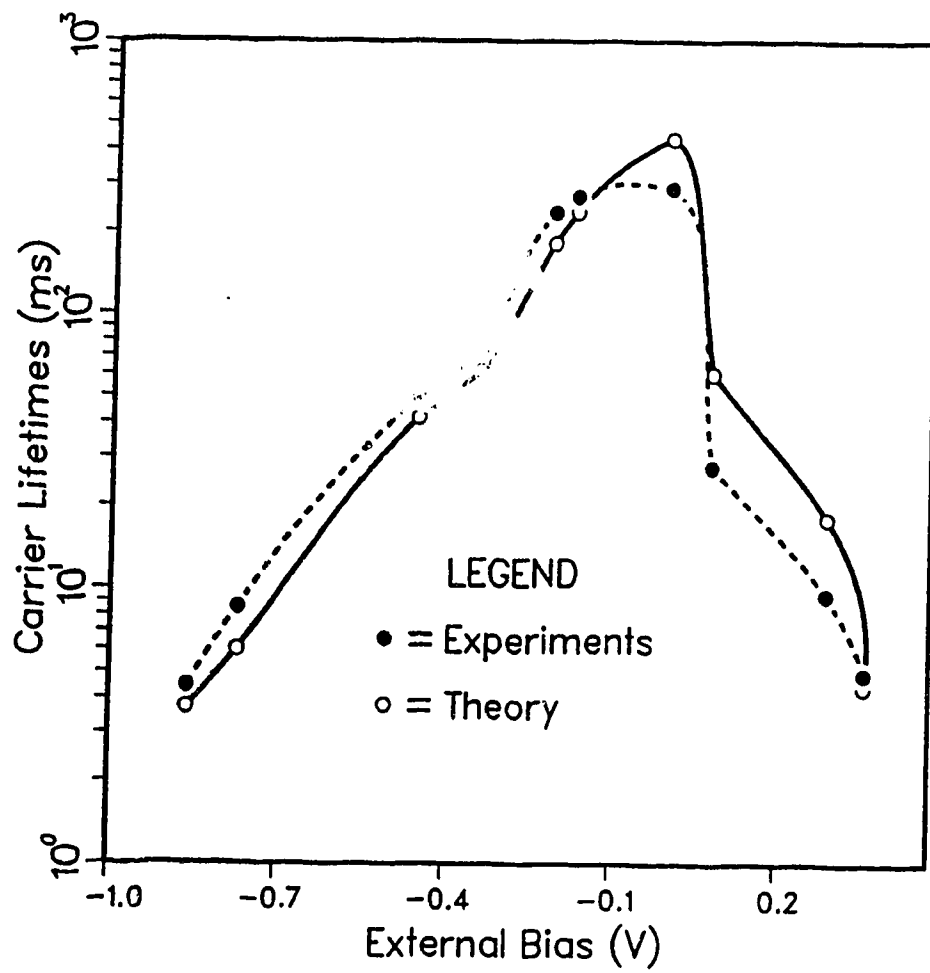


Fig. 3.4 Carrier lifetime as a function of external bias at $T=80^{\circ}\text{K}$.

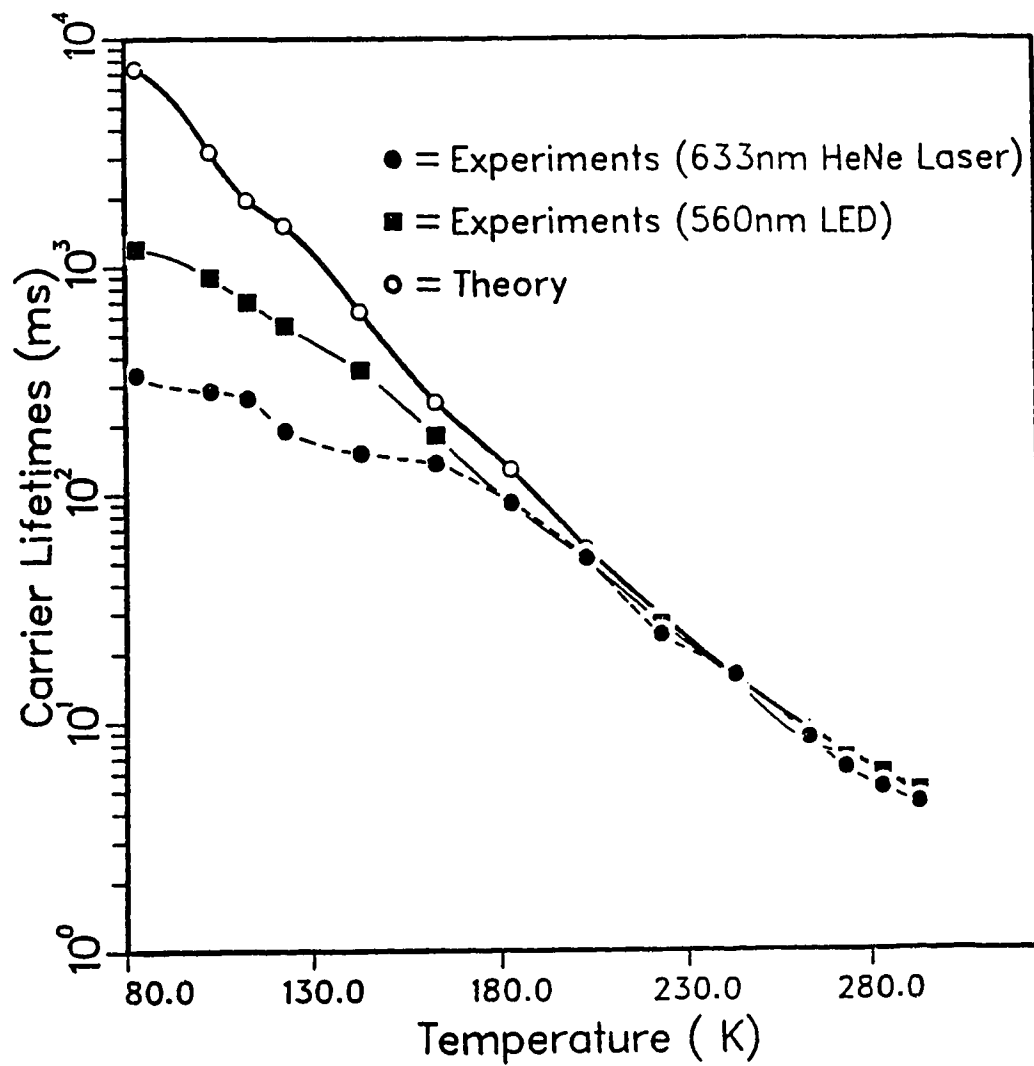


Fig. 3.5 Carrier lifetime as a function of temperature.

3.3 Discussion

In general the model presented here is consistent with the experimental results showing that thermionic emission and tunneling are not the dominant recombination mechanisms. The carrier lifetime in the Si nipi, with wide layers can be estimated from the product of its capacitance and its effective small signal resistance. The disparity at low temperatures may be due to the reduction of the temperature dependent substrate resistance when exposed to optical excitation. The HeNe laser has a $1/e$ absorption depth at $T = 80^\circ\text{K}$ of approximately $5\text{ }\mu\text{m}$, while the corresponding absorption depth of the LED is $2\text{ }\mu\text{m}$ [67]. Hence, the reduction of substrate resistance during optical excitation will be less for the LED, which may account for the four-fold increase in the carrier lifetime of the nipi. Another possible source of error is that the effective small signal resistances of the nipi were obtained from points CD rather than points AB of the equivalent circuit in Figure 3.1 and it may not be possible to neglect the contact resistance in all cases. Traps do not seem to influence significantly the recombination lifetime of the free carriers in the nipi. For narrow barrier Si doping superlattices where tunneling is important the calculation of Döhler [33] for the direct bandgap materials would have to be modified to take into account the fact that the transitions are indirect both in real space and momentum space.

Chapter 4

Steady State Small Signal AC Analysis

In Chapter 3, it was determined that traps in the Si doping superlattice do not seem to affect significantly the recombination lifetime of the free carriers. This may be due to the relatively low density of deep level traps. To determine the energy level and the density of deep level traps, one of the most common and reliable methods is deep level transient spectroscopy (DLTS) [68].

The DLTS method basically uses the principle of a capacitance transient. The measurement of the capacitance of the Si doping superlattice at 1 MHz operating frequency indicated that the value was two orders of magnitude smaller than expected. This prompted the investigation of this problem, which resulted in the development of a circuit model for the doping superlattices.

Electrical characterisation by the use of simple circuit analysis is a useful tool for understanding the complex physical mechanisms inside semiconductor structures and devices [69-71,31]. Doping superlattices with selective contacts fabricated by the shadow mask MBE technique are known to have complicated internal structures [72]. In a previous paper [26], the DC characteristics of a doping superlattice were described. However such an analysis is unable to provide frequency dependent parameters such as the junction capacitance and the AC conductance of the superlattice. These parameters are required for the proper interpretation of other measurements such as DLTS. In this chapter, a small signal AC circuit lumped model is introduced to analyse a Si doping superlattice under reverse DC bias. Equivalent

circuits are written in terms of linear parameters such as AC resistance and capacitance. Experiments using a small signal AC bridge were carried out on two Si doping superlattice samples under a range of reverse bias and the measurements were compared with the theoretical results given by the model. In this way, parameters such as capacitance, AC conductance and doping profile of the doping superlattices were inferred. (A version of this chapter has been accepted for publications. See Reference 32.)

4.1 Linear Electrical Lumped Circuit Model

The structure of a doping superlattice with selective contacts is shown schematically in Figure 2.4. If the layers are highly doped and of sufficient thickness to prevent full depletion of the layers from occurring under limited reverse bias, then the superlattice can be assumed to be made up of multiple p-n junctions in parallel. Normally a p-n junction under reverse bias is assumed to have the equivalent circuit shown in Figure 4.1, where R_{SI} is the total serial resistance, R_L , as in Chapter 3, is made up of the junction leakage resistance and the voltage dependent junction resistance, and C_j is the voltage dependent depletion capacitance. However, the Si doping superlattices under consideration have wide ($300 \mu\text{m} < W < 1000 \mu\text{m}$), thin ($\geq 0.1 \mu\text{m}$) layers in which the resistance along the layers is non-negligible. Under these circumstances, a more realistic model is that shown in Figure 4.2, where again the values of the discrete circuit elements depend on the applied bias. The number of lumps, N , can be increased as the width of the layers increases. Furthermore, because the serial AC resistances, r_p and r_n , along the layers are very small compared to

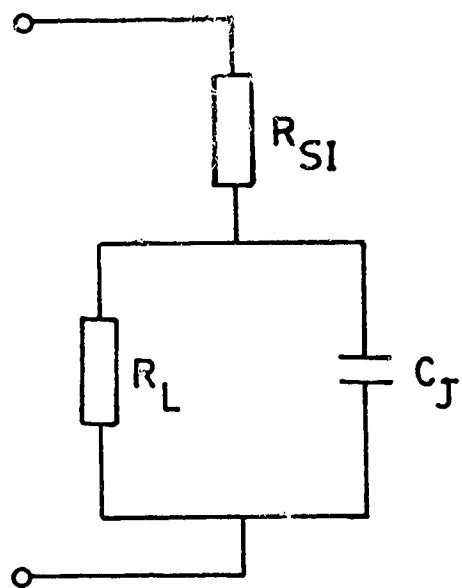


Fig. 4.1 Electrical model for a diode under reverse bias.

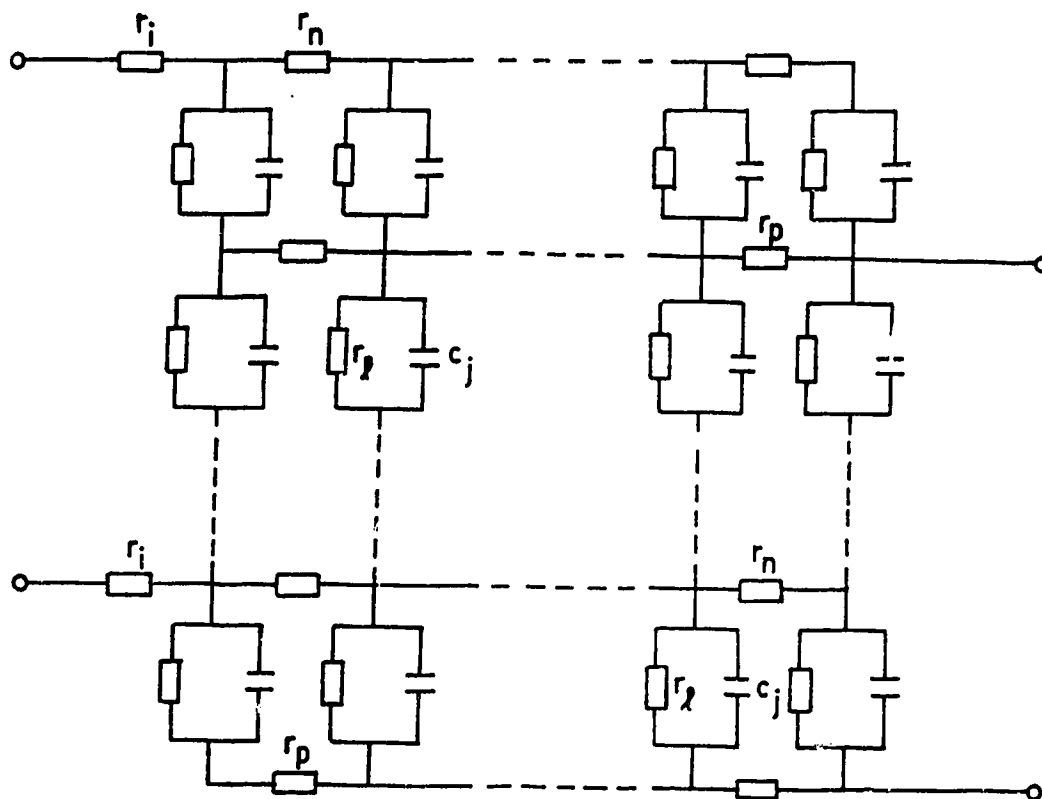


Fig. 4.2 Lumped electrical model for a doping superlattice.
 $r_l = r_p r_n / (r_p + r_n)$.

r_{ℓ} , the DC voltage across each $r_{\ell}c_j$ element will be approximately constant. With the exception of the top and the bottom layers, it can be assumed that the p-n junctions between all layers will have similar characteristics. If the number of layers is large, in our case 20, then one can in practice ignore the slight differences in characteristics introduced by the top and the bottom layers and sum up the parallel effect of all the p-n junctions. The resulting equivalent circuit is shown in Figure 4.3. Now we have included R_c , the contact resistance of the metal-semiconductor interface and R_{cs} , the resistance of the non-depletion portion of the n- and p-type layers (indicated by shaded regions in Figure 2.4). For very high doping levels ($>3 \times 10^{18} \text{ cm}^{-3}$), R_c is never more than a few ohms [48].

There are also other p-n junctions formed such as the one between the bottom layer and the substrate, and those of the "intrinsic" and the doped layers formed for the selectivity of the contacts (see Figure 2.4). It is to be noted that the "intrinsic" regions are in general lightly doped due to non-abrupt doping profiles. The stray capacitances introduced by these junctions are generally negligible compared to the capacitance of the p-n junctions in the superlattice because of their larger depletion regions. In addition, the leakage of the substrate can be ignored since the PtSi p-type contact serves as a good rectifying barrier to the n-type substrate [26].

In order to determine the values of the discrete circuit elements of our model, we may compare the measured impedances of the superlattice at different frequencies with those predicted by standard linear circuit analysis of Figure 4.3 (these being valid as long as the AC signal is small enough that the voltage dependent elements are

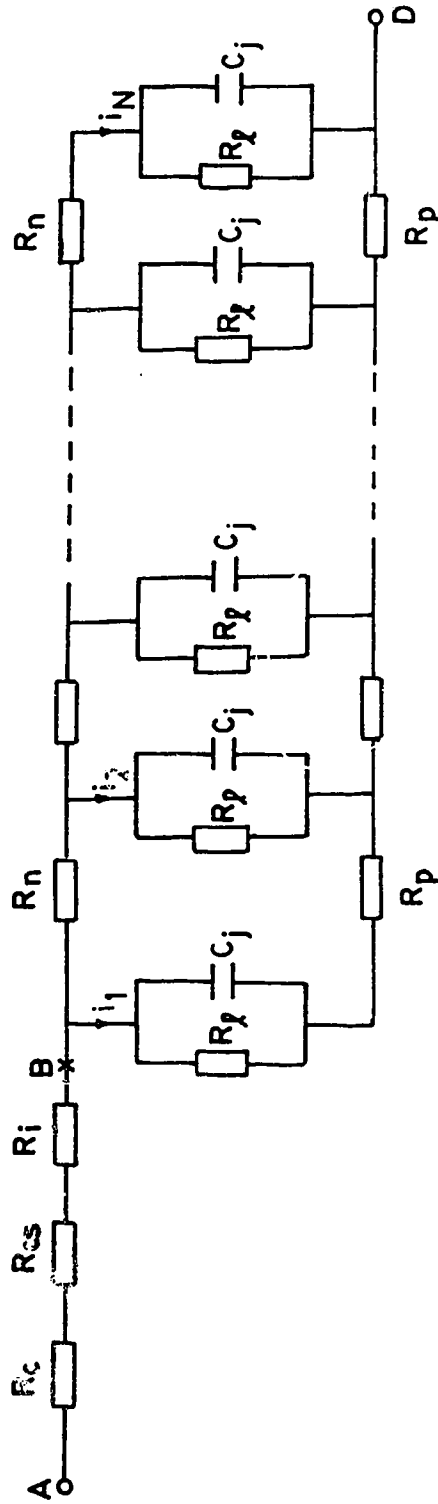


Fig. 4.3 Net equivalent circuit of a doping superlattice.
 $R_1 = R_p R_n / (R_p + R_n)$.

constant). For the measurements, a bridge was used which gives the impedance in terms of a capacitance and a AC resistance either in parallel or in series. Measurements at high and low frequencies were used to find a first approximation to the unknown circuit elements. For example, at high frequency the measured impedance across the superlattice will be approximately given by

$$R_s = R_c + R_{cs} + N R_n / 2 \quad (4.1)$$

if we assume that $R_n = R_p$. If $R_n \neq R_p$, then $R_n / 2$ is replaced by $R_{pn} = R_p R_n / (R_p + R_n)$. Similarly, in the frequency range

$$1/R_c C_j < \omega < 1/[(N-1)R_n C_j] \quad (4.2)$$

a series impedance measurement gives an approximate value for NC_j . Likewise, R_c/N and NC_j can be approximately obtained from the low frequency parallel impedance measurements. The final values of these parameters were fine tuned by curve fitting to the experimental results. The curve fitting was carried out by trial and error and visual inspection. As mentioned earlier, the number of required lumps, N , will depend on the width W_d (see Figure 2.4) of the superlattice. It is expected that the calculated impedance will approach a limit as the value of N increases.

4.2 AC Characteristics under Reversed Bias

In order to obtain some general properties of the circuit of Figure 4.3, some typical values for the circuit elements were used (see

Table 4.1) and the equivalent serial and parallel impedance (capacitance and AC resistance) as a function of frequency were calculated using $N = 24$. Seven cases with different values of the circuit elements were considered in the calculations and the results are shown in Figures 4.4 and 4.5. The capacitances are normalized to NC_j and the serial and parallel AC resistances are normalized to R_s (see (4.1)) and R_p/N , respectively.

4.2.1 Capacitance

Consider first the parallel capacitance characteristics of Figure 4.4. At low frequency, the capacitance characteristics for all cases approximate NC_j . At high frequency, the frequency at which the normalised values of the parallel capacitance are reduced to 0.5 (the 3 dB frequency) may be approximated by

$$f_{cp} = [2\pi R_s NC_j]^{-1} \quad (4.3)$$

where R_s is given by (4.1) for $R_n = R_p$. This is demonstrated by the common high frequency characteristics of cases B, F and G (as these cases have the same $R_s C_j$). For case A, where $R_n \neq R_p$, R_n of (4.1) may be replaced by R_p if $R_p > R_n$. As the circuit of Figure 4.3 is not a single-pole circuit, the 3 dB frequency of (4.3), which can be derived from a single-lump model of Figure 4.1 (see Appendix A), is at best an approximation.

As for the serial capacitance characteristics shown in Figure 4.4 by the dotted curves, the frequencies where the normalised values begin to deviate from unity for the lower and upper limits may be

Table 4.1. The values of the discrete circuit elements for cases A to G.

Case	R_n (ohms)	R_p (ohms)	R_ℓ ($\times 10^6$ ohms)	$R_c + R_{cs}$ (ohms)	C_j ($\times 10^{-9}$ F)
A	25	2.7778	1	30	0.5
B	5	5	1	30	0.5
C	1	1	1	30	0.5
D	25	25	1	30	0.5
E	5	5	1	30	0.1
F	5	5	0.1	30	0.5
G	5	5	10	30	0.5

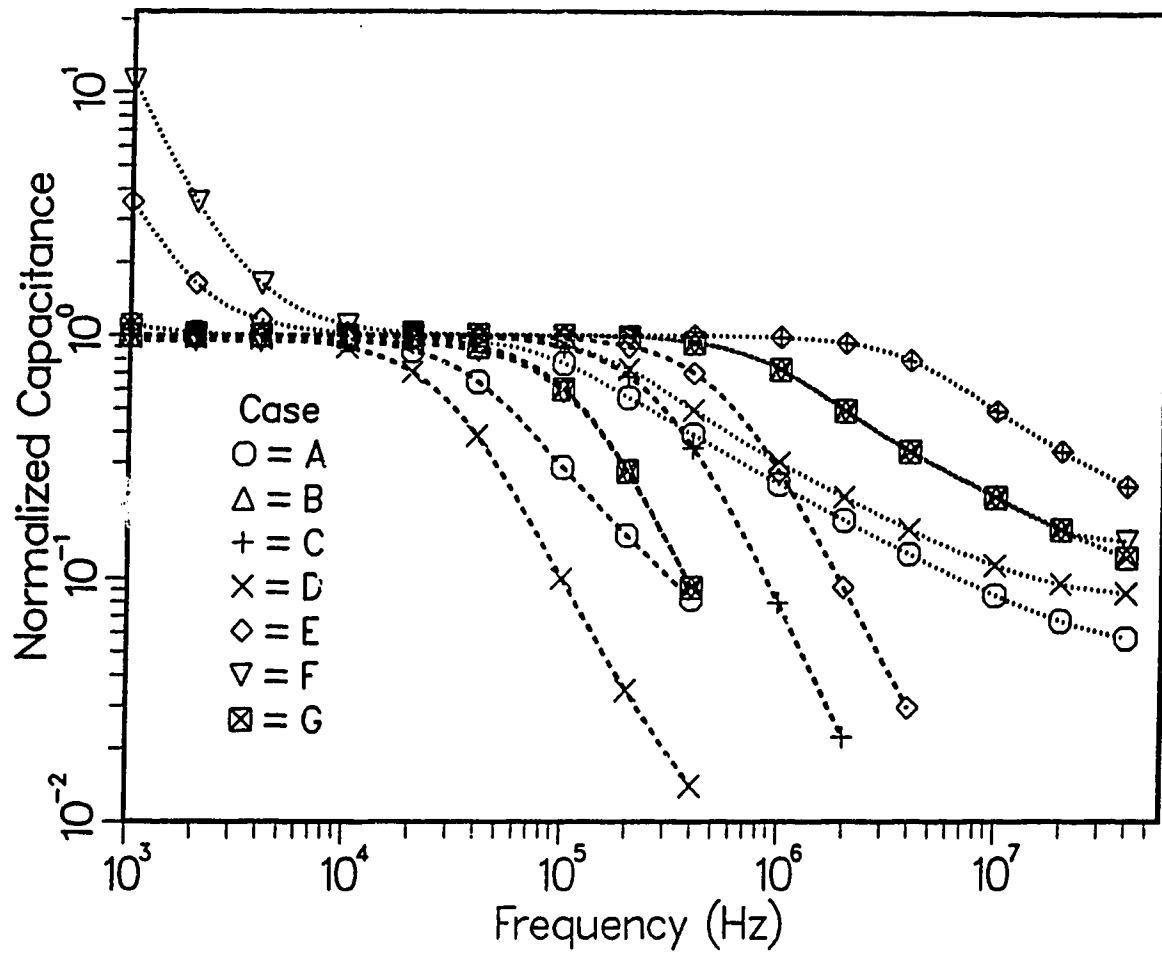


Fig. 4.4 Calculated capacitance characteristics of a doping superlattice for $N = 24$. The dotted and dash curves represent the serial and parallel capacitances, respectively. The values of the discrete circuit elements of Figure 4.3 for cases A to G are shown in Table 4.1.

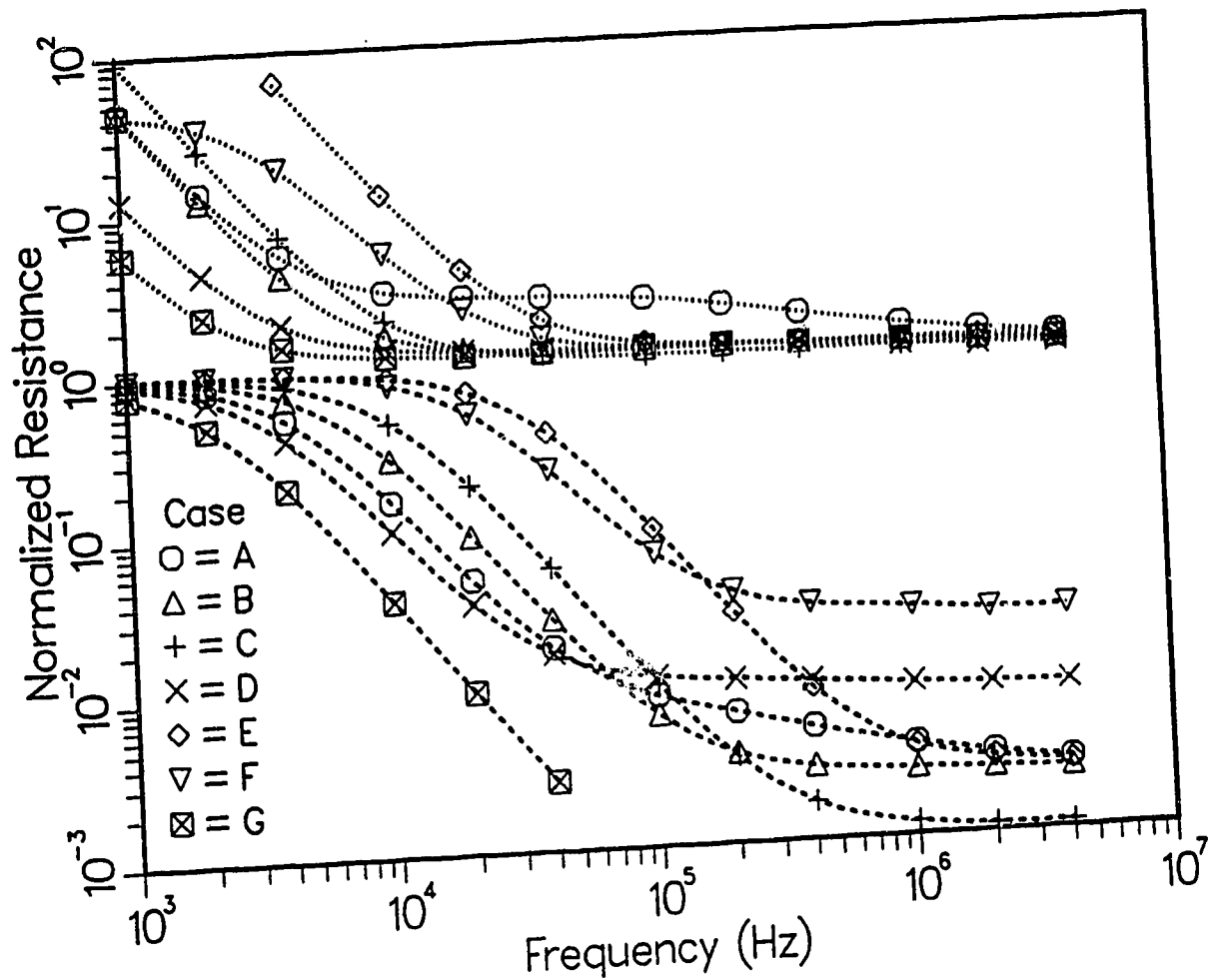


Fig. 4.5 Calculated AC resistance characteristics of a doping superlattice for $N = 24$. The dotted and dash curves represent the serial and parallel AC resistances, respectively. The values of the discrete circuit elements of Figure 4.3 for cases A to G are shown in Table 4.1.

approximated by expression (4.2). Just as in the parallel capacitance arrangement, cases B, F and G share similar characteristics at high frequency, due to the fact that they have the same product $R_n C_j$. Cases C and E, though having different values of R_n and C_j , have the same value of $R_n C_j$, hence they share similar high frequency characteristics. Again, if $R_p > R_n$, then R_n of expression (2) may be replaced by R_p . At low frequency, the deviation of the normalized serial capacitance is dependent on the product $R_\ell C_j$ (see Appendix) and they are explicitly illustrated in Figure 4.4 for cases E and F. It is to be noted that, unlike the parallel capacitance characteristics, the serial capacitance characteristics are independent of the value of $R_c + R_{cs} + R_i$.

4.2.2 AC Resistance

As far as the AC resistance characteristics are concerned, the high and low frequency measurements give the net serial AC conductance (see (4.1)) and the parallel AC resistance, R_ℓ/N , respectively, of the doping superlattice. Similar to the capacitance characteristics, the 3 dB frequency of the serial and parallel AC resistance characteristics may be approximated by $(2\pi R_\ell C_j)^{-1}$ and $[(R_s R_\ell/N)^{1/2} (2\pi N C_j)]^{-1}$, respectively, if $R_\ell \gg R_s$. These approximations can be easily obtained from the single lump model of Figure 4.1 (see Appendix). For example, in cases F and G a factor of 100 change in the value of R_ℓ gives a factor of 10 change in the 3 dB frequencies of the parallel AC resistance characteristics. Similar properties are observed for the serial AC resistance characteristics. For case A, where $R_n = 9R_p$ and R_{pn} has the same value as case B, observe that the serial and parallel characteristics are different from all other cases where $R_n = R_p$.

These differences in characteristics will help to identify a doping superlattice layer resistance if the value of R_n is very different from R_p .

As mentioned earlier, the serial resistance of the doping superlattice can be determined from the AC resistance characteristics at high frequencies. However, this value also includes R_c , R_{cs} and R_i [see (4.1)]. To determine R_{pn} , the serial capacitance characteristics may be used since it is independent of R_c , R_{cs} and R_i . In general, although the 3 dB frequency for the parallel capacitance and the central frequency range for the serial capacitance are only approximate values, they nevertheless provide useful information when one also wishes to determine the value of the capacitance, NC_j . The knowledge of this frequency range is also vital for DLTS measurements on a doping superlattice [73].

4.3 Experimental Results and Discussions

For the experimental results, we measured two samples of different width W with an HP 4275A bridge. Samples 405B and 405C have widths of about $350\mu\text{m}$ and $550\mu\text{m}$ respectively and lengths of about 1.4mm . The doping sources were set to give a doping level of $4 \times 10^{18} \text{cm}^{-3}$ (n- and p-type layers) for a rotating wafer during growth. Since a shadow mask technique was used [26], the wafer was not rotated during growth. As a result, both the thicknesses of the layers and the doping levels for the n and p-type layers will vary at different points of the wafer. As these two samples were taken from different parts of the wafer, their doping levels and layer thicknesses will be different [23]. The samples consisted of 20 p and n-doped layers, that is 10 periods. The

thickness of each layer for sample 405B was about 700Å to 900Å while for sample 405C it was about 1000Å to 1200Å. The doping levels for both the n and p-doped layers are difficult to determine but from past experiments on grown wafers using resistivity measurements, they can be estimated to be in the range from 1×10^{18} to $8 \times 10^{18} \text{ cm}^{-3}$. Although the doping sources were set during crystal growth to give the same doping level for the n and p-type layers, because of the non-rotated wafer, their doping levels could still differ by as much as a factor of 5. From resistance mapping of single n and p-type layers grown on wafers, it was estimated that the variation of the doping levels (n and p-type layers) across samples 405B and 405C were 14% and 17% respectively. Since the calculated results in Figures 4.4 and 4.5 indicate that the capacitance and AC resistance characteristics are not very sensitive to the difference between R_n and R_p , and in order to reduce the number of unknowns, we have assumed $R_n = R_p$. This assumption is proven to be a fair approximation, as will be shown below, by the good fit between theory and experiment. The range of frequency used in the impedance measurement is 10^4 to 10^6 Hz, while the reverse bias to the samples varies from 0 to 2V.

Figure 4.6 and Figures 4.7 to 4.10 show the measured and calculated results of AC resistance and capacitance for samples 405B and 405C respectively, using parallel and serial bridge equivalent circuits. As discussed earlier, at low frequency the measured parallel capacitance in Figure 4.6 approximates the net depletion capacitance of the layers of the superlattice. Similarly, at high frequency, the measured serial AC resistance shown in Figure 4.6 reflects the net conductance of the layers of the superlattice. R_{cs} is relatively large

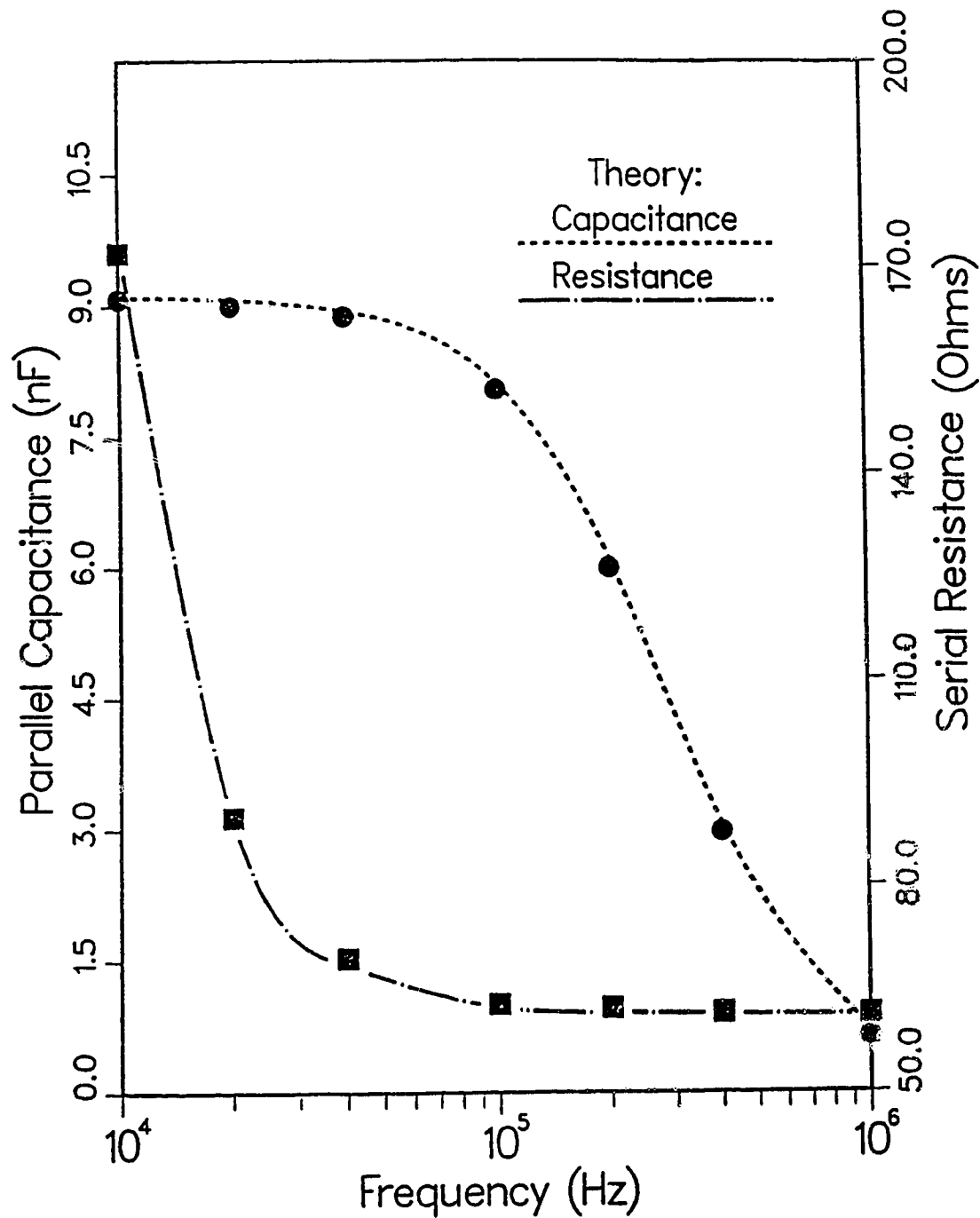


Fig. 4.6 Equivalent parallel capacitance and AC serial resistance as a function of frequency for sample 405B. The experimental data are represented by the symbols and the theoretical calculations were carried out with $N = 12$. The doping superlattice is under a reverse bias of 2V.

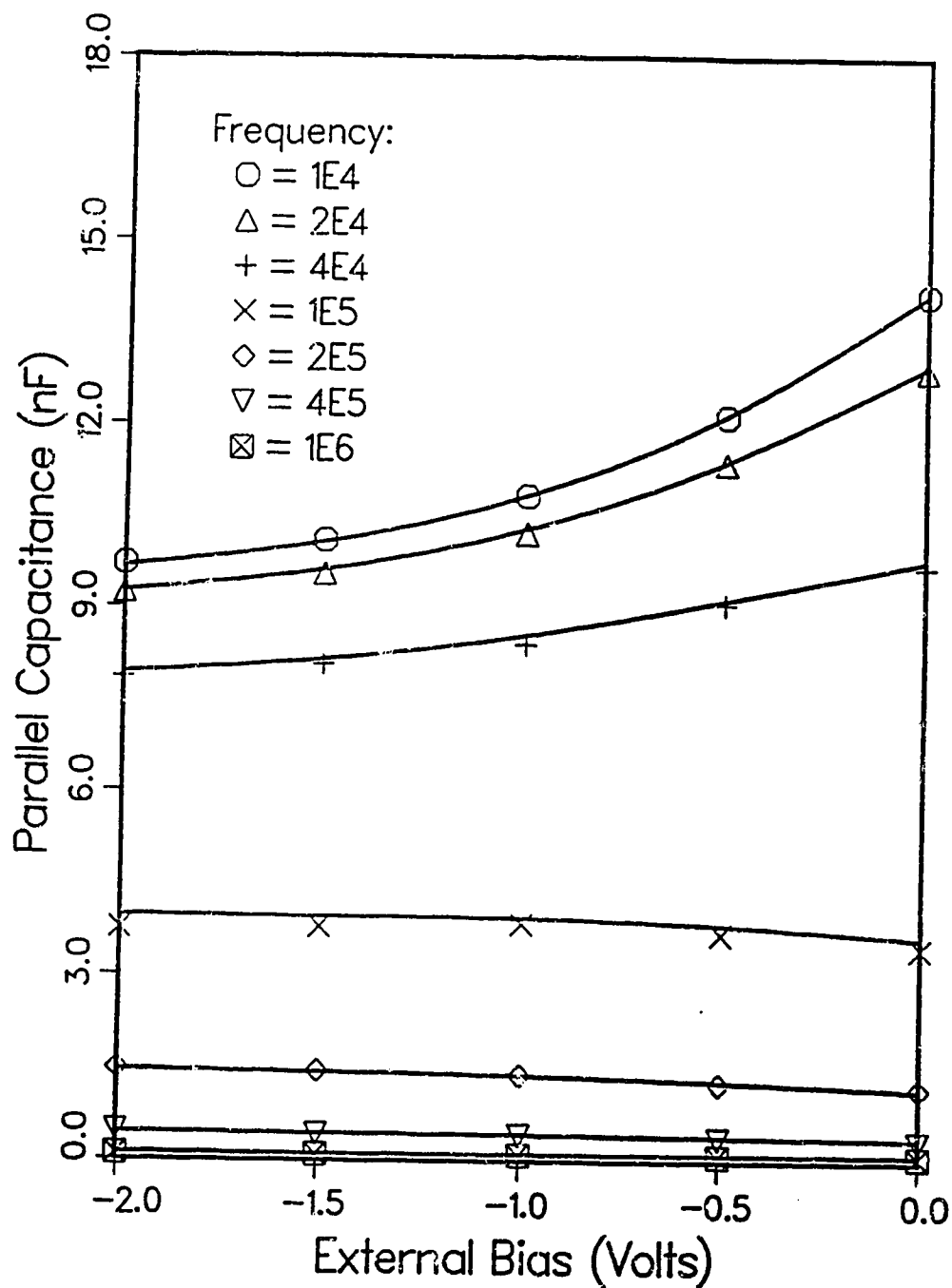


Fig. 4.7 Equivalent parallel capacitance as function of reverse bias at different frequency for sample 405C. The symbols represent the experimental results while the solid lines represent the corresponding theoretical results calculated with $N = 24$.

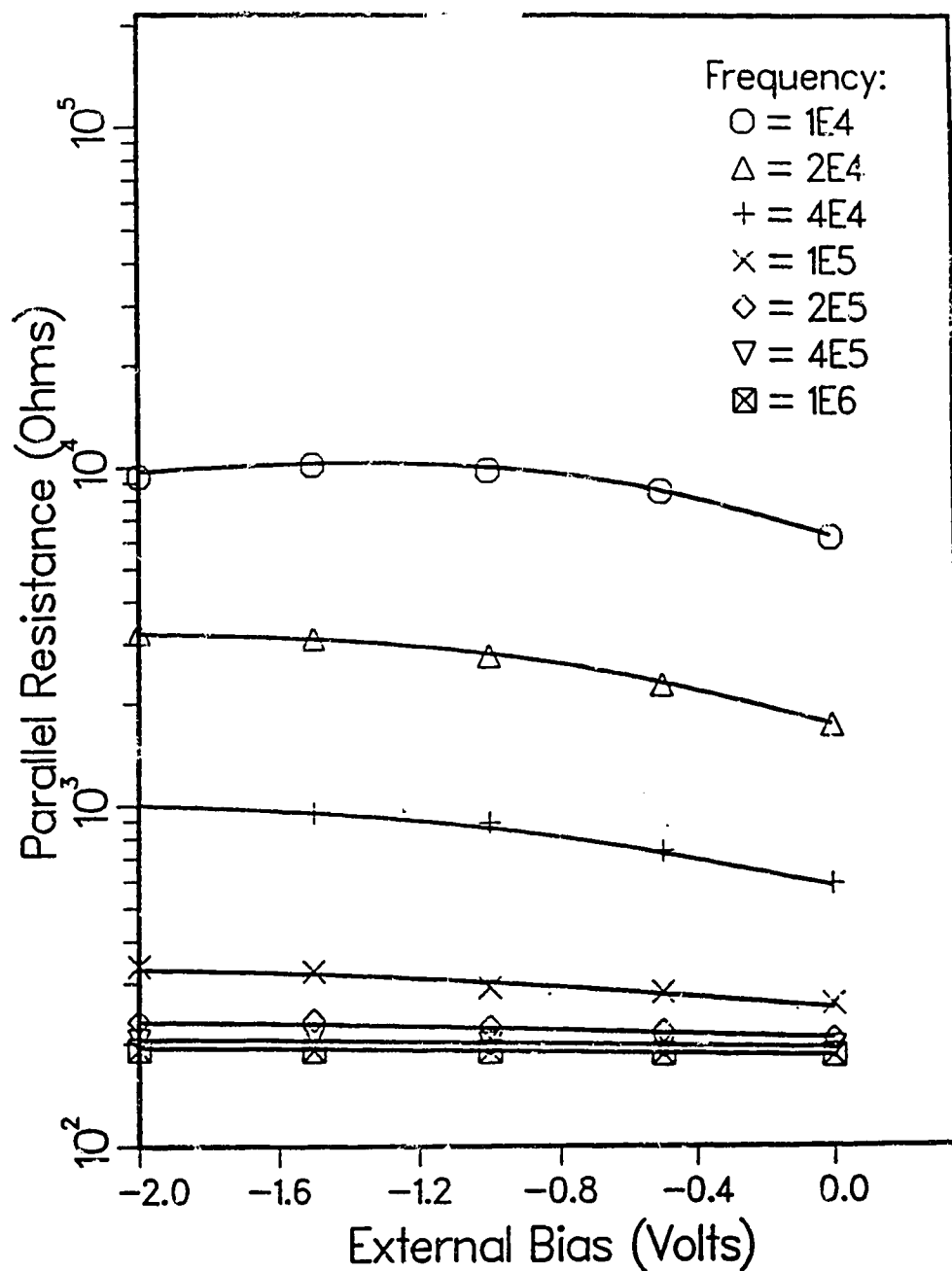


Fig. 4.8 Equivalent parallel AC resistance as function of reverse bias at different frequency for sample 405C. The symbols represent the experimental results while the solid lines represent the corresponding theoretical results calculated with $N = 24$.

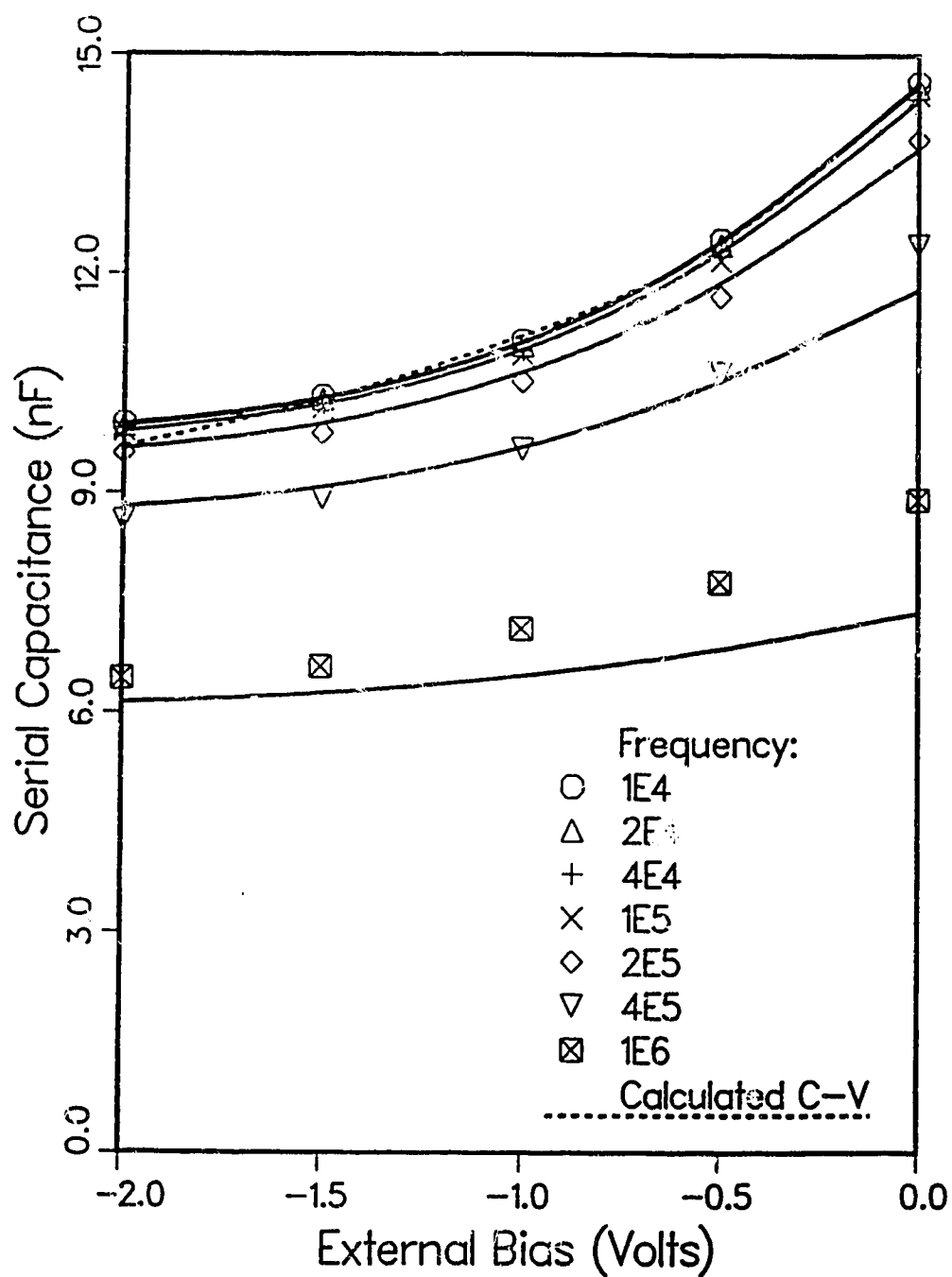


Fig. 4.9 Equivalent serial capacitance as function of reverse bias at different frequency for sample 405C. The symbols represent the experimental results while the solid lines represent the corresponding theoretical results calculated with $N = 24$. There is one solid curve for each of the seven frequencies. The dotted curve gives the results of calculation where we assume C is proportional to $(V_b + V_{bi})^{-1/3}$, with $V_{bi} = 0.8V$.

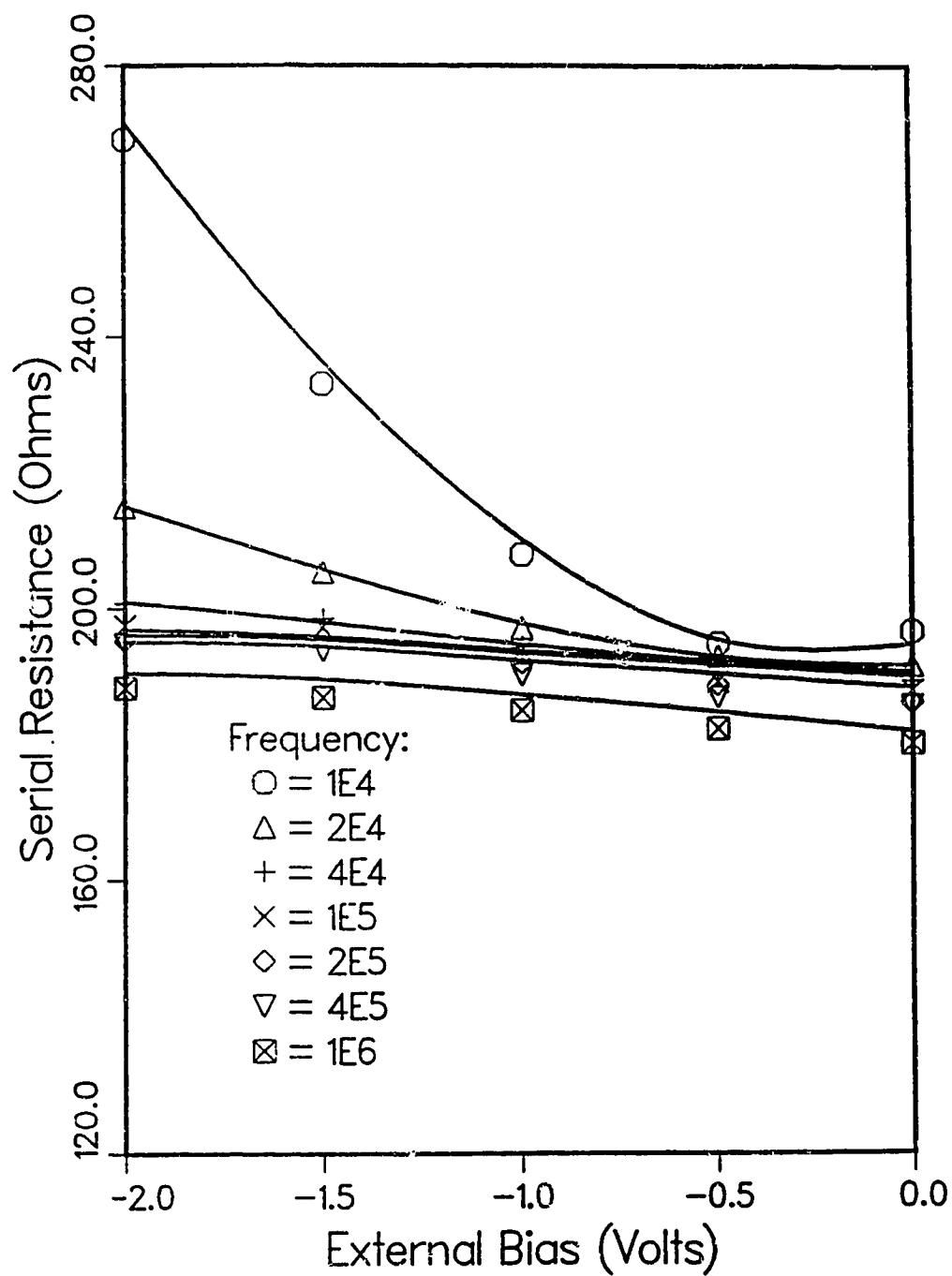


Fig. 4.10 Equivalent serial AC resistance as function of reverse bias at different frequency for sample 405C. The symbols represent the experimental results while the solid lines represent the corresponding theoretical results calculated with $N = 24$. There is one solid curve for each of the seven frequencies.

in value due to the fact that W_1 (see Figure 2.4) has a dimension which ranges from $90\mu\text{m}$ to $140\mu\text{m}$. The theoretical results shown in Figure 4.6 were calculated using the model of Figure 4.3 with the number of lumps $N = 12$. The values of their discrete elements are shown in Table 4.2. Using (4.3), the 3 dB frequency is calculated to be approximately 3.1×10^5 Hz, which agrees well with experimental results.

The experimental and calculated results in Figures 4.7 to 4.10 are for sample 405C at different frequencies and with an external bias applied to the superlattice. The theoretical results for $N = 24$ (shown by full lines) agree well with the measured equivalent parallel capacitance and AC resistance values shown in Figures 4.7 and 4.8, respectively. The different values of the parameters used in the calculation for different bias are given in Table 4.2. It is to be noted that the values of N equal to 12 and 24 were chosen for sample 405B and 405C, respectively, because the calculated results have been shown to approach a limit. Also, curve fitting was simply carried out by trial and error and visual inspection. The increase in values of C_j and R_p , as the bias is reduced, is consistent with diode characteristics. The agreement between the calculated values given by the theoretical model of Figure 4.3 and experimental results is poorer, particularly at higher frequencies for the equivalent serial capacitance and AC resistance (as illustrated in Figures 4.9 and 4.10).

These discrepancies may be caused by the stray capacitances and inductances introduced by the complex structure of the doping superlattice shown in Figure 2.4.

The dotted curve in Figure 4.9 is the calculated capacitance as a function of reverse bias voltage assuming capacitance is proportional

Table 4.2. Values of the discrete circuit elements for samples 405B and 405C. These values for samples 405B and 405C were used in the calculations with $N = 12$ and $N = 24$, respectively.

Sample	405C			
	405B	-2	-1	0
Bias (Volts)	-2	-2	-1	0
$R_{sc} + R_c$ (ohms)	35.30	68.13	68.13	68.13
R_p or R_n (ohms)	3.44	8.26	8.10	7.90
R_ℓ (1×10^6 ohms)	0.32	0.82	3.00	7.00
C_j (nF)	0.7634	0.413	0.4613	0.6089

to $(V_b + V_{bi})^{-1/3}$, where V_{bi} is 0.8V [64]. This proportionality starts to deviate from the experimental data at about 2V reverse bias. This implies that for the range of reverse bias used, the doping profile is approximately linearly graded. In general, this fact does not contradict the secondary ion mass spectrometry (SIMS) measurements [23] as shown in Figure 4.11. If the effective area of the p-n junction for sample 405C is 0.35mm x 1.2mm, with 19 p-n junctions (20 layers), the impurity gradient is estimated to be $3.4 \times 10^{23} \text{ cm}^{-4}$, with a depletion width of about 570 Å for each p-n junction. Figure 4.12 shows that the net serial AC resistance of the superlattice (shown by resistance values at high frequency), varies by only about 5% when the bias changes from 0V to -2V. This small change in the layer resistance is confirmed by the transconductance measurement. The change in the layer resistance is largely due to the decrease in the conducting thickness in the layers as the depletion regions increase in thickness when the reverse bias is increased. It is also assumed here that $R_c + R_{cs}$ remains a constant as the reverse bias changes.

DLTS measurements on sample 405B were carried out by us at Dr. Webb's Laboratory at NRC and by Dr. Zukotynski at the University of Toronto [74]. The measurements were carried out with capacitance meters operating at 1 MHz (Webb) and at 10 KHz (Zukotynski). At 1MHz no meaningful signal was observed. Figure 4.12 shows the DLTS results at 10 kHz for sample 405B. From the curves shown in this figure and using standard analysis [68], an estimated trap energy level of 0.03 eV was obtained. It appears that the trap is a shallow one. However, it is doubtful that DLTS run at 10 kHz would be able to measure such a trap. Three possible reasons for these inconclusive results are: a)

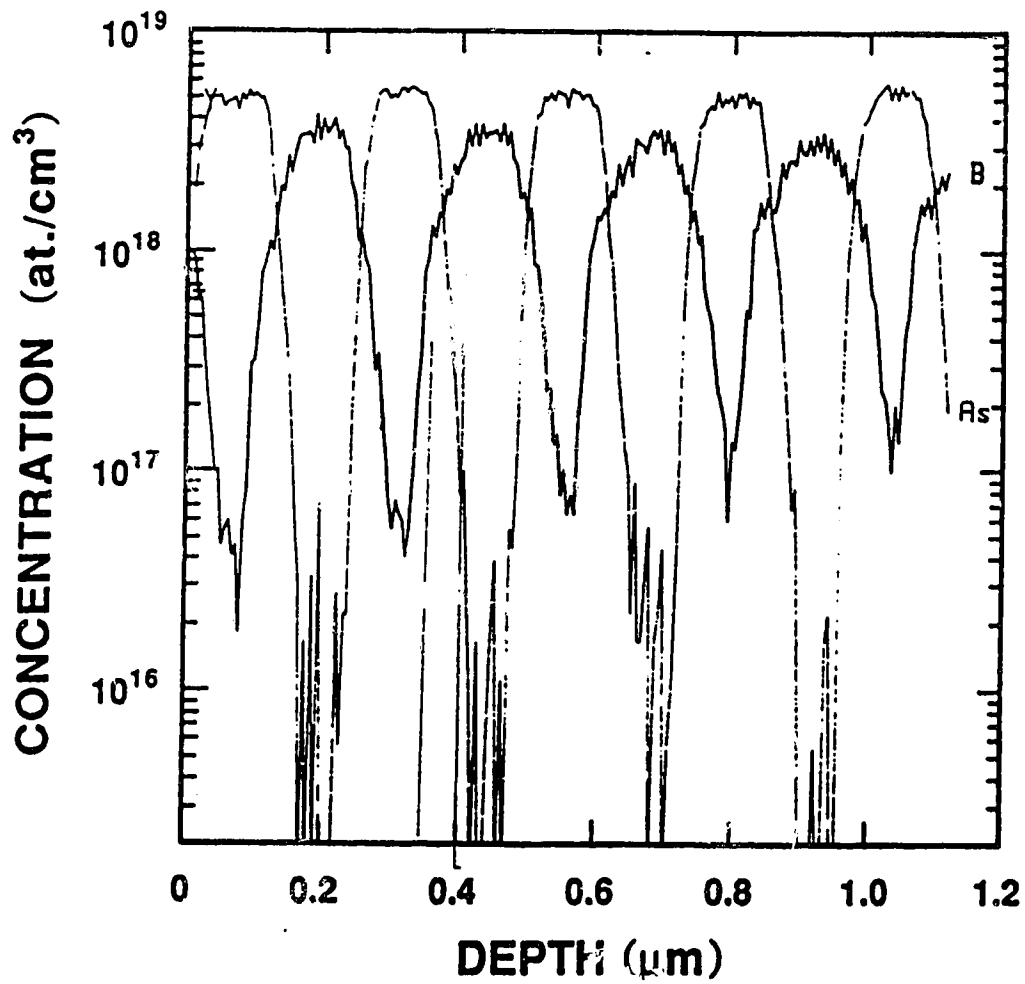


Fig. 4.11 Simultaneous SIMS profile of a sample taken from wafer 405 obtained with 14.5 keV/ion Cs⁺ beam. The detected species were B⁻ and As⁻

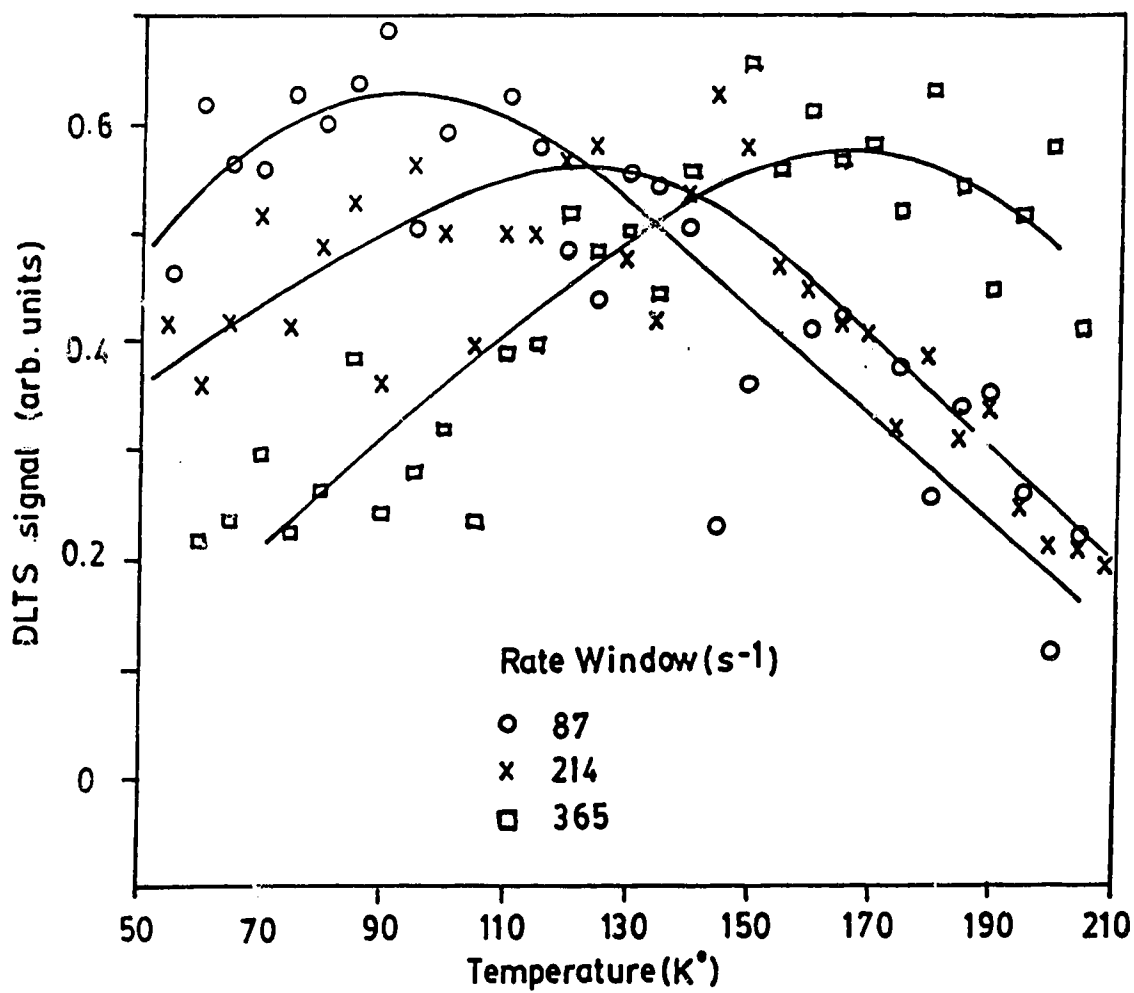


Fig. 4.12 Experimental DLTS spectra for traps (sample 405B).

the capacitance transient is non-exponential which makes the standard DLTS analysis invalid; b) the assumption that the capture cross sections of the traps are independent of temperature is generally not valid which may lead to a shift in the measured energy level relative to the true level and c) the doping profile is spatially dependent which may require a more sophisticated analysis than the one given by Lang [68,75].

Chapter 5

Two-Dimensional Properties of Electrons

Considerable work on the two-dimensional properties of electrons and holes in structures such as MOS inversion layers [76,77] and heterostructures [78,79] has been carried out during the past 20 years.

It has been shown that the two-dimensional structures may demonstrate new effects which do not exist in the bulk of the material. Phenomena, such as the quantum Hall effect and enhanced carrier mobility, have been shown experimentally to exist [80,5].

In this chapter and the next, the two-dimensional properties of electrons and holes in a Si doping superlattice are explored. For the two-dimensional study of electrons, Si doping superlattices with narrow, highly-doped n layers and broad, lightly-doped p layers are used. Similarly, for the holes, doping superlattices with narrow, highly-doped p layers and broad, lightly-doped n layers are used. Such systems will result in the formation of subbands. As in the MOS inversion layer [76], the carrier concentrations as well as the subband energies can be controlled by an external bias. The main advantage of using a doping superlattice instead of a MOS inversion layer in the study of two-dimensional properties of carriers is the absence of the Si/Si dioxide interface which is known to introduce complications to both theory and experiment. These complications arise, for example, from carriers trapped in the surface states, from stress and strain due to lattice mismatch, and from the difference in dielectric constants on both sides of the interface [81].

This chapter is concerned with the study of two-dimensional

properties of electrons. Section 5.1 studies the tunability of the effective bandgap and carrier concentration in a Si doping superlattice. Section 5.2 examines the effect of exchange-correlation in the electron subbands. The effects of the physical parameters of the doping superlattice, such as doping concentrations and layer thicknesses, on the two-dimensional properties are also studied. (A version of Section 5.1 and 5.2 has been published. See References 18 and 20)

5.1 Tuning the Effective Bandgap

In this section, we calculate the primary tunability of two of the quantities (see Chapter 2), the electron concentration and the effective bandgap, in a Si doping superlattice with narrow, highly-doped n-layers and broad, lightly-doped p-layers subjected to an external bias through selective contacts. Such a structure would be expected to show quantization of the motion of the electrons, but not of the holes, in the narrow potential wells which are formed in the ultrathin n-layers. The bandgap tunability is expressed in terms of a dimensionless parameter, T_B , defined as the ratio of the change in the effective bandgap energy to the change in the difference between the electron and hole quasi-Fermi energy levels. In the case of an external bias, the latter is just the applied potential. The approach used is to solve iteratively the one-dimensional Schrödinger equation for the envelope of the electron wave function in the effective mass approximation. We assume a self-consistent Hartree potential which consists of the "bare" space charge potential modified by a thermal distribution of the electrons in the bound states of the quantum well.

In each run the electron concentration is held constant and the corresponding external bias is determined during the course of the calculation. In this way, the variation of the effective bandgap and the electron concentration with the external bias can be determined from a series of runs. As in a Si MOS structure [76], the multi-valley bandstructure, the narrow potential wells, and the anisotropic effective mass of the electrons give rise to more than one subband system. This makes the calculation of the subband energies more involved than in the case of GaAs doping superlattices, such as reported by Döhler [81], particularly for non-zero temperatures when more than the lowest subbands are filled.

The section is organized as follows. The superlattice structure being studied and the basic assumptions about it are described in Section 5.1.1. Details of the calculations are described in Section 5.1.2 and the results are presented and discussed in Section 5.1.3. The results presented will show the tunability at different ambient temperatures for various design parameters such as the doping concentration, the thickness of the layers and the external bias. The variation of the carrier concentration with the external bias is also discussed.

5.1.1 Potential Wells in a Doping Superlattice

Figure 5.1 shows a doping superlattice made of ultrathin layers of n-doped Si alternating with relatively thick layers of p-doped Si. The doping profiles are assumed to be abrupt and the doping concentrations N_D and N_A are constant in the respective doping layers. Assuming that the n-doped layers ($0 \leq |z| \leq d_n/2$, $|z \pm d| \leq d_n/2$, ...) are totally

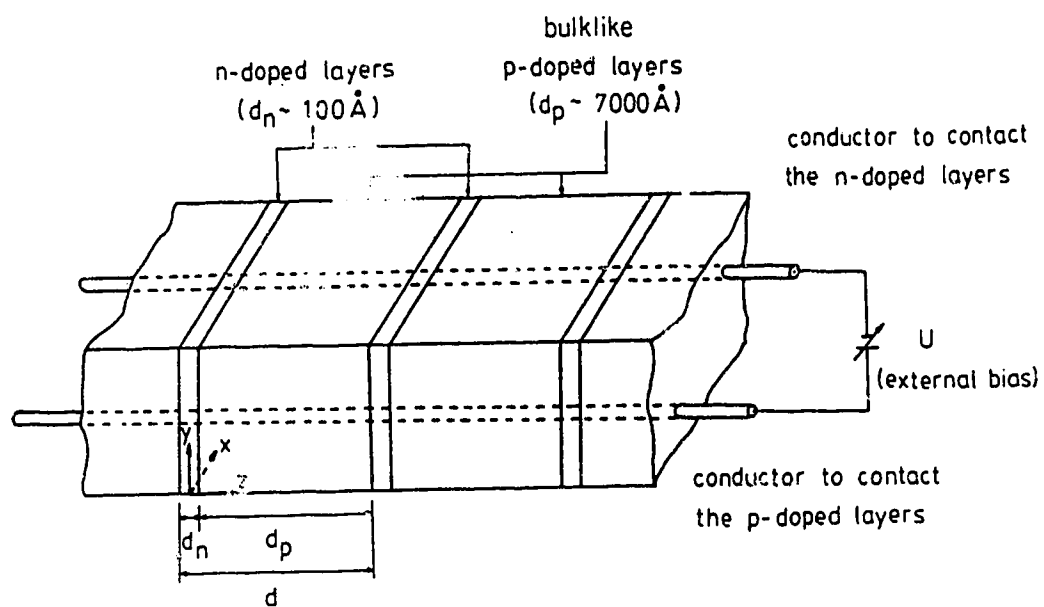


Fig. 5.1 A doping superlattice structure with selective contacts for external biasing.

depleted of free electrons and using the depletion approximation for the space-charge regions in the p-doped layers [81], the electric potential $V_b(z)$ is obtained from Poisson's equation. For the range of electron concentrations in the n-doped wells ($0 \leq n^{(2)}/N_D d_n \leq 0.4$), and the values of N_D and N_A used here, the depletion approximation can be used in the computation of $V_b(z)$. For the single well about $z = 0$, $V_b(z)$ is given by

$$V_b(z) = \begin{cases} \frac{e}{2\epsilon} N_D z^2 & \text{for } 0 \leq |z| \leq d_n/2 \\ \frac{e}{2\epsilon} \left[N_D (d_n/2)^2 + (z - d_n/2) (N_D d_n - N_A (z - d_n/2)) \right] & \text{for } d_n/2 \leq |z| \leq d_n/2 + z_A, \end{cases} \quad (5.1)$$

where the length z_A of the space charge region in the p-doped material is such that electrical neutrality is satisfied,

$$n^{(2)} = N_D d_n - 2N_A z_A. \quad (5.2)$$

In the above, $n^{(2)}$ is the density of the electrons per unit area in the n-doped layers, e is the electron charge and ϵ is the dielectric permittivity. Various values of $n^{(2)}$ can be obtained by applying an external bias between the n-doped and the p-doped layers using selective contacts (see Figure 5.1) and/or by optical excitation. The maximum value of z is obtained for $n^{(2)} = 0$; $(z_A)_{\max} = (N_D d_n)/2N_A$. In all cases considered in this chapter, $d_p \geq (z_A)_{\max}$.

The ultrathin and heavily doped n-layers form potential wells for the electrons which are so narrow that the electron motion in the well

along the z direction becomes quantized. This results in a two-dimensional "subband" structure for the unrestricted motion in the x and y directions, i.e., parallel to the interfaces. We use the envelope-function approximation which has been called "a simple, accurate and very flexible method for the calculation of this subband structure" [82]. In the given case, the electric potential of the electrons generated in a well by biasing the superlattice structure (see Figure 5.1) is added to the electric potential of the donors in the computation of the self-consistent Hartree potential.

In contrast, due to the greater thickness of the p -doped layers ($5,000 \text{ \AA} < d_p \leq 10,000 \text{ \AA}$) which is assumed in this chapter, all physical properties of the holes in the p -doped layers will remain approximately the same as in bulk p -type Si. In addition, the n -doped potential wells for electrons shown in Figure 5.2 are sufficiently isolated from one another so that the analysis can be confined to one single potential well. The effects from coupled bulk bands at the degenerate valence band edge in ultrathin p -type layers [21,22] will be considered in Chapter 6.

5.1.2 Calculation of the Self-Consistent Potential and the Tunability

The effective bandgap E_g^{eff} is defined [33] as the energy difference between the lowest conduction subband and the edge of the valence band

$$E_g^{\text{eff}} \equiv E_g^0 - eV_o + E_{c,11}, \quad (5.3)$$

where E_g^0 is the bandgap of bulk Si, V_o is the depth of the potential

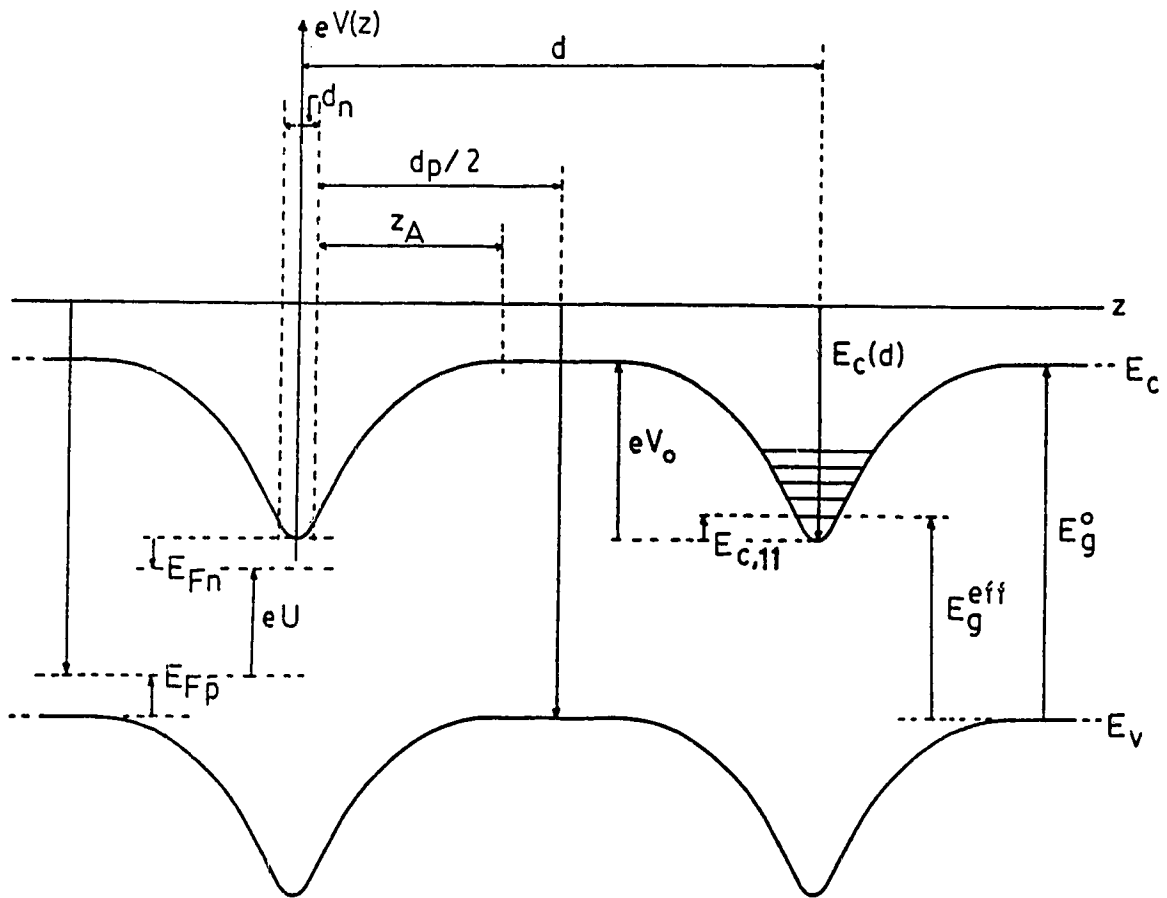


Fig. 5.2 Energy diagram for a Si doping superlattice. U is the external bias between the n-doped and p-doped layers.

well measured from the edge of the conduction band, and $E_{c,11}$ is the energy of the lowest conduction subband measured from the bottom of the potential well. It is clear from Figure 5.2 that the effective bandgap, aside from being indirect in k -space (due to the bulk properties) is also an indirect bandgap in real space.

The electric potential $V(z)$ in the doping superlattice structure is obtained by the Hartree method [76]:

$$V(z) = V_b(z) + V_H(z), \quad (5.4)$$

where $V_H(z)$ is the contribution to the potential by the free electrons in the n -doped layer given by

$$\frac{\partial^2 V_H(z)}{\partial z^2} = - \frac{e}{\epsilon} \sum_{ij} n_{ij} |\psi_{ij}(z)|^2 \quad (5.5)$$

Here, n_{ij} is the two-dimensional electron concentration for the j th subband of the i th subband set and

$$n^{(2)} = \sum_{ij} n_{ij} \quad (5.6)$$

is the total two-dimensional electron concentration in a well.

The electron envelope wavefunctions ψ_{ij} (see (5.5)), and energy eigenvalues $E_{c,ij}$ are obtained by solving Schrödinger's equation in the z direction

$$\left[-\frac{\hbar^2}{2m_{zi}} \frac{\partial^2}{\partial z^2} + eV(z) \right] \psi_{ij}(z) = E_{c,ij} \psi_{ij}(z); \quad \begin{array}{l} i = 1, 2. \\ j = 1, 2, 3.. \end{array} \quad (5.7)$$

Equation (5.7) describes the wave envelope functions ψ_{ij} for the one-dimensional motion of an electron in a well along the z direction. The subscript j labels the number of the subband, i.e., the number of the electron envelope wave eigenfunction for the quantized motion in the z direction. If the doping layers have (100) surface orientation in Si with z denoting the direction perpendicular to the layer surfaces, then $i = 1, 2$ label the two different effective masses (longitudinal and transverse) of electrons moving in the z direction [76].

The n_{ij} are determined from Fermi-Dirac statistics,

$$n_{ij} = D_{ij}(E) P_{ij} \quad (5.8)$$

where

$$P_{ij} = k_B T \ln \left[\exp \left(-\frac{E_{c,ij} - E_{Fn}}{k_B T} \right) + 1 \right] \quad (5.9)$$

and where

$$D_{ij}(E) = \frac{1}{\pi \hbar} g_i \sqrt{m_{xi} m_{yi}} H(E - E_{c,ij}) \quad (5.10)$$

is the two-dimensional density of states for the j th subband of the i th subband set; g_i is the valley degeneracy, m_{xi} and m_{yi} are the effective masses in the x and y directions, respectively [76]. $H(x) = 1$ if $x \geq 0$, $H(x) = 0$ otherwise (see Figure 5.3). From (5.6), (5.8), (5.9)

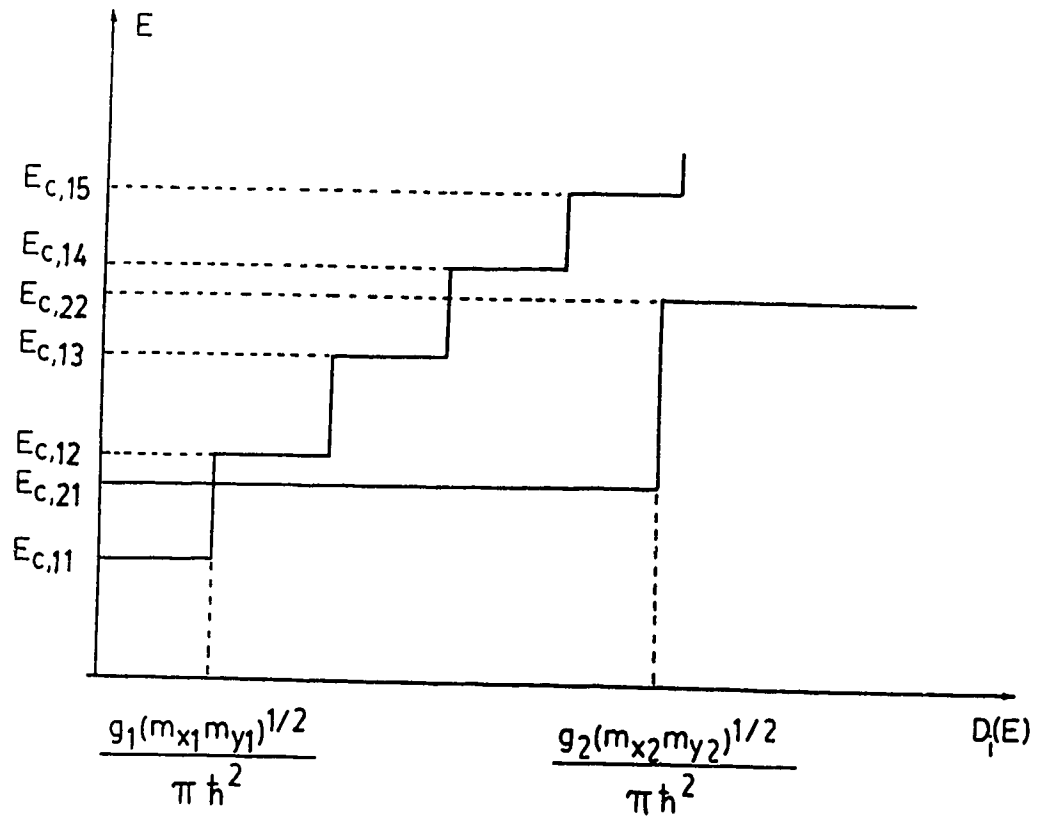


Fig. 5.3 Energy state densities for two-dimensional electrons in Si [76]. $D_i(E) = \sum_j D_{ij}(E)$, where j is the subband number and i labels the effective mass of electrons in the z direction, in Si (100); $i = 1, 2$.

and (5.10) the Fermi energy E_{Fn} (measured from $E_c(0)$, see Figure 5.1) of the electrons is determined.

The self-consistent calculation starts with an initial computation letting $V(z) = V_b(z)$. Using (5.7) we determine the eigenvalues $E_{c,ij}$ and envelope wavefunctions ψ_{ij} . With these calculated values, and for a given $n^{(2)}$, the electron concentrations n_{ij} for each subband are determined through (5.6), (5.8)-(5.10). These values are then used to determine the Hartree potential $V_H(z)$ by (5.5), which in turn gives rise to a new value for $V(z)$ in (5.4). This process is repeated until a self-consistent solution is reached. From this the final value of the depth of the potential well, V_o , is found. The quasi-Fermi level ϕ_p in p-doped bulk Si is found from Reference 83. The quasi-Fermi levels ϕ_n and ϕ_p , the depth of the potential well V_o , the bulk energy gap E_g^o , and the external bias U are related by (see Figure 5.2)

$$eU = E_g^o + E_{Fn} - E_{Fp} - eV_o \quad (5.11)$$

where

$$eU = \phi_n - \phi_p \quad (5.12)$$

$$E_{Fn} = \phi_n - E_c(0) \quad (5.13)$$

$$E_{Fp} = \phi_p - E_v(d/2) \quad (5.14)$$

$$eV_o = E_c(d/2) - E_c(0) . \quad (5.15)$$

In order to provide a quantitative measure of the effectiveness of the bandgap tuning, we introduce a quantity which we call the

tunability, T_B . We define "tunability" of the effective bandgap, T_B , as a measure of the change in the effective bandgap per unit change in the quasi-Fermi level difference (see (5.11)),

$$T_B \equiv \frac{\Delta E_g^{\text{eff}}}{\Delta(eU)} \quad (5.16)$$

where the quasi-Fermi energy level difference corresponds to the external potential, eU (in electron volts). Since for a given temperature E_g^0 remains approximately constant, it follows from (5.3), (5.11) and (5.16) that

$$T_B = \frac{-\Delta(eV_o) + \Delta E_{C,11}}{-\Delta(eV_o) + \Delta E_{Fn} - \Delta E_{Fp}}. \quad (5.17)$$

Since E_{Fp} can be assumed to be approximately constant for all cases considered in this chapter, and at higher temperatures $|\Delta E_{C,11}| \ll |\Delta eV|$,

$$T_B = \frac{\Delta(eV_o)}{\Delta(eV_o) + |\Delta E_{Fn}|} \quad (5.18)$$

The tunability of the electron concentration may be defined as the ratio of the change in the electron charge in one period of the superlattice to a change in the external bias potential. A dimensionless parameter, T_E , is obtained by dividing by the capacitance of the same p-n-p layer in the depletion approximation, C_{dpl} ;

$$T_E = \frac{\Delta n^{(2)} / \Delta eU}{C_{dpl}} . \quad (5.19)$$

This tunability is related to the bandgap tunability by

$$T_E = T_B \cdot \frac{\Delta n^{(2)} / \Delta(eV_o)}{C_{dpl}} \quad (5.20)$$

In our calculations, T_E never varies from T_B by more than 1% at 30°K and 3% at 300°K. This is an indication of the extent to which the computed self-consistent potential varies from that obtained from the depletion approximation. All numerical results and discussion of the bandgap tunability given in the next section apply to the electron concentration tunability as well.

5.1.3 Results and Discussion

The results of these self-consistent calculations show that the value of the effective bandgap is essentially determined by the electronic charge in the n-doped layers (see Figure 5.4). The small differences between cases (b) and (c) shown in Figure 5.4 are explained by the fact that in (b) the potential well is narrower and N_D is larger, which results in slightly higher subband energies. The results in Figure 5.4 show further that the effective bandgap is not a very sensitive function of temperature. However, we observe that both E_g^{eff} and $\Delta E_g^{\text{eff}} / \Delta(n^{(2)} / N_D d_n)$ for a given value of $n^{(2)} / N_D d_n$ are somewhat larger at lower temperatures. This is readily explained by noting that with higher temperature the bulk energy bandgap E_g^0 decreases, and in

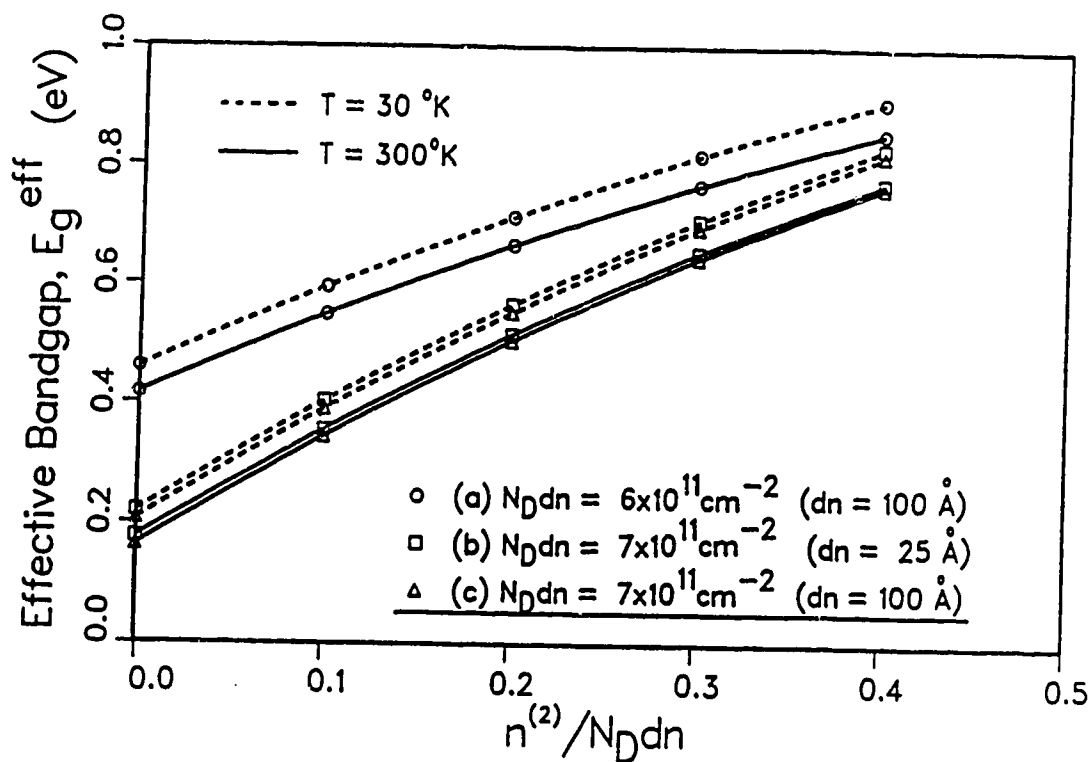


Fig. 5.4 Effective bandgap in a Si doping superlattice versus the normalized planar electron concentration in the n-doped layers. In this case, $N_A = 1 \times 10^{16} \text{ cm}^{-3}$.

the n-doped potential well more electrons occupy energy levels that belong to broader envelope wave functions. As a result, this makes for smaller Hartree contributions to the potential well.

Figure 5.5 shows an almost linear relation between the external bias and some of the subband energy edges. For example E_{11} and E_{13} belong to the first and third subband of electrons with the heavier effective mass in z direction. E_{21} and E_{22} belong to the first and second subband of electron with the smaller effective mass in z direction.

Figures 5.6 to 5.8 were calculated for small values of concentrations of electrons in the n-doped wells, $0.1 \leq n^{(2)}/N_{Dn} \leq 0.2$. Figure 5.6 demonstrates that for a constant planar donor charge density N_{Dn} , the tunability of the effective bandgap is largely independent of the thickness of the n-doped layers. Figure 5.7 shows that the tunability increases with increasing planar charge density N_{Dn} . This is due to the fact that $|\Delta E_{Fn}|$ becomes a smaller percentage of $\Delta(eV_o)$ as the charge density, N_{Dn} , in the n-doped layers increases. Figure 5.8 shows that the tunability decreases as temperature increases. The results in these figures are consistent with (5.18): for lower temperatures, $|\Delta E_{Fn}|$ can be neglected against $\Delta(eV_o)$ and consequently T_B approaches unity; for higher temperatures, $|\Delta E_{Fn}|$ cannot be neglected against $\Delta(eV_o)$.

The calculated temperature dependence of the tunabilities can be understood in terms of the energy dependence of the electron wavefunctions obtained. The value of $\Delta(eV_o)$ in (5.18) is determined mainly by N_{Dn} and is relatively insensitive to temperature. At low temperatures, the electrons occupy only the lowest subbands and $|\Delta E_{Fn}|$

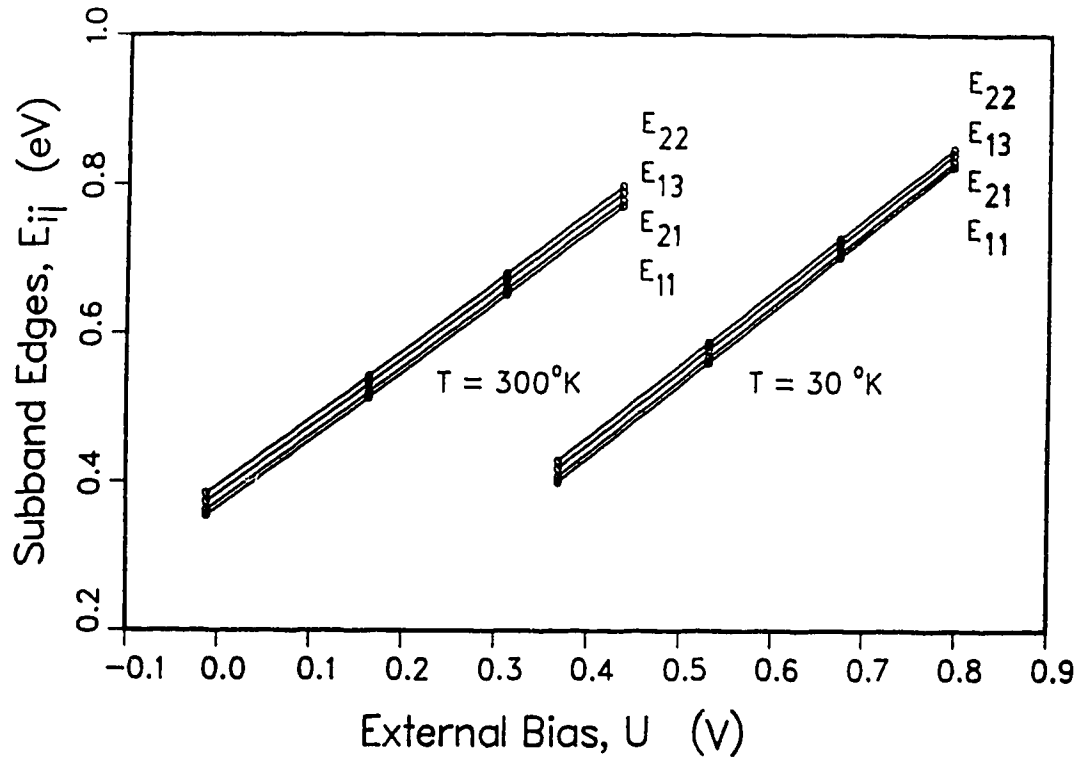


Fig. 5.5 Energy of subband edges (against the valence band edge) versus the external bias. $E_{ij} = E_g^{\text{eff}} - eV_o + E_{c,ij}$; $E_{11} \equiv E_g^{\text{eff}}$ (see (5.3)). $N_D = 2.8 \times 10^{18} \text{ cm}^{-3}$, $d_n = 25 \text{ \AA}$, $N = 1 \times 10^{16} \text{ cm}^{-3}$.

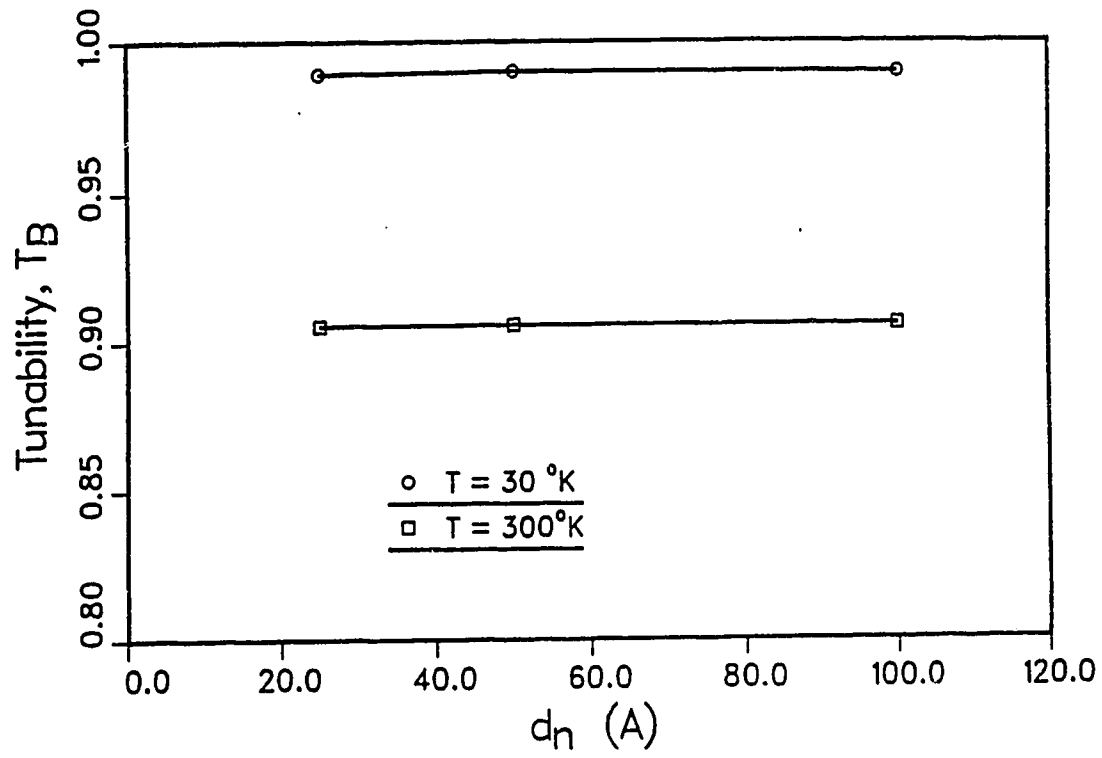


Fig. 5.6 Tunability of the effective bandgap (see (5.16)) as a function of the thickness of the n-doped layer. $N_A = 1 \times 10^{16} \text{ cm}^{-3}$, $N_D d_n = 7 \times 10^{11} \text{ cm}^{-3}$.

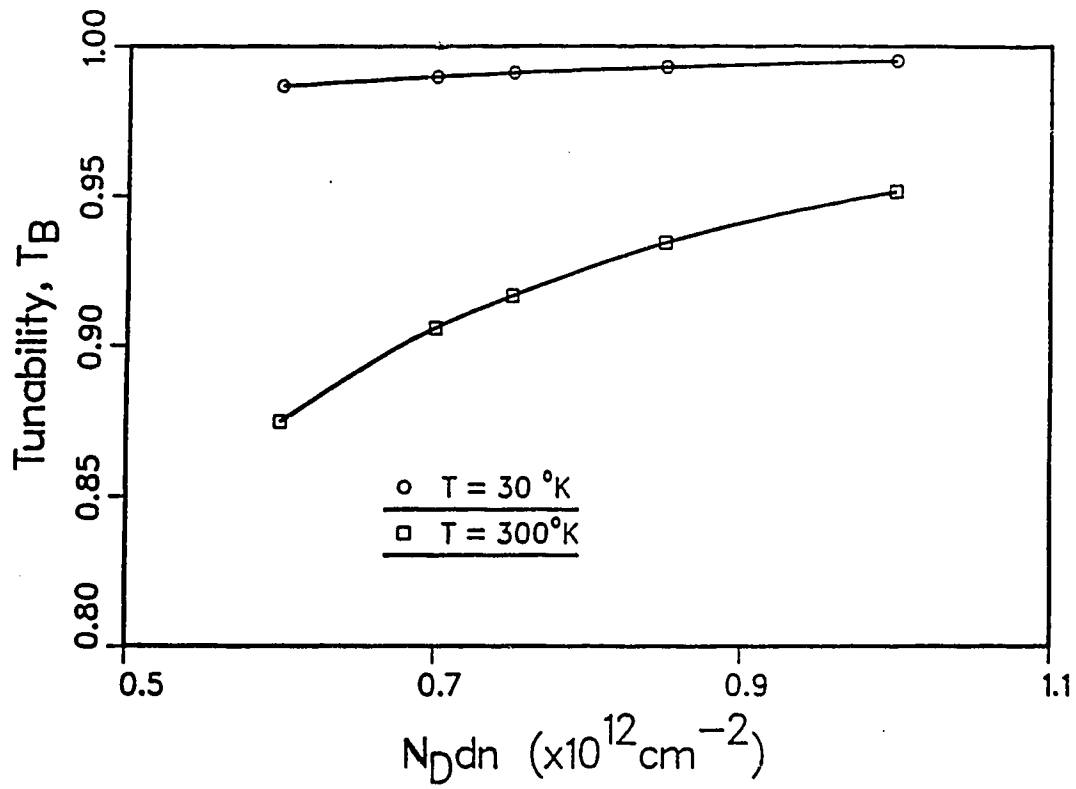


Fig. 5.7 Tunability of the effective bandgap [see (5.16)] as a function of the planar donor charge density (N_{Dn}) per square centimeter of the n-doped layer. $N_A = 1 \times 10^{16} \text{ cm}^{-3}$.

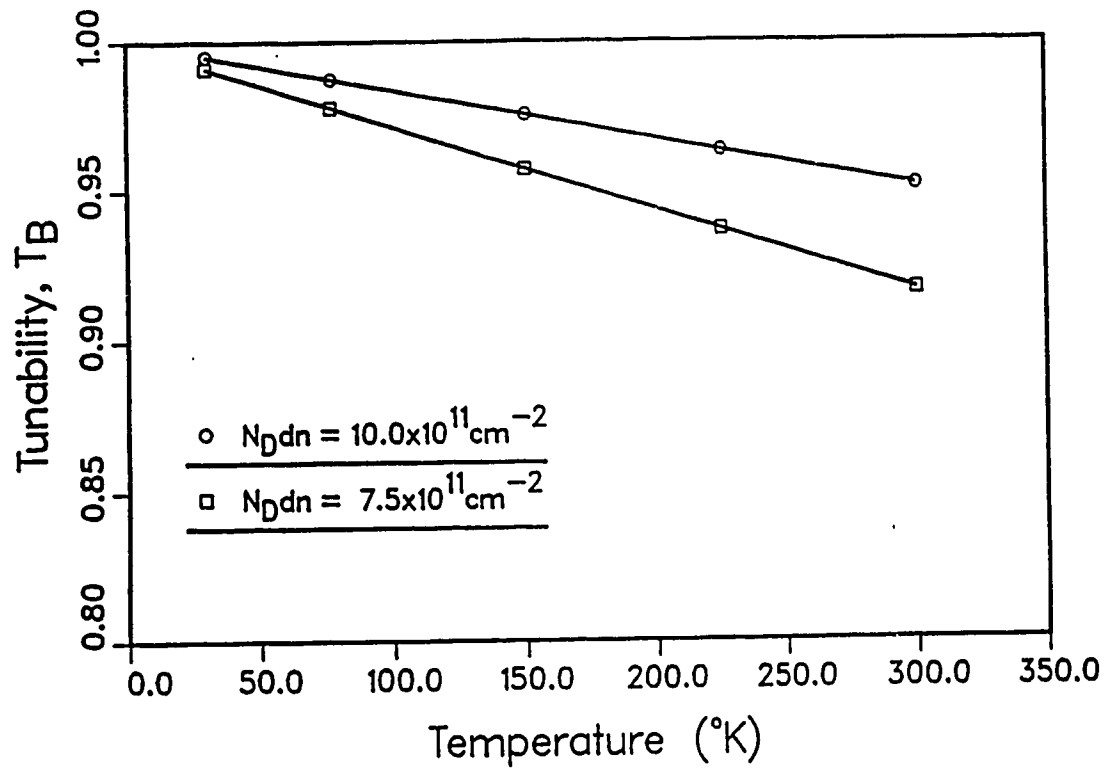


Fig. 5.8 Tunability of the effective bandgap (see (5.16)) as a function of temperature. $N_A = 1 \times 10^{16} \text{ cm}^{-3}$.

varies little with $n^{(2)}$; hence $\Delta(eV_o)$ dominates over $|\Delta E_{Fn}|$ and the tunability is close to unity. At higher temperatures, some of the electrons will be found in more energetic subbands (see (5.9)) resulting in larger values of $|\Delta E_{Fn}|$ and reduced tunability. The carrier tunability, T_E , directly measures the dynamic capacitance of a superlattice layer. A decrease in the tunability means that fewer electrons are injected into the superlattice at higher temperatures for a given external bias. In the case of optical excitation, it means that the measured change in the external potential due to an increase of carriers should be greater at higher temperatures.

5.2 Exchange-Correlation Energy in the Subbands

In Section 5.1, self-consistent calculations of the electron energy levels in a doping superlattice were based on the Hartree approximation [81,18], which does not include the exchange interaction of the electrons. This approximation is acceptable when the average kinetic energy of the electrons is much greater than the average interaction energy [84]. When this is not the case, the Hamiltonian which determines the single-particle wave functions should include the exchange interaction in some approximation. Ruden and Döhler [85] included the exchange energy, in the form of a Kohn-Sham potential [86,87], in calculations for GaAs doping superlattices. For low concentrations, their results indicated a change on the order of 10% in the splitting between occupied and nearest-neighbor subband energies when the exchange interaction was included in this way. As shown in the next paragraph, it is expected that the effect should be at least as prominent in Si doping superlattices. Moreover, it has been shown

that the exchange interaction is important in Si MOS structures [88,89]. The influence of the exchange interaction on the electron energy levels in Si and GaAs doping superlattices is the topic of this section.

The wave functions and energies obtained by Ruden and Döhler [84] were calculated self-consistently as in the Hartree approximation. Since these calculations are carried at $T = 0^\circ\text{K}$, the problem of freezing out of the donors is first considered in Section 5.2.1. The criteria that determine the values of the doping level of the n-type layers used in a doping superlattice are also discussed. In Section 5.2.2, self-consistent calculations of the electronic band-structure in both Si and GaAs as a function of the charge-carrier concentration are presented. In addition, an improved form of the exchange potential as described by Ando [88] is used. A discussion of the results is given in Section 5.2.3.

5.2.1 Freezing out of the Donors

As the calculation is carried out at $T = 0^\circ\text{K}$, the problem of freezing out of the carriers cannot be ignored. As suggested by Priester et al. [19], the existence of free carriers will decide whether the space charge model or the self-consistent calculations should be used. The former method of calculation assumes that all free carriers are frozen out and there exists a distinct impurity band. The latter method assumes the existence of a free carrier gas, a phenomenon which will occur when the impurity bands merge into the continuum. To date, there has been no work done on the conditions for the existence of an impurity band in a quantum confined system at $T = 0^\circ\text{K}$. Therefore

as in Priester et al. [19], we will use the conditions given by the bulk system as a guide to set the lower limits to the doping levels for the existence of free carriers. This assumption is supported by the fact that the theoretical values of the carrier concentrations in GaAs n-pis have been shown to be in good agreement with experimental results and that there is no indication that they are affected by its quantum confined system [49]. Hence the criteria for whether the space charge model or the self-consistent calculations should be used are [19]:

(a) for the formation of the impurity band;

$$P_I^{1/3} a^* < 0.13 \quad (5.21)$$

(b) for the merging of the impurity band into the continuum;

$$P_I^{1/3} a^* > 0.43 \quad (5.22)$$

Here, P_I is the doping concentration and a^* is the Bohr radius given by

$$a^* = a_0 \epsilon_r m_0^* / m^* \quad (5.23)$$

where m^*/m_0 is the effective mass of the electron (in units of the ordinary electron mass) in the energy subband under consideration, ϵ_r is the relative dielectric constant and a_0 is the Bohr radius.

In the case for GaAs and Si doping superlattices, minimum doping levels required in which donor impurity bands merge into the conduction band continuum are $8 \times 10^{16} \text{ cm}^{-3}$ and $2 \times 10^{19} \text{ cm}^{-3}$, respectively. In the

calculations to follow, the doping levels chosen will assume the merging of the bands.

5.2.2 Self-Consistent Calculations

Due to the many-valley bandstructure of Si, the basic equations used for the computation of the subband energies must be expanded as follows. The one-particle Schrödinger equation including the exchange and correlation potential is given by:

$$\left[-\frac{\hbar^2}{2m_{z1}} \frac{d^2}{dz^2} + eV_b(z) + eV_{eff}(z) \right] \psi_{ij}(z) = E_{c,ij} \psi_{ij}(z) \quad (5.24)$$

where $j = 1, 2, 3, \dots$ is the j^{th} subband of the i^{th} subband set, and for Si (100), $i = 1, 2$ correspond to the two different effective masses of electrons moving in the z direction. $V_b(z)$ is the bare potential given by (5.1) (based on the depletion approximation) whose values will depend on the parameters of the superlattice such as layer widths and doping concentrations [18,85]. V_{eff} is the "effective potential",

$$V_{eff}(z) = V_H(z) + V_{ex}(z) \quad (5.25)$$

where

$$V_{ex}(z) = \frac{e}{4\pi^2 \epsilon} \left(\frac{3\pi^2 n(z)}{g_1} \right)^{1/3} \beta \quad (5.26)$$

Here, $V_H(z)$ is given by (5.5) and $n(z)$ is the local electron concentration given by

$$n(z) = \sum_{ij} n_{ij} |\psi_{ij}(z)|^2 \quad (5.27)$$

where n_{ij} is the two-dimensional electron concentration for the j th subband of the i th subband set, and where g_i is the valley degeneracy of the i th subband set. Everywhere, we are using the effective-mass approximation and the envelope method [18,84] to separate variables in the wave functions. In (5.26), β is the correlation enhancement factor given by

$$\beta = 1 + \int_0^\infty dq \int_0^\infty \frac{d\omega}{4\pi} \left(1 - \frac{1}{\epsilon(q, i\omega q)} \right) \ln \left[\frac{(2+q)^2 + \omega^2}{(2-q)^2 + \omega^2} \right] \quad (5.28)$$

where q is the wave vector and the dielectric function $\epsilon(q, i\omega q)$ is given by Ando [88], but here excludes the interaction with images of other electrons in a neighbouring layer of a different dielectric constant. We assume that the effect of the anisotropy of the effective mass is small [18] for Si. At $T = 0$, only the lowest energy band will be occupied (the first subband in the first set of subbands) for the cases considered here.

5.2.3 Results and Discussion

From (5.24) to (5.28) above, numerical results have been obtained for wave functions and subband energies of Si and GaAs doping superlattices for three different cases: pn^+p , $pnpn$, and $nipi$. In all of these cases, we have only presented the energy levels for the lowest three subbands. For the large spatial separations of the wells

considered here the wells are essentially "single" wells, that is there is minimal overlap of the wave functions between neighbouring wells. For comparison, we also present results obtained by setting β to unity in (5.26) in which case the exchange potential is identical to that used by Ruden and Döhler [85] in their calculations for GaAs.

Figures 5.9 and 5.10 show results for the subband splitting in Si and GaAs pn^+p doping superlattices. We have assumed the same doping concentrations and layer thicknesses in both cases. Figures 5.11 and 5.12 illustrate the subband energies and the self-consistent potential wells. As well, the wavefunction of the lowest subband is shown. Other results for different electron concentrations in this type of superlattice are presented in Table 5.1. Table 5.2 summarizes some results for $pnpn$ and $nipi$ superlattices.

Our numerical results show that the exchange-correlation effect plays a more important role in Si than in GaAs doping superlattices. This can be explained by the fact that the Si has a much higher effective mass than that of GaAs which results in more a localized wave function as can be seen by comparing Figures 5.11 and 5.12. In turn, this gives rise to a higher electron concentration at the center of the potential well. Consequently, the exchange-correlation potential is larger at the center of the well in Si doping superlattices than in the GaAs type. Our results seem to imply that while the higher valley degeneracy in Si tends to reduce the Kohn-Sham potential, it is more than offset by the stronger localized wave function.

Figures 5.9 to 5.12 and Tables 5.1 and 5.2 indicate that the correlation enhancement factor has a more significant effect in Si than in GaAs doping superlattices. When it is included in Si, the

correction to the subband splitting energies due to exchange-correlation is increased by approximately 20% whereas in GaAs it has virtually no effect. Again, this is due to both the higher values of the effective mass and the valley degeneracy of Si which results in a higher value of β . Higher temperature effects have not been considered here. However, as in the MOS structure, it is to be expected that the exchange-correlation effect will be reduced at a higher temperature [90].

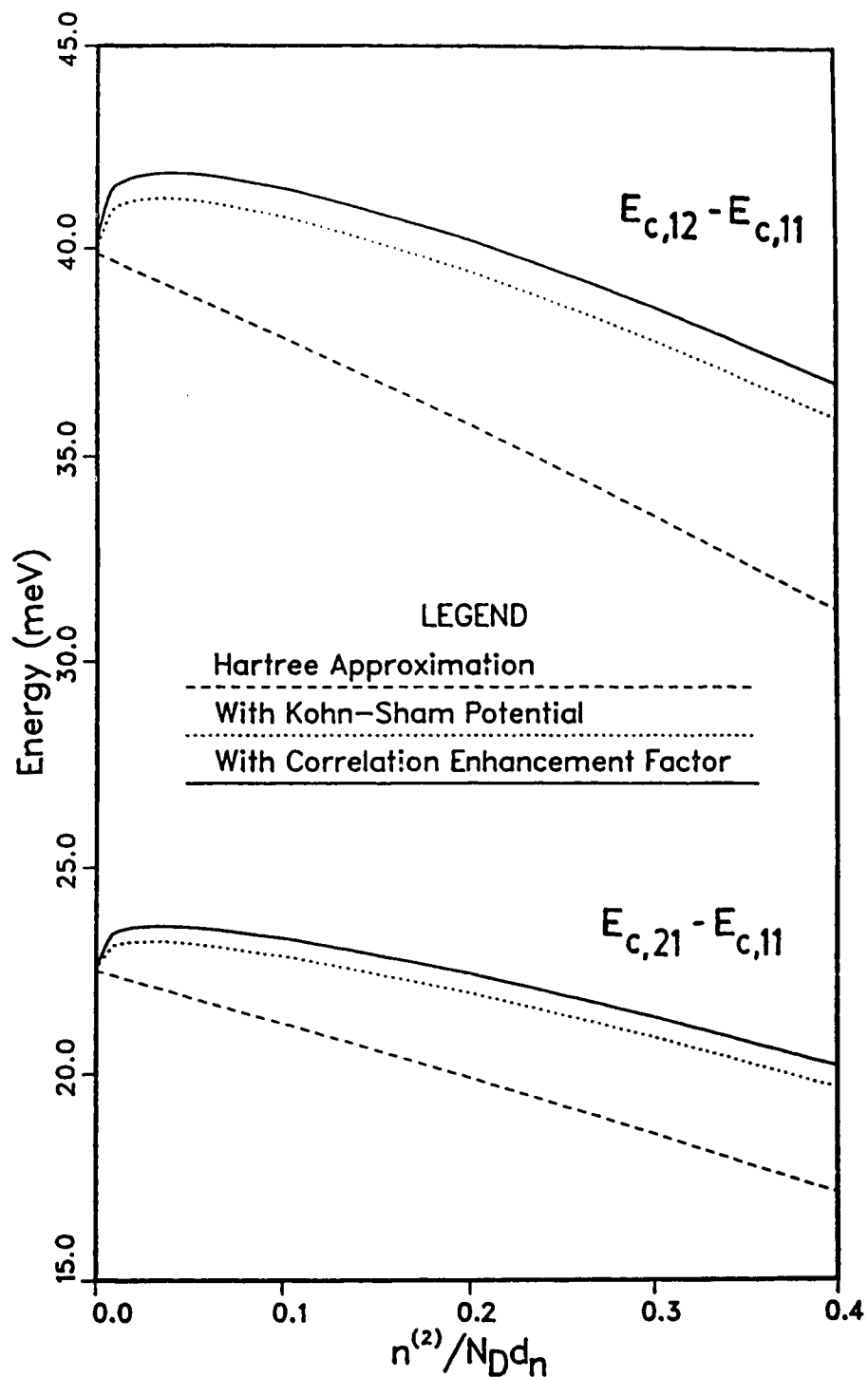


Fig. 5.9 Differences in subband energies calculated with the Hartree Approximation, with the exchange energy and with the correlation enhancement factor in a Si^{I} pn^+p doping superlattice. $N_D = 2 \times 10^{19} \text{ cm}^{-3}$, $N_A = 2 \times 10^{17} \text{ cm}^{-3}$, $d_n = 20 \text{ \AA}$ and $d_p = 2000 \text{ \AA}$.

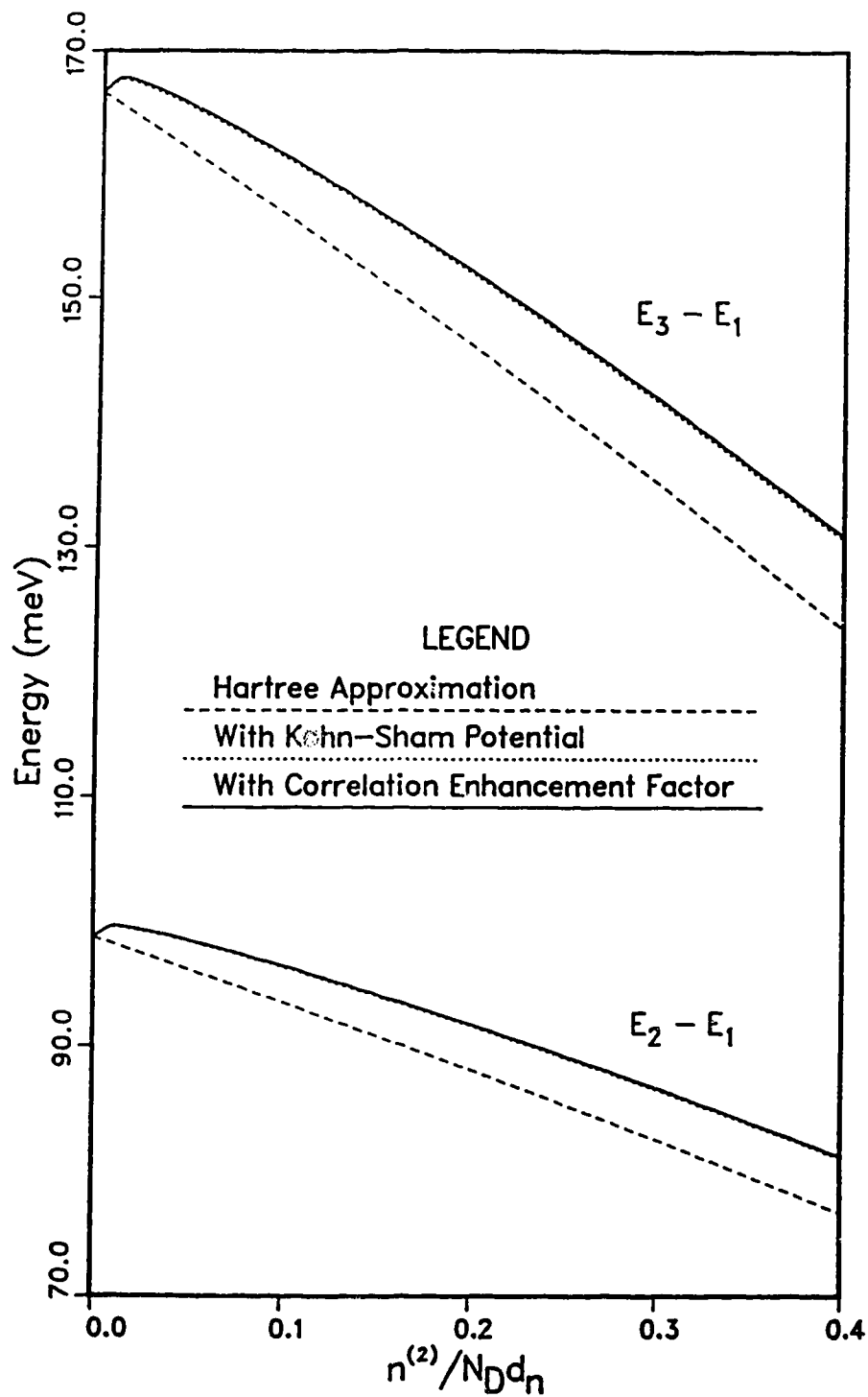


Fig. 5.10 Differences in subband energies calculated with the Hartree Approximation, with the exchange energy and with the correlation enhancement factor in a GaAs pn^+p doping superlattice. $N_D = 2 \times 10^{19} \text{ cm}^{-3}$, $N_A = 2 \times 10^{17} \text{ cm}^{-3}$, $d_n = 20 \text{ \AA}$ and $d_p = 2000 \text{ \AA}$.

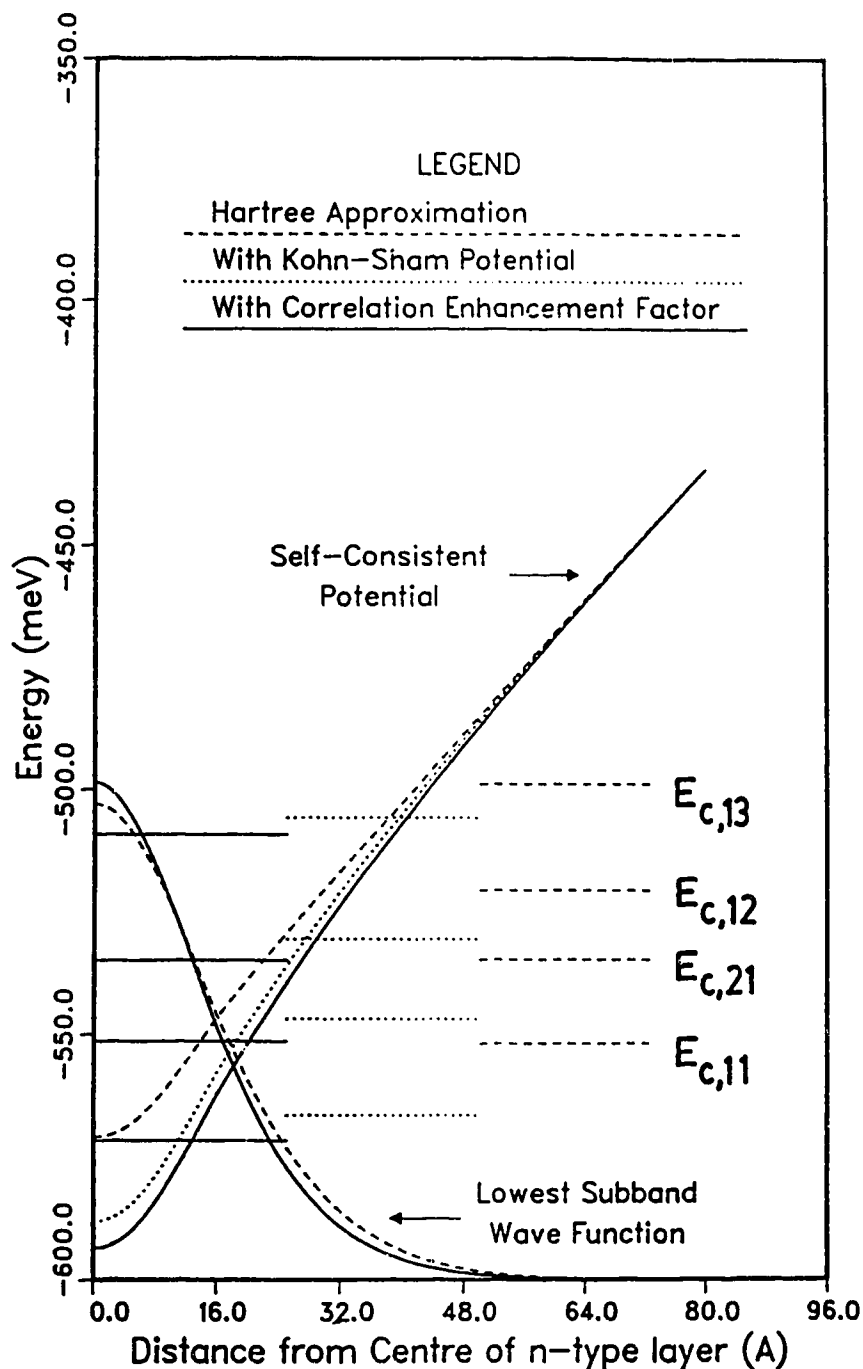


Fig. 5.11 Subband energies and the self-consistent potential as calculated in the Hartree Approximation, with exchange energy and with correlation enhancement factor in a Si pn p doping superlattice. $N_D = 2 \times 10^{19} \text{ cm}^{-3}$, $N_A = 2 \times 10^{17} \text{ cm}^{-3}$, $d_n = 20 \text{ Å}$, $d_p = 2000 \text{ Å}$ and $n^{(2)} = 1.6 \times 10^{12} \text{ cm}^{-2}$. The point of reference for the energy is the conduction band edge in the non-depleted region of the p-doped layers.

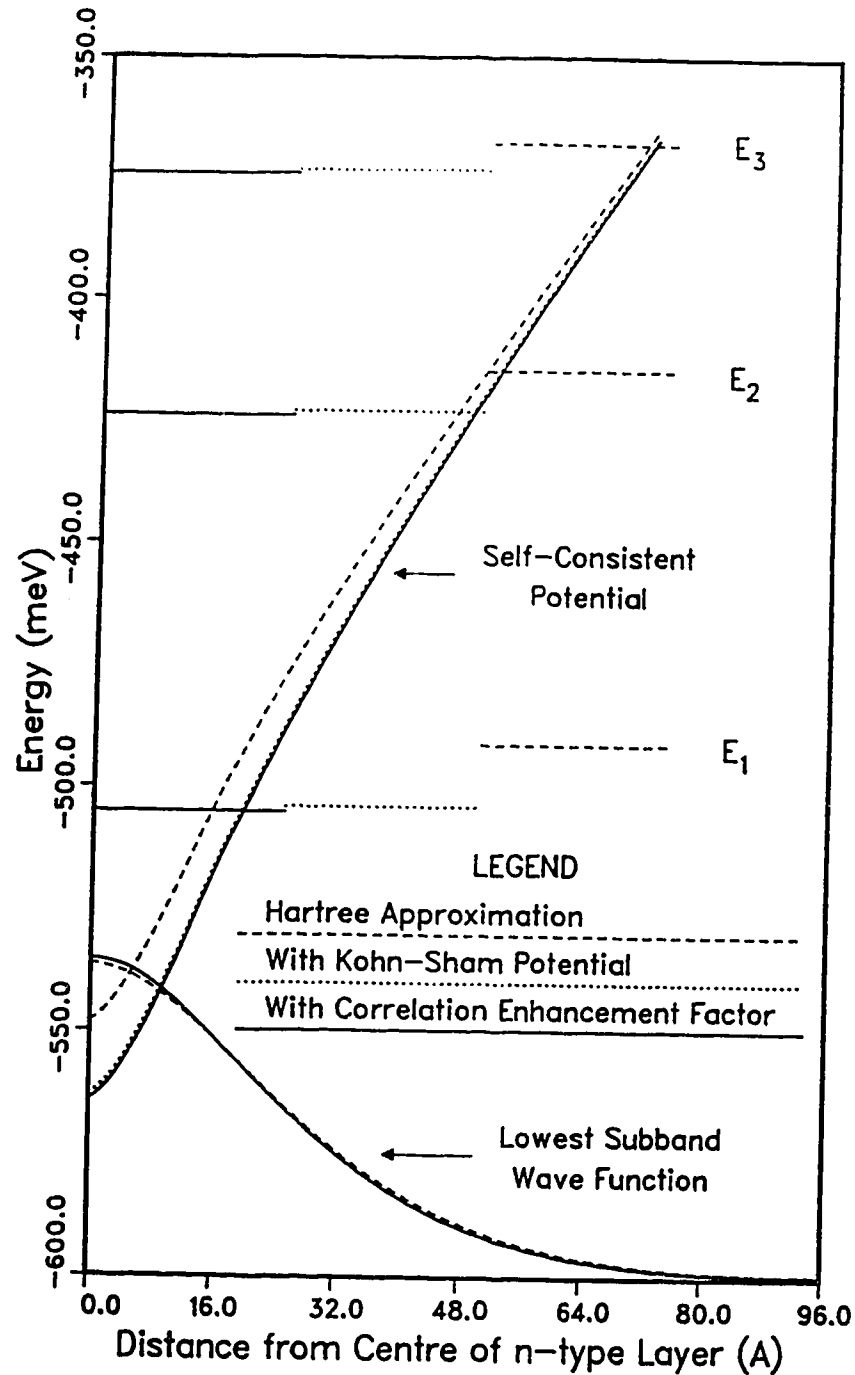


Fig. 5.12 Subband energies and the self-consistent potential as calculated in the Hartree Approximation, with exchange energy and with correlation enhancement factor in a GaAs pn p doping superlattice. $N_D = 2 \times 10^{19} \text{ cm}^{-3}$, $N_A = 2 \times 10^{17} \text{ cm}^{-3}$, $d_n = 20 \text{ Å}$, $d_p = 2000 \text{ Å}$ and $n^{(2)} = 1.6 \times 10^{12} \text{ cm}^{-2}$. The point of reference for the energy is the conduction band edge in the non-depleted region of the p-doped layers.

Table 5.1 The correction to the subband energies for different values of electron concentration in a pn^+p doping superlattice when the exchange energy and the correlation enhancement factor is included. ΔE_{KS} is the difference between the subband energy calculated in the Hartree Approximation and that calculated using the Kohn-Sham potential. ΔE_{CEF} is the difference when the correlation enhancement factor is included. $N_D = 2 \times 10^{19} \text{ cm}^{-3}$, $N_A = 2 \times 10^{17} \text{ cm}^{-3}$, $d_n = 20 \text{ \AA}$ and $d_p = 2000 \text{ \AA}$.

Host Material	$n^{(2)}/N_D d_n$	$\Delta E_{KS} \text{ (meV)}$			$\Delta E_{ECF} \text{ (meV)}$		
		0.02	0.1	0.4	0.02	0.1	0.4
Si	$E_{c,11}$	5.76	9.76	14.63	9.16	14.06	19.71
	$E_{c,21}$	4.82	8.13	12.08	7.85	12.00	16.64
	$E_{c,12}$	4.07	6.83	10.00	6.88	10.43	14.24
GaAs	E_1	5.06	8.56	12.79	5.83	9.46	13.80
	E_2	3.42	5.76	8.40	4.08	6.55	9.29
	E_3	2.39	3.98	5.61	2.95	4.66	6.35

Table 5.2 Same as Table 5.1 except for pnpn and nipi doping superlattices.

		Si $\Delta E_{KS}(\text{meV})\Delta E_{ECF}$			GaAs $\Delta E_{KS}(\text{meV})\Delta E_{ECF}$	
pnpn $N_A = N_D = 2 \times 10^{19} \text{ cm}^{-3}$ $d_n = d_p = 250 \text{ \AA}$ $n^{(2)} = 3 \times 10^{12} \text{ cm}^{-2}$						
	$E_{c,11}$	18.28	23.82	E_1	17.88	19.01
	$E_{c,21}$	16.15	21.32	E_2	13.58	14.60
	$E_{c,12}$	13.97	18.86	E_3	10.90	11.85
nipi $N_A = N_D = 2 \times 10^{19} \text{ cm}^{-3}$ $d_n = d_p = 40 \text{ \AA}$ $d = 400 \text{ \AA}$ $n^{(2)} = 3.2 \times 10^{12} \text{ cm}^{-2}$						
	$E_{c,11}$	18.50	24.05	E_1	17.13	18.24
	$E_{c,21}$	15.89	21.00	E_2	11.88	12.88
	$E_{c,12}$	13.93	18.80	E_3	8.17	9.02

Chapter 6

Two-Dimensional Properties of Holes

Much of the earlier work concerning two-dimensional hole gas has been done on metal-semiconductor-oxide (MOS) structures. With the progress made in molecular beam epitaxy, a number of different kinds of two-dimensional structures, using one or more materials, have been made and studied [84]. Structures such as MODFETs (modulated doped field effect transistors), heterostructures, and doping superlattices are but some examples.

In general, the calculation of the subband energies for holes in a quasi 2-D structure is much more complex than for electrons due to the fact that the hole bands couple with each other. The 2-D subband structure in a p-channel inversion layer in a Si MOS transistor was first calculated by E. Bangert et al. [77,91] and by Ohkawa and Uemura [92]. In this chapter, a different method (developed by Dr. W. Allegretto, U. of A.) for such calculations in quasi 2-D Si structures is presented. The results of calculations of the subband energies and the density-of-states mass of holes of a p-channel Si inversion layer at $T = 0^\circ\text{K}$ are described as an illustration of the method. This method is also applied to the doping superlattice structure. The main advantage of investigating a doping superlattice rather than an inversion layer in a MOS structure is outlined in Chapter 5.

Two-dimensional properties of electrons in GaAs [81] and Si [18] doping superlattices have been investigated theoretically but so far no work has been done on the two-dimensional properties of holes. It is the objective of this work to attempt to fill this gap. As illustrated

both theoretically and experimentally, the confinement of holes in the inversion layers has the ability to alter and to reduce the hole masses as compared to their bulk values, an effect which may be important when one considers the transport properties of the holes [77]. Results for the inversion layers indicated that hole masses can be reduced with lower hole carrier planar density, here referred to as the hole concentration. However, the problem with the inversion layer is that the depth of the electric potential and the degree of confinement of the holes increases with hole concentration. This makes it difficult to work experimentally at low hole concentrations. Doping superlattices, however, have the opposite effect; that is, the depth of the electric potential increases with decreasing hole concentrations. Since the two-dimensional holes concentrations can be easily controlled by external bias via selective contacts [26], hole masses at low levels of hole concentrations can be studied, a region which may be interesting due to the possibility of reduced hole mass.

In this chapter the results of the calculations of the subband energies and the density-of-states mass of holes in a Si and Ge doping superlattices at $T = 0^\circ\text{K}$ are described. Due to the fact that our calculations were carried out at low temperature, we first address the problem of the freezing out of the acceptors. The criteria that determine the values of the doping level of the p-type layers used in a doping superlattice are also discussed. The effect of the three physical parameters of the doping superlattice, namely, the doping levels of the p and n-type layers and the thickness of p-type layers on the density-of-states masses of holes are investigated. Finally, we will compare the properties of the 2-D hole gas in a doping

superlattice to that of the MOS structures. (A version of this chapter has been accepted for publication. See References 21 and 22)

6.1 Freezing Out of the Acceptors

The self-consistent calculation of the subband energies in a quasi 2-D doping superlattice structures will depend on the existence of free carriers. Due to the highly complex nature of the problem, our calculation is confined to the case where $T = 0^\circ\text{K}$. At non-zero temperature, the problem involves having to handle not only a large number of subbands but also subbands whose density-of-states cannot be determined by explicit analytical formulae.

Since our calculation is carried out at $T = 0^\circ\text{K}$, the problem of freezing out of the carriers has to be taken into consideration. As mentioned in Section 5.2.1, the existence of free carriers will decide whether the space charge model or the self-consistent calculations should be used. Expression (5.21) has been used to calculate the maximum doping concentration for which a distinct impurity band will exist. Below this concentration, the carriers are frozen out and space-charge model should be used. Likewise, expression (5.22) has been used to calculate the minimum doping concentration for which the acceptor impurity band will be merged with the valence band continuum. Above this concentration, there will be free carriers and self-consistent calculations should be used. Between these two concentrations, it is not clear which model should be used. The values of these concentrations for GaAs, Si and Ge are given in Table 6.1.

In the next section, the new method of computation will be described. It will be shown that the results calculated by the method

Table 6.1 Doping levels for the formation and merging of the impurity bands as described in the text.

Host Material	ϵ_r	m^*/m_o	Maximum doping concentration for space-charge model (cm^{-3})	Minimum doping concentration for self- consistent calculations (cm^{-3})
GaAs	12.5	0.5	9×10^{17}	3×10^{19}
Si	11.7	0.49	1×10^{18}	4×10^{19}
Ge	15.8	0.28	8×10^{16}	3×10^{18}

for the MOS inversion layer compares favourably with experimental data, as well as with those calculated by other authors. Most of the calculation for the subband energies of Si and Ge doping superlattices are for the ranges of doping concentrations where band merging takes place.

6.2 Method of Computation

We begin by using the Kohn-Luttinger 6x6 matrix Hamiltonian [77] and the effective mass approximation. Using the Hartree approximation, the subband energies can be obtained by solving the Schroedinger and Poisson equations self-consistently. Specifically, the equations are

$$\left[H(k_x, k_y, \frac{1}{j} \frac{\partial}{\partial z}) + eV(z) \right] \psi_{\nu, k_x, k_y}(z) = E_{\nu}(k_x, k_y) \psi_{\nu, k_x, k_y}(z) \quad (6.1)$$

where H is the 6x6 Kohn-Luttinger Hamiltonian [94] (see Appendix B). The suffix ν denotes the index of the subband.

$V(z)$ in equation (6.1) is given by

$$V(z) = V_b(z) + V_H(z) \quad (6.2)$$

where

$$\frac{\partial^2 V_H(z)}{\partial z^2} = - \frac{e}{\epsilon} \left(\sum_{\text{states}} \alpha_{\nu} p^{(2)} |\psi_{\nu, k_x, k_y}(z)|^2 \right) \quad (6.3)$$

where α is the occupancy factor. At $T = 0^\circ\text{K}$ the occupied states are those with $E(k_x, k_y) \leq E_{Fp}$ the Fermi energy. This defines contours in k_x - k_y space where the number of states available within the total area,

A , enclosed by the contours is related to the total hole concentration, $p^{(2)}$, by

$$p^{(2)} = \frac{1}{4\pi^2} A. \quad (6.4)$$

For the MOS inversion layer [77], $V_b(z)$ is given by

$$\frac{\partial^2 V_b(z)}{\partial^2 z} = \frac{e}{\epsilon} (N_D - N_A) \quad (6.5)$$

For the doping superlattice using the space charge model, that is, when $P_I^{1/3} a^* < 0.13$ (see (5.23), $V(z)$ can be found by solving the Poisson equation if we assume abrupt and constant depletion regions in the doping superlattice [18]. From (6.1), the subband energies as a function of hole concentration are obtained.

In the case of the self-consistent calculation for the doping superlattices, that is, when $P_I^{1/3} a^* > 0.43$ (see (5.24), the determination of $V(z)$ and the subband energies becomes much more complicated. The "bare" potential $V_b(z)$ in (6.1) in the doping superlattice structure is

$$V_b(z) = \begin{cases} \frac{e}{2\epsilon} N_A z^2 & 0 \leq |z| \leq \frac{d_p}{2} \\ \frac{e}{2\epsilon} \left\{ N_A \left[\frac{d_p}{2} \right]^2 + \left[z - \frac{d_p}{2} \right] \left[N_A d_p - N_D \left(z - \frac{d_p}{2} \right) \right] \right\} & \frac{d_p}{2} \leq |z| \leq \frac{d_p}{2} + z_D \\ \frac{e}{2\epsilon} \left\{ N_A \left[\frac{d_p}{2} \right]^2 + z_D \left[N_A d_p - N_D z_D \right] + \left[N_A d_p - 2N_D z_D \right] \left[z - z_D - \frac{d_p}{2} \right] \right\} & |z| > \frac{d_p}{2} + z_D \end{cases} \quad (6.6)$$

where the depletion length z_D in the n-type layers is chosen to satisfy electrical neutrality,

$$p^{(2)} = N_A d_p - 2N_L z_D \quad (6.7)$$

As described in Reference 81, $p^{(2)}$ can be controlled by external bias via the selective ohmic contacts on the p^+ doped layers and the n-type bulk. The external bias is given by [18],

$$eU = E_g^0 + E_{Fn} - E_{Fp} - eV_0 \quad (6.8)$$

where U is the external bias in volts and E_g^0 is the bulk energy bandgap whose value is dependent on the doping level of the p-type layers and the n-type bulk [95]. E_{Fn} and E_{Fp} are the quasi Fermi energy levels of the p-type layers and the n-type bulk respectively. V_0 is the depth of the electric potential given by (6.2). In general, increasing the forward or reverse bias of the structure tends to increase or decrease the value of $p^{(2)}$ respectively. The limit to the reverse bias will depend on two factors, namely that $p^{(2)} > 0$ and that the voltage applied across the p-n junction must not exceed the breakdown voltage whose value is also dependent on the doping level of the n-type bulk [96]. It is to be noted that the doping superlattice structure considered in this chapter has narrow p-type and wide n-type layers so that each quantum well is isolated and the problem can be treated as a single-well problem [81].

The method of computation can be described as followed. Equations (6.1) and (6.2) constitute a nonlinear system which is to be solved iteratively subject to suitable boundary conditions. Assuming an initial $V(z)$, (6.1) is solved for $\psi_{\nu, k_x, k_y}(z)$ according to the scheme described below. Equation (6.2) is then solved by a second-order integration routine and a new $V(z)$ is generated. The process is continued until consistent values of $V(z)$ are obtained. It is assumed at this point that the holes populate only the highest (ground) subband which, because of spin, splits into two subbands, $\nu = 1$ and 2.

Standard procedures for solving (6.1) involve the expansion of ψ_{ν} into a truncated series of Airy functions [77], or more complicated expansions [92]. We have chosen to discretize (6.1) by means of a "Finite Box" method, briefly described as follows. The 1-D interval $\{a, b\}$ is subdivided into I subintervals and we set

$$\bar{\psi} = \bar{c}_{i-1}\psi_{i-1}(x) + \bar{c}_i\psi_i(x) + \bar{c}_{i+1}\psi_{i+1}(x) \quad (6.9)$$

in the i^{th} subinterval where $\{\psi_i\}$ is a system of piecewise linear functions as represented in Figure 6.1, while $\bar{c}_i = (c_i^0, \dots, c_i^5)^T$ are vectors to be determined. We construct about every interior node x_i the cell $B_i = [x_{i-1/2}, x_{i+1/2}]$ and replace $H_o \bar{\psi} = EI \bar{\psi}$ by the matrix equation:

$$\frac{1}{(x_{i+1/2} - x_{i-1/2})} \int_{B_i} H_o(\bar{\psi}) dx = \frac{E}{(x_{i+1/2} - x_{i-1/2})} \int_{B_i} \bar{\psi} dx \quad (6.10)$$

The division of (6.10) by the factor $(x_{i+1/2} - x_{i-1/2})$ is to make the

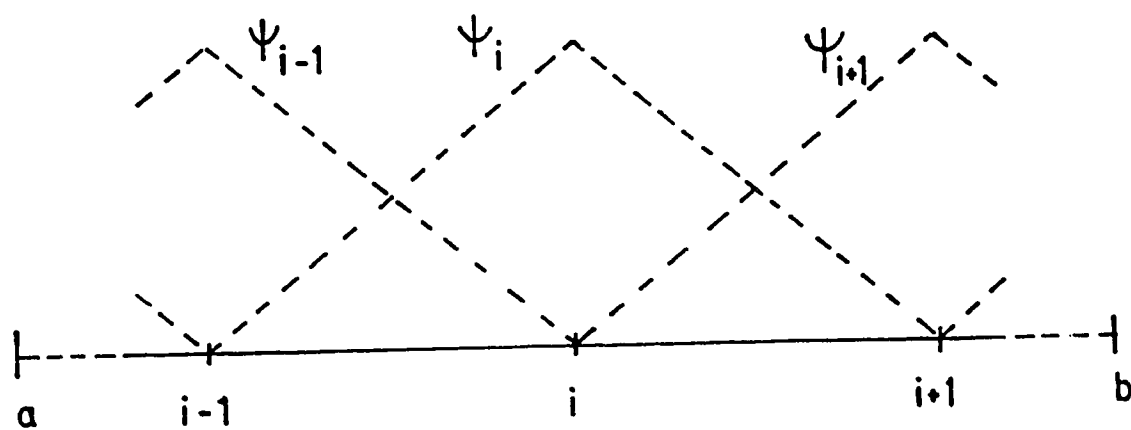


Fig. 6.1 Piecewise linear function of ψ .

matrices symmetrical. Substituting (6.9) into the left hand side of (6.10) gives the matrix expression for $i = 1, \dots, I-1$,

$$AE(i)\bar{c}_{i-1} + AC(i)\bar{c}_i + AW(i)\bar{c}_{i+1},$$

where $AE(i)$, $AC(i)$, $AW(i)$ denote 6×6 matrices whose components come from integrating the components of $H_0(\bar{\psi})$ over each cell B_i . The same procedure applied to the right hand side of (6.10) merely gives $E\bar{c}_i$. For computational convenience, the calculations are actually carried out by integrating over each subinterval rather than over each cell, so that the matrices AE , AC , AW are constructed in two steps; that is by first integrating over $[x_{i-1/2}, x_i]$ and later over $[x_i, x_{i+1/2}]$. As these matrices are constructed, they are immediately assembled into a global matrix A by means of modulo 6 arithmetic calculations. Specifically, we define the new vector \bar{x} by $x(6i+j) = c_i^j$ for $i = 0, \dots, I$ and $j = 0, \dots, 5$, where c_i^j denotes the j^{th} component of \bar{c}_i . The entries of $AE(i)$, $AW(i)$, $AC(i)$ are mapped accordingly so that (6.10) is discretized into a Hermitian complex matrix eigenvalue problem:

$$A\bar{x} = \lambda\bar{x} \quad , \quad (6.11)$$

We note that the global matrix A is sparse and only the nonzero entries are stored. It is an elementary procedure to improve the accuracy of the approximation by increasing the number of grid points (and thus the order of A). The bottom of the spectrum of (6.11) is computed by means of IMSL routines and the special form of (6.11) is of great importance in reducing computational effort.

The process of calculation begins by guessing an initial $V_0(z)$ and iteratively solving (6.1) and (6.2) with $k_x = k_y = 0$. Then the new $V(z)$ is used to start an iterative solution of (6.1) and (6.2) for several values of k_x with $k_y = 0$ to estimate the effect of different shapes of ψ_ν ($\nu = 1, 2$) at different k 's on the solution of (6.2). The contour in k_x - k_y space is assumed to be square and (6.4) is used to find $k_{x\max}$ at which $E_\nu(k_{x\max}, 0) = E_{Fp}$. An improved $V(z)$ is thus obtained.

Next, more detailed calculations involving k_x and k_y are done. Radial coordinates are used in the k_x - k_y plane with Δk^2 and $\Delta\theta$ constant. At each θ the value of k^2 is determined which gives $E_1 = E_{Fp}$ in the solution of (6.1) by using a bisection method where the ends of the bracketing interval are always on grid points. When the interval is one grid unit, linear interpolation is used. In this way, calculations are restricted only to the regions of interest and values are saved for future use. When the E_{Fp} contours for E_1 and E_2 have been determined, the hole concentration from (6.4) is compared with the desired value and used to predict the next guess of the Fermi energy and the corresponding k_x value. This whole procedure is repeated until the Fermi energy converges. It is to be noted that due to the symmetry of the Fermi contours, computations are only needed for $0 \leq \theta \leq \pi/2$.

To hasten the convergence process, the next guess is obtained by an approximate secant method. The change of area with k_x , $\Delta A / \Delta k_x$, is estimated by calculating the area inside the boundaries of the two rectangles closest to the previous Fermi contours. The change in k_x can then be found knowing the desired change in A . The next E_{Fp} is the value of E_1 from (6.1) at a new k_x , and $k_y = 0$.

The Fermi energy is then compared with the energy of the second subband (E_3 and E_4) at $k_x = k_y = 0$ to determine whether this subband will be occupied. If so, the whole process is repeated but now there are two pairs of contours to find. Now the sum of the enclosed areas must agree with (6.4).

The method described above reduces considerably the computational intensity of the problem - indeed it may make the difference as to whether a given simulation is actually feasible.

6.3 Density-of-States Masses

Once the calculations have converged, the density-of-states masses of holes can be obtained. The density-of-states masses of holes for each subband (experimentally shown to be approximately equal to the classical cyclotron masses [77]) can be defined as [78]

$$m_{\nu}^* = \frac{\hbar^2}{2\pi} \frac{dA_{\nu}}{dE} \bigg|_{E_{Fp}} \quad (6.12)$$

where, A_{ν} denotes the area inside the ν^{th} Fermi Contour. In doping superlattices with symmetric electric potentials and no magnetic field, the doubly degenerated subbands do not split at higher values of k_x , k_y . Then in the first subband, $A_1 = A_2$ and $m_1^* = m_2^*$. Similarly, $A_3 = A_4$ and $m_3^* = m_4^*$ belong to the second subband of the system. Whether this second subband is the first of the light hole subbands or the second of the heavy hole subbands can be resolved by identifying the shape of the envelope functions ψ_3 and ψ_4 . This identification procedure can be also applied to the next few populated higher

subbands.

6.4 Results and Discussions

Figures 6.2 and 6.3 compare our computed results with the experimentally determined cyclotron masses for a Si p-channel inversion layer with different surface carrier concentrations at the (110) and (100) surfaces, respectively. Due to band splitting, there are two different masses for the heavy and the light holes as shown in Figure 6.2. Observe that for the (110) surface, our results are in good agreement with the experimental results obtained in Reference 77 if one only considers the smaller values of the heavy holes. A similar result was obtained in Reference 92. In the (100) surface, Figure 6.3, the mean value of the heavy hole masses is in reasonable agreement with the experimental data. Our calculations show that for the (110) and (100) surfaces, the population of the second subband occurs at hole concentrations of approximately $2.9 \times 10^{12} \text{ cm}^{-2}$ and $2.1 \times 10^{12} \text{ cm}^{-2}$, respectively. Figure 6.4 shows the calculated self-consistent potential. Also shown are the rms envelope functions and energy levels of the three highest subbands calculated at $k_x = k_y = 0.0$ for the hole concentration of $8.6 \times 10^{12} \text{ cm}^{-2}$. Figure 6.5 shows the Fermi contours at the hole concentration of $5 \times 10^{12} \text{ cm}^{-2}$ for (100) surface. These results are consistent with those calculated results given in References 77, 91 and 92.

The above computations and those to follow were carried out using twenty-one grid points in the z-dimension for both the space-charge model and the self-consistent calculations. The accuracy of our calculations was determined not only by comparison with experiments for

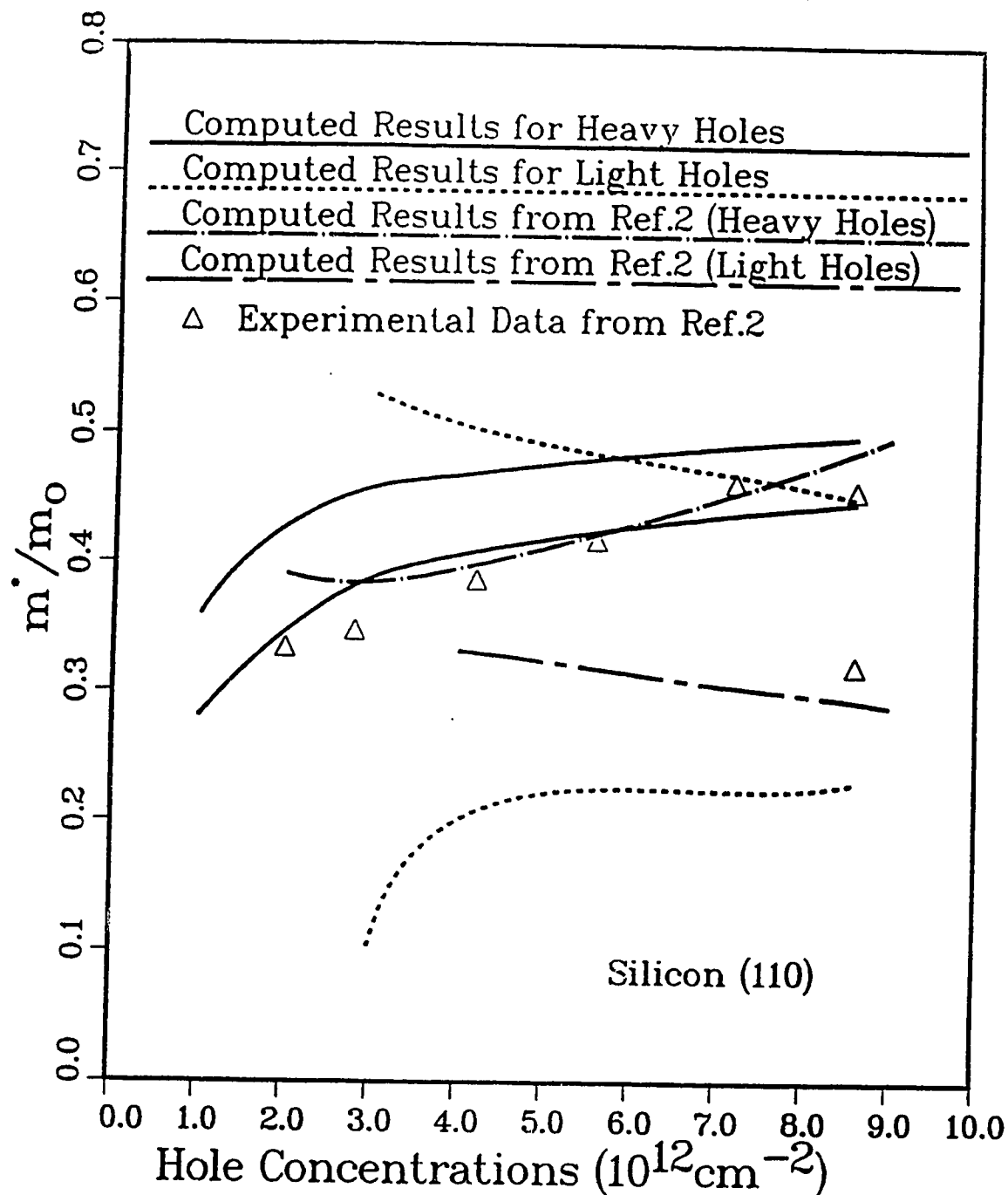


Fig. 6.2 Density-of-states masses at different hole concentrations for a (110) Si MOS structure. $N_D - N_A = 1 \times 10^{15} \text{cm}^{-3}$. The two solid lines represent the 2 different masses for the heavy hole bands. Likewise, the two dotted lines represent the 2 different masses for the light hole bands. The line and dot (dash) curve represents the average of the 2 different masses for the heavy (light) bands.

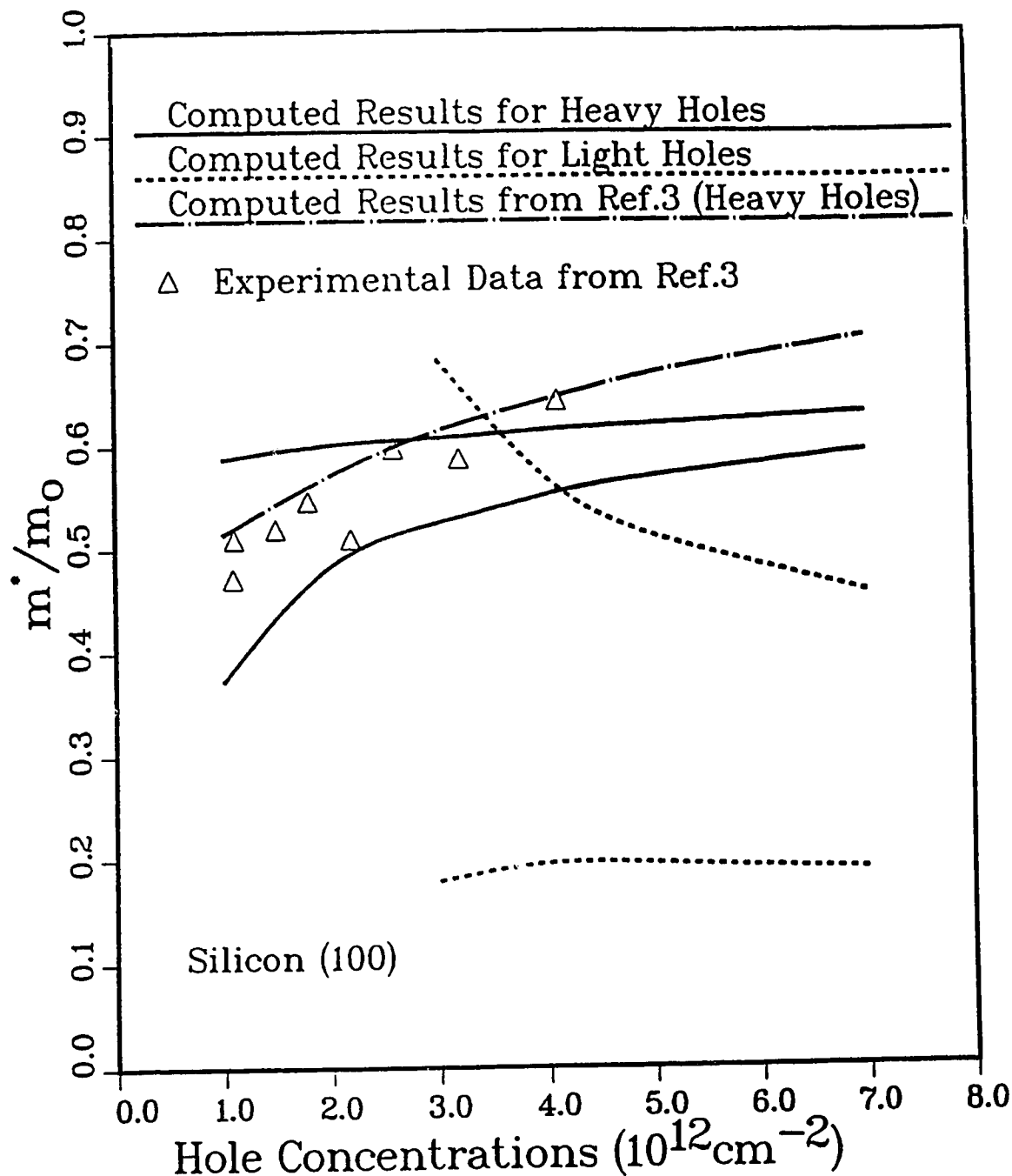


Fig. 6.3 Density-of-states masses at different hole concentrations for a (100) Si MOS structure. $N_D - N_A = 1 \times 10^{15} \text{cm}^{-3}$. The two solid lines represent the 2 different masses for the heavy hole bands. Likewise, the two dotted lines represent the 2 different masses for the light hole bands. The line and dot curve represents the average of the 2 different masses for the heavy bands.

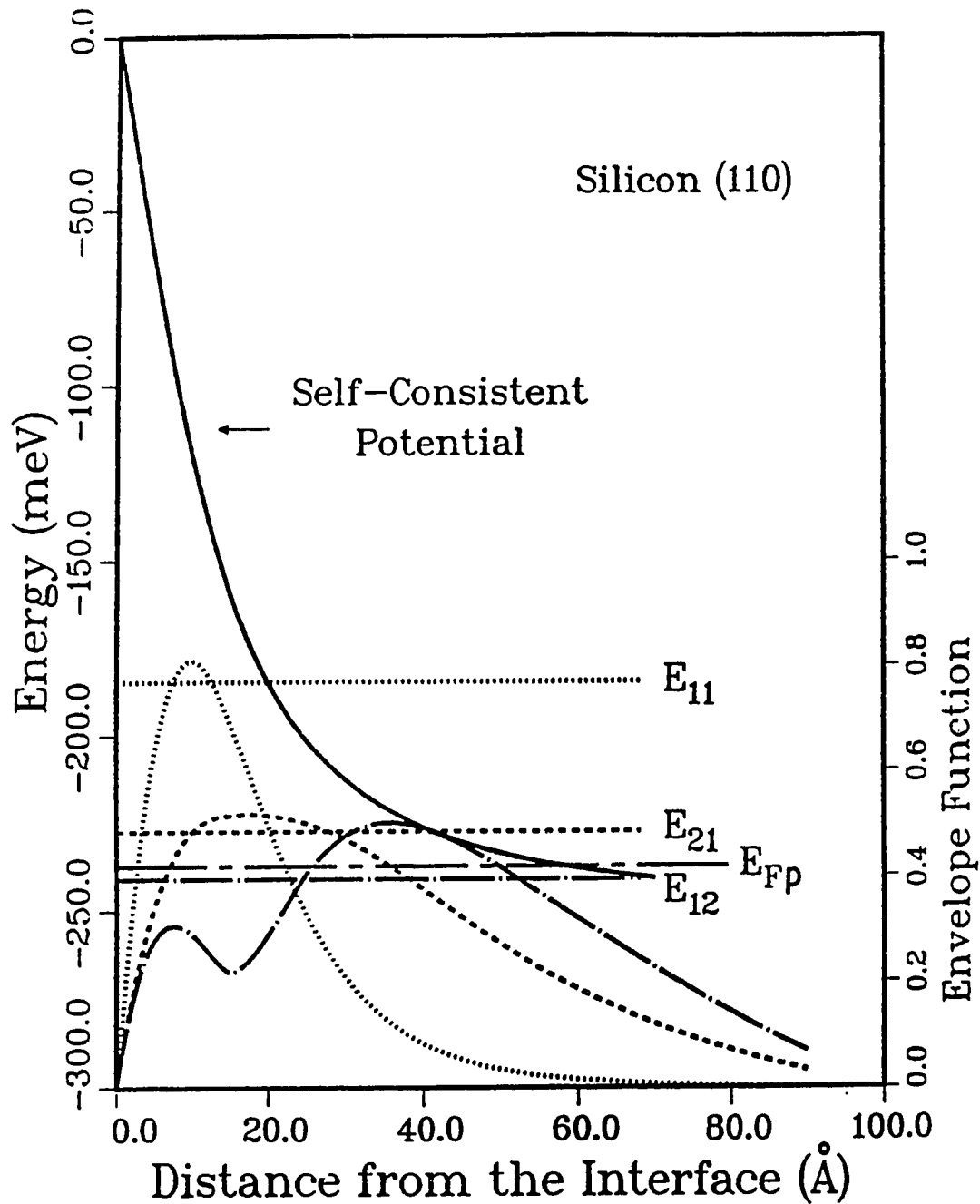


Fig. 6.4 Self-consistent electric potential with the three highest subbands energies and rms envelope functions at $k_x = k_y = 0.0$.

The hole concentration is $8.6 \times 10^{12} \text{ cm}^{-2}$ in a (110) Si MOS structure. E_{11} and E_{12} are the energies of the first and second subbands of the heavy holes, and E_{21} is the energy of the first subband of the light holes. E_{Fp} is the Fermi energy. $N_D - N_A = 1 \times 10^{15} \text{ cm}^{-3}$.

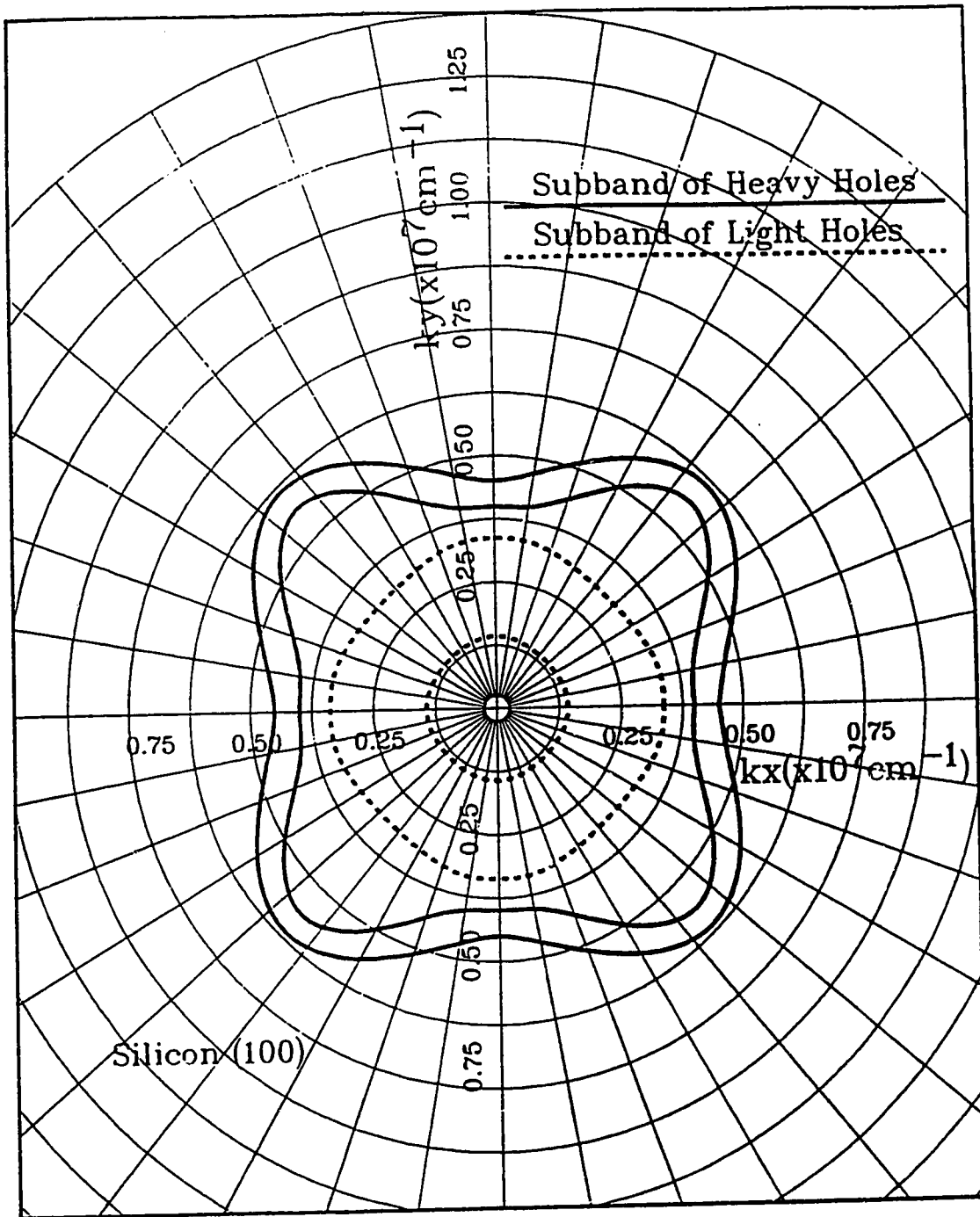


Fig. 6.5 Fermi contours of the highest subband for the heavy and the light holes. The hole concentration is $5 \times 10^{12} \text{ cm}^{-2}$ in a (100) Si MOS structure. The two solid lines represent the Fermi contours for the two heavy hole bands. Likewise, the two dotted lines represent Fermi contours for the two light hole bands.

the MOS, as illustrated above, but also by considering further grid refinement. For example, for the ranges of hole concentrations considered here, the density-of-states masses, subband energies, and electric potential calculated by twenty-one grid points yielded no more than 3%, 1% and 0.05% difference in results, respectively, when compared with the results calculated by thirty-one grid points.

The subband energies, Fermi contours and the density-of-states masses of a doping superlattice were calculated for surface orientation of (100) and (110), and using Si and Ge as the host material. The calculations also involved the use of different values of the physical parameters of the doping superlattice, such as the thickness of the p-type layers and doping levels of the p and the n-type layers.

Figure 6.6 shows the electric potentials and the respective envelope functions at $k_x = k_y = 0.0$ and at different hole concentrations for a Si doping superlattice with $N_A = 8 \times 10^{19} \text{ cm}^{-3}$, $N_D = 1 \times 10^{19} \text{ cm}^{-3}$ and $d_p = 4 \text{ nm}$. This high level of doping of the n-type layers will result in the merging of the impurity band with the valence band and at $T = 0^\circ \text{K}$, no freezing out of the acceptors may occur. We observe that compared to the MOS inversion layer, the electric potential flattens and the envelope functions broaden with increased hole concentrations. Figures 6.7 and 6.8 show the changes in the subband energies with hole concentrations for a Si doping superlattice using the same parameters as above. As in a MOS inversion layer, a different surface orientation greatly affects the characteristics of the subband energies. For example, the third subband energy for the (110) surface (see Figure 6.7) can be determined from its envelope function to be the second subband of the heavy holes. In the case of

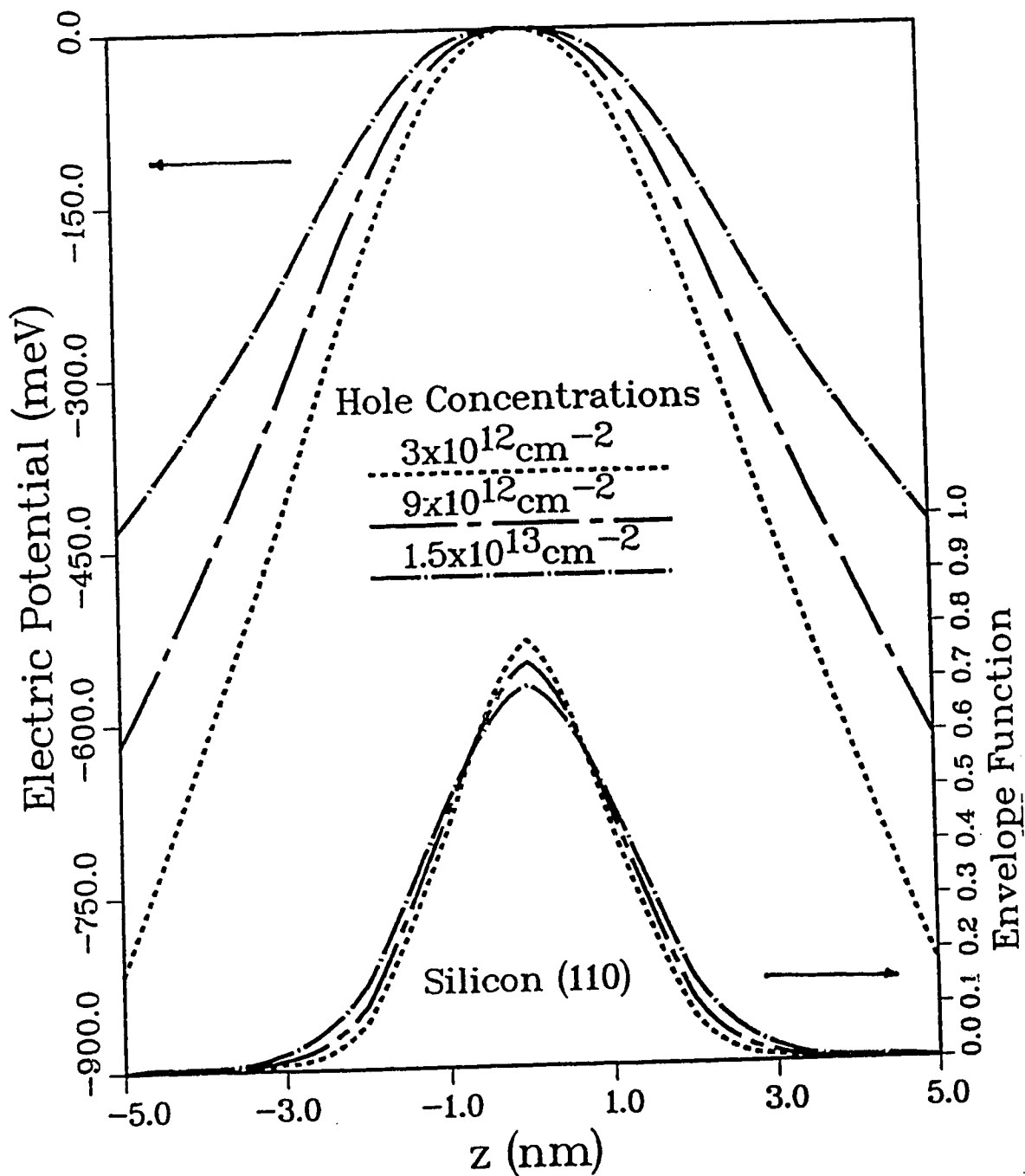


Fig. 6.6 The electric potentials and envelope functions (at $k_x = k_y = 0.0$) of the highest subband for various values of hole concentration. The values of the parameters of the Si doping superlattice are: $N_A = 8 \times 10^{19} \text{ cm}^{-3}$, $N_D = 1 \times 10^{19} \text{ cm}^{-3}$ and $d_p = 4 \text{ nm}$.

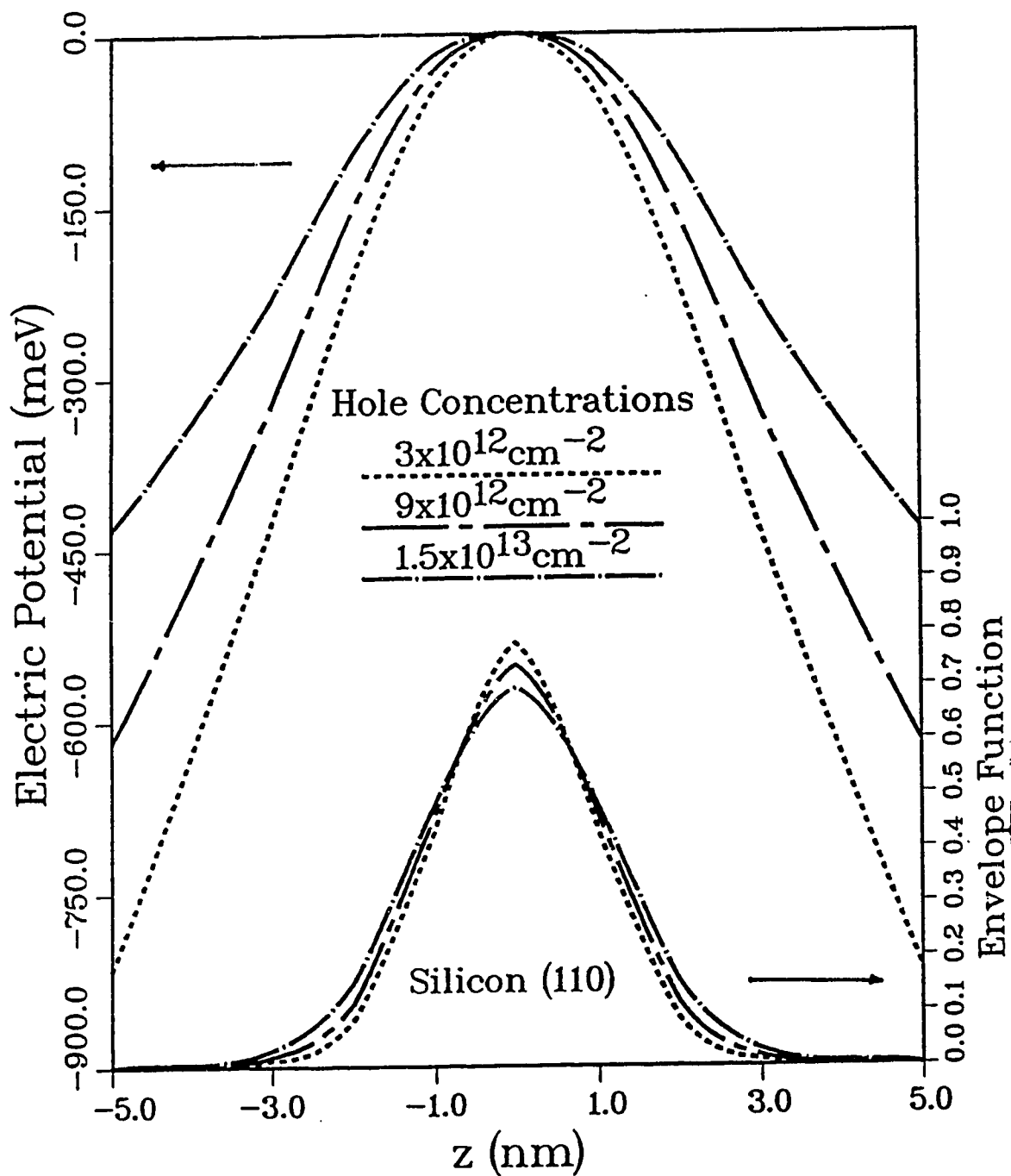


Fig. 6.6 The electric potentials and envelope functions (at $k_x = k_y = 0.0$) of the highest subband for various values of hole concentration. The values of the parameters of the Si doping superlattice are: $N_A = 8 \times 10^{19} \text{ cm}^{-3}$, $N_D = 1 \times 10^{19} \text{ cm}^{-3}$ and $d_p = 4 \text{ nm}$.

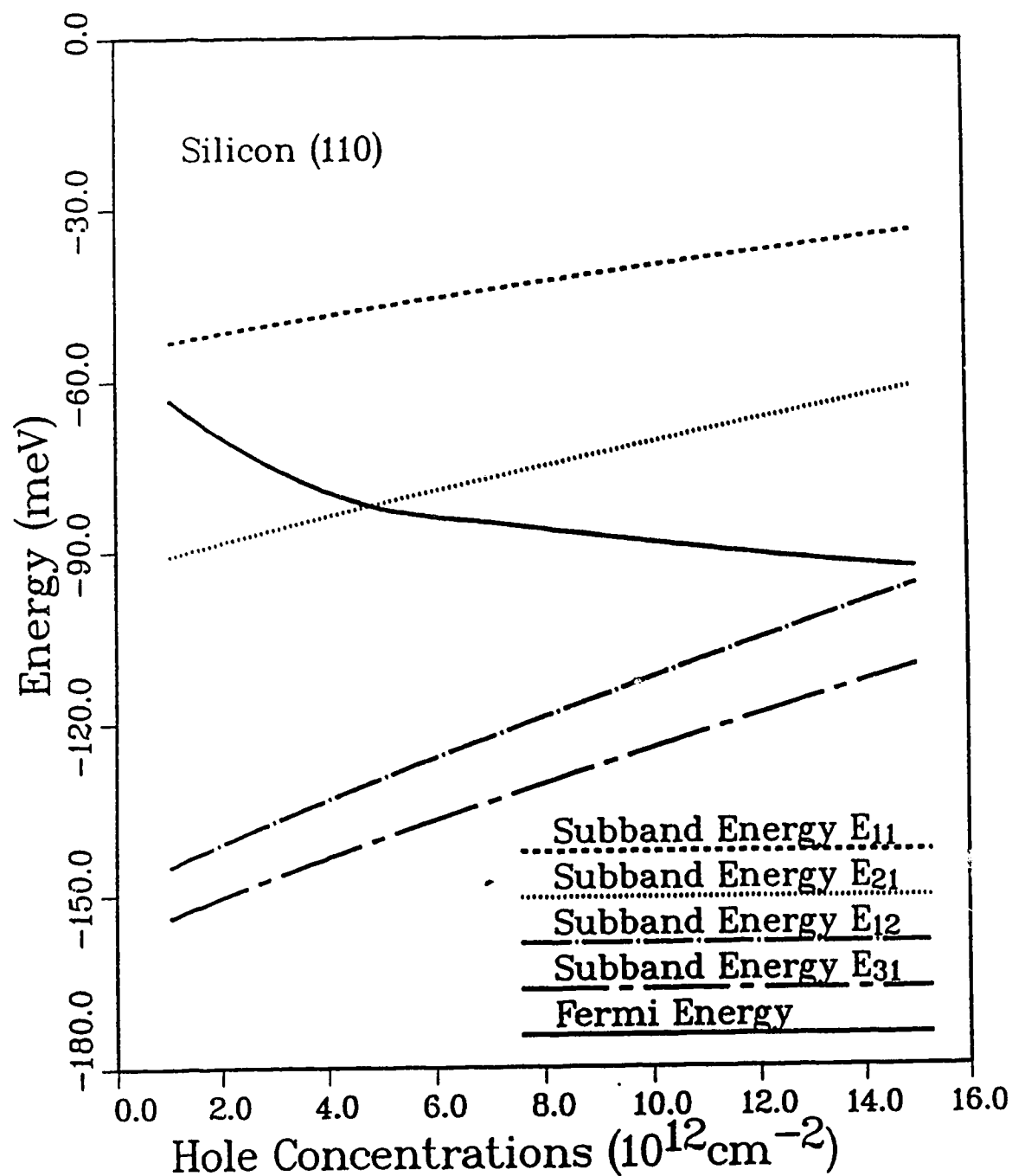


Fig. 6.7 Subband energies as a function of hole concentration. The (110) Si doping superlattice's parameters are given in Figure 6.6 caption. E_{11} and E_{12} are the energies of the first and second subbands of the heavy holes and E_{21} and E_{31} are the energies of the first subband of the light and split-off holes.

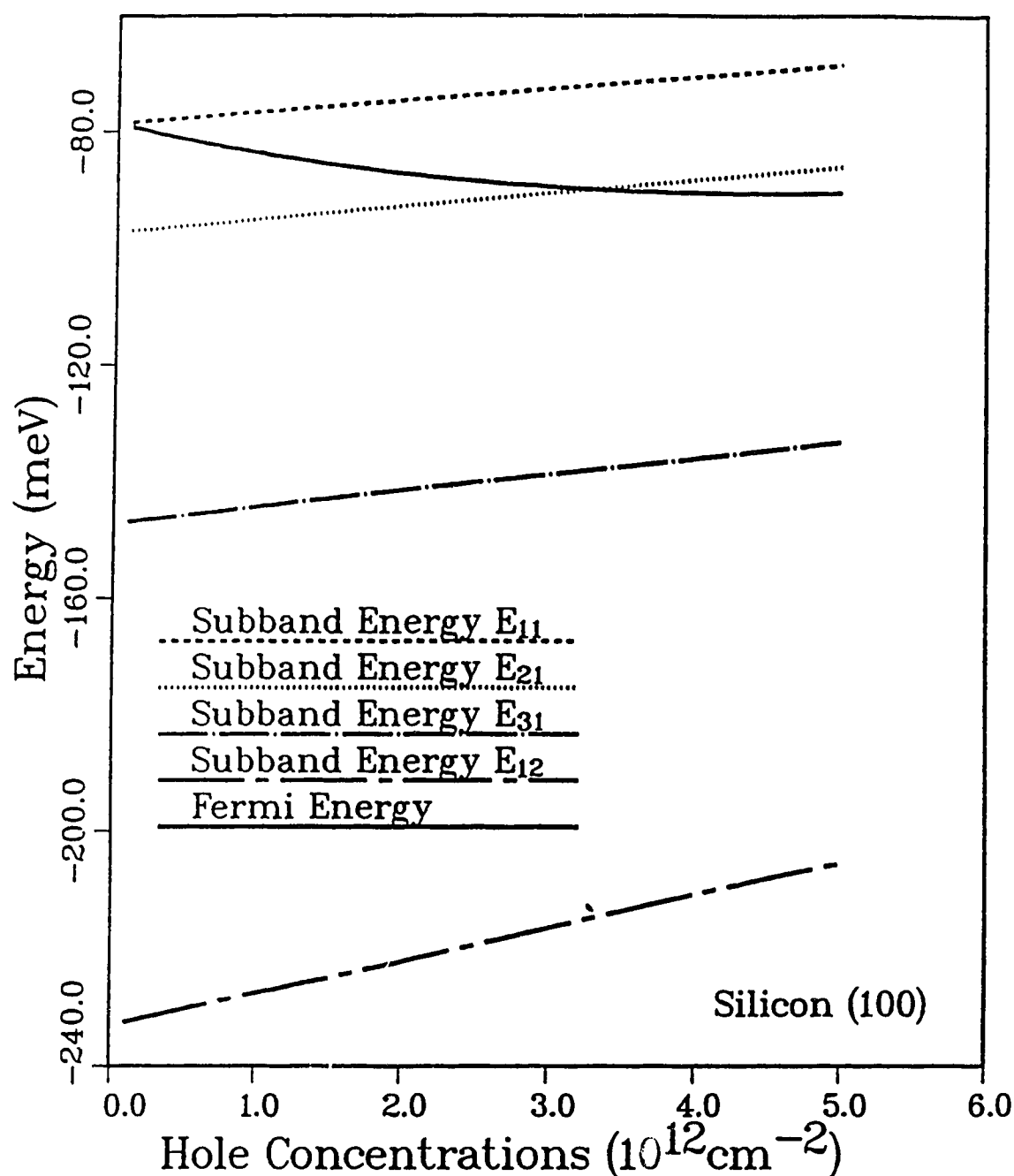


Fig. 6.8 Subband energies as a function of hole concentration. The (100) Si doping superlattice's parameters are given in Figure 6.6 caption. E_{11} and E_{12} are the energies of the first and second subbands of the heavy holes and E_{21} and E_{31} are the energies of the first subband of the light and split-off holes.

the (100) surface, the third subband is the highest subband of the split-off holes. The population of the second subband energy of the holes for the (110) surface occurred at a hole concentration of $4.8 \times 10^{12} \text{ cm}^{-2}$ and at $3.2 \times 10^{12} \text{ cm}^{-2}$ for the (100) surface. The values of the hole concentration at which the second subband energy is populated is usually higher for the (110) surface than for the (100) surface, a property which is similar to the MOS inversion layer. Unlike the MOS inversion layer, these values of the hole concentration vary with different values of the parameters of the doping superlattice. The subband energies tend to converge with increased hole concentrations; whereas they tend to diverge in the case of the inversion layer. Note that in the figures, E_{11} and E_{12} represent the energies of the first and second subbands of the heavy holes and E_{21} and E_{31} represent the energies of the first subband of the light and split-off holes, respectively. Figures 6.9 and 6.10 show the subband energies varying as a function of k values for surface orientations of (110) and (100) at a hole concentration of $3 \times 10^{12} \text{ cm}^{-2}$. In contrast to the MOS inversion layer, and as mentioned in the preceding section, the doubly degenerated subbands do not split with increased values of k_x or k_y . Similar to the MOS inversion layer, the subband energies for the (110) surface are highly non-parabolic. The extent to which these subbands are separated at $k_x = k_y = 0.0$ will depend on the values of the hole concentration (see Figures 6.7 and 6.8) as well as the values of the physical parameters of the doping superlattice.

Figure 6.11 illustrates the density-of-states masses of holes for the two surface orientations. For the range of hole concentrations considered, only the first of the heavy and light hole subbands are

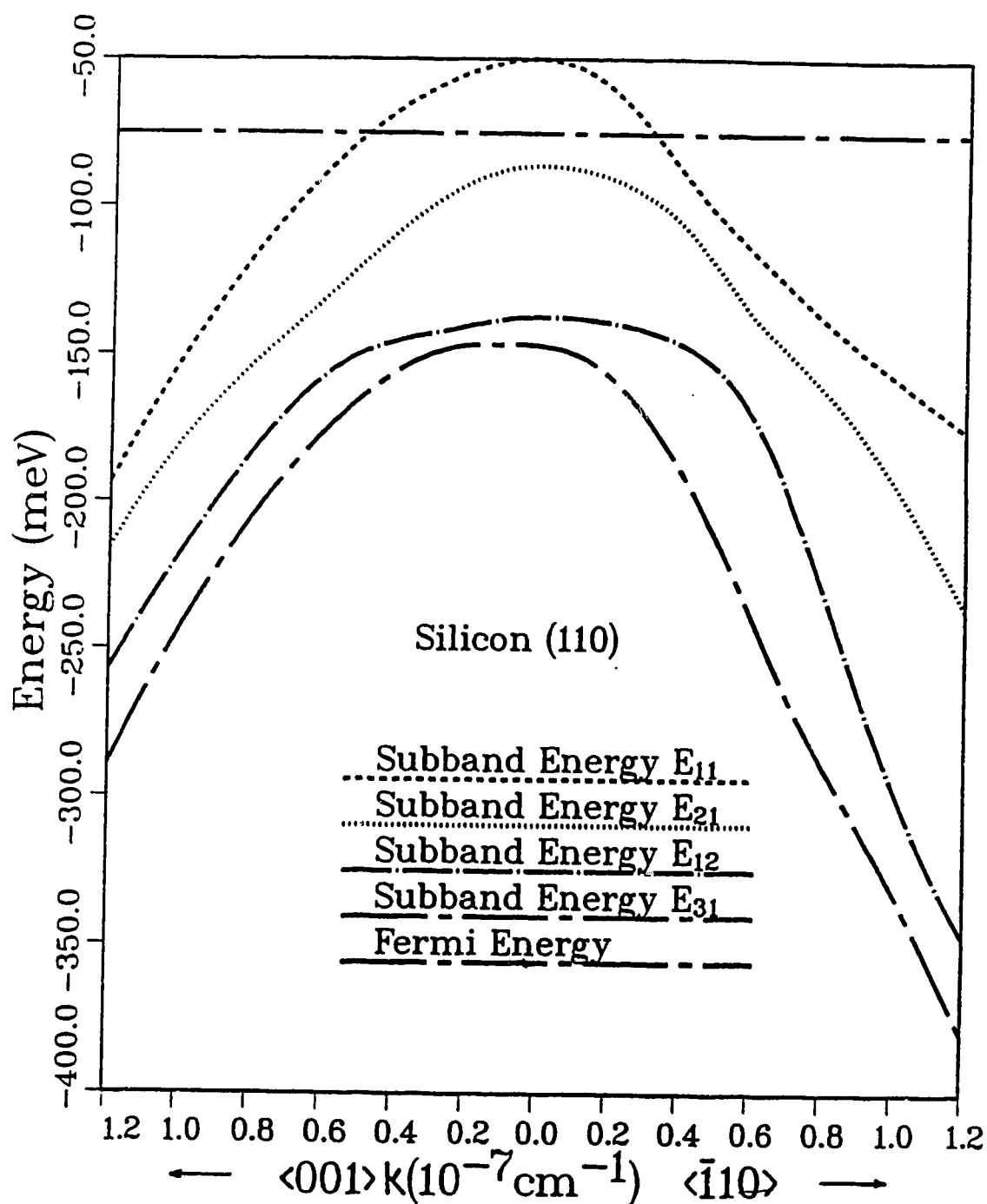


Fig. 6.9 The hole subband dispersions for a (110) Si doping superlattice with the parameter given in Figure 6.6 caption. The hole concentration is $3 \times 10^{12} \text{ cm}^{-2}$.

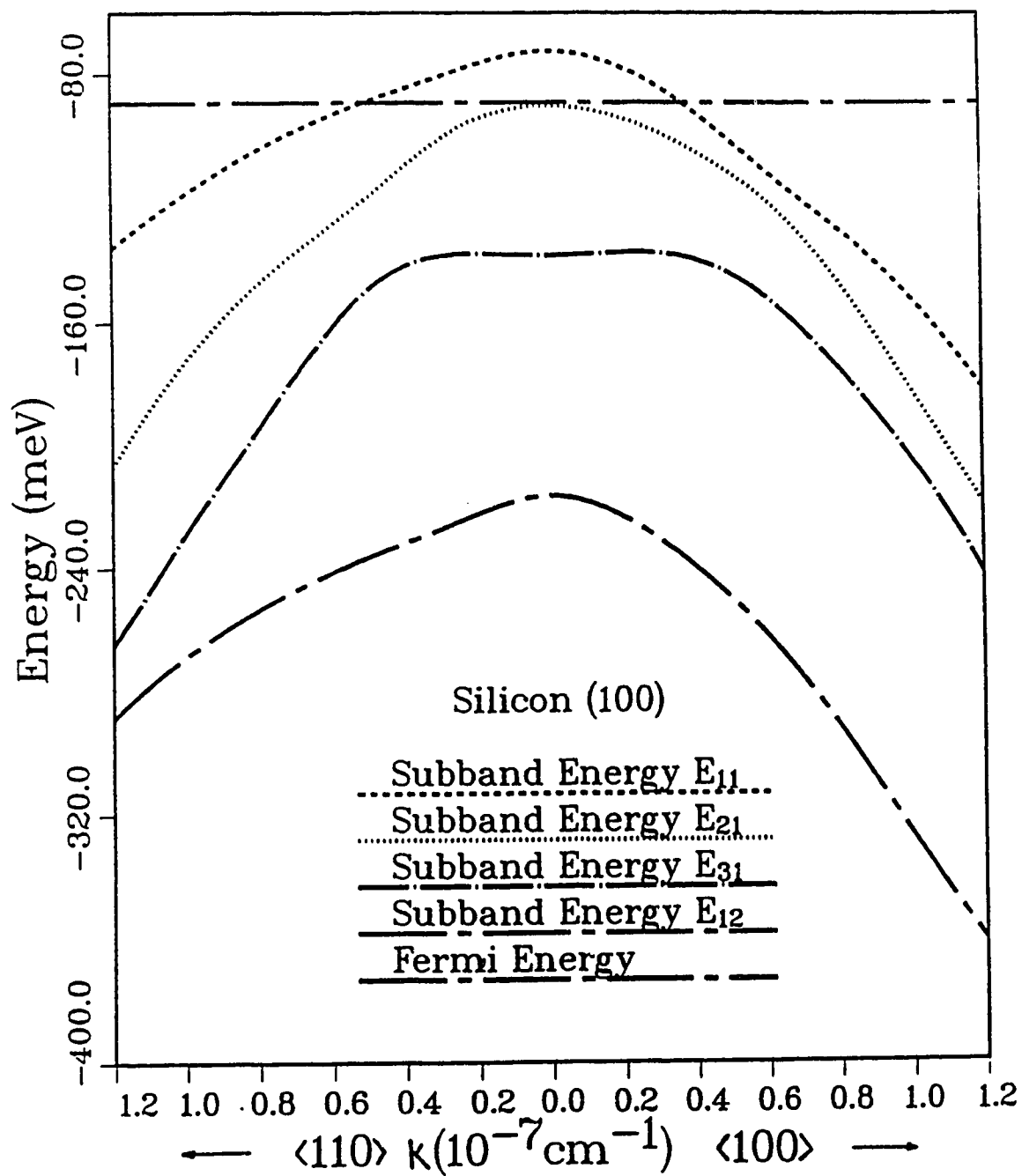


Fig. 6.10 The hole subband dispersions for a (100) Si doping superlattice with the parameter given in Figure 6.6 caption. The hole concentration is $3 \times 10^{12} \text{ cm}^{-2}$.

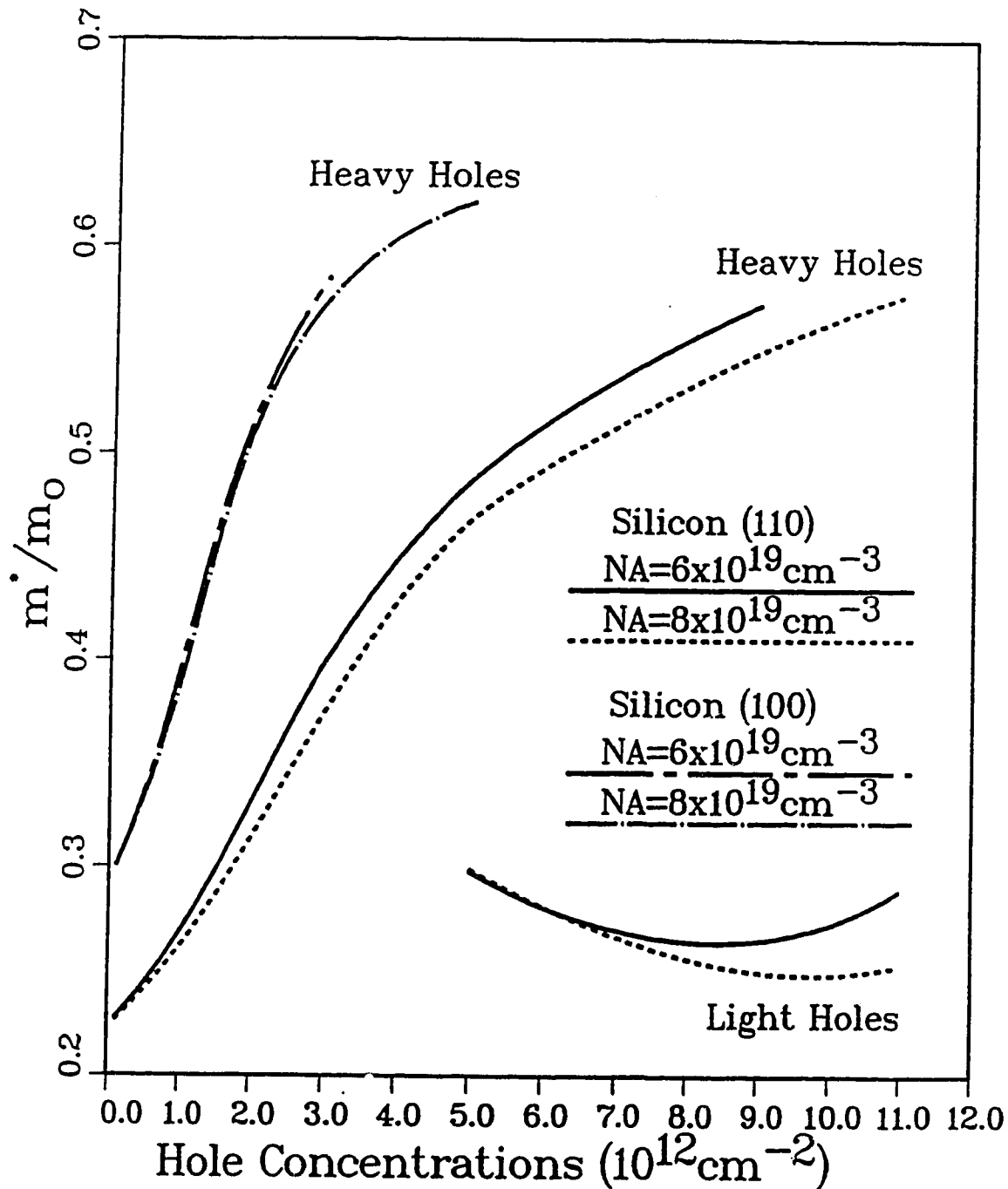


Fig. 6.11 The density-of-states masses of hole as a function of hole concentration for (110) and (100) Si doping superlattices with $N_D = 1 \times 10^{19} \text{ cm}^{-3}$, $d_p = 4 \text{ nm}$ and N_A 's are given in the Figure. The heavy and light holes indicated in the Figure belong to the first of the heavy and the light hole subbands, respectively.

populated. Hence, the masses shown in Figure 6.11 and other figures are basically masses of the first subband of the heavy and/or light hole subbands. Observe that the masses of the holes for the (100) surface are more sensitive functions of the hole concentration than for the (110) surface. However, as shown in Figures 6.12 and 6.13, the hole masses for the (100) surface are less sensitive to changes in the thickness and doping level of the p-type layers. For any given hole concentration (in the range given in Figure 6.11), the hole mass is smaller for the (110) surface than that for the (100) surface. Notice from Figure 6.12 that beyond certain values of the thickness of the p-type layers, and depending on the value of N_A , the hole masses become fairly constant. These values will depend on the doping level of the p-type layers. Figure 6.12 and 6.13 also show that the sensitivity of the hole masses to the values of the thickness and doping level is greater for higher hole concentrations. It is to be noted that only the heavy holes are usually considered as they are normally the dominant carriers as experimentally observed in the MOS inversion layers [77].

The calculations were repeated for Ge doping superlattices. Figure 6.14 shows the subband energies as functions of hole concentration calculated both by the self-consistent approach and the space charge model for a superlattice with $N_A = 8 \times 10^{18} \text{ cm}^{-3}$, $N_D = 1 \times 10^{17} \text{ cm}^{-3}$ and $d_p = 6 \text{ nm}$. Because of the smaller value of the hole masses in bulk Ge, the required doping level to avoid freezing out of the acceptors is lower than in Si. The space-charge model is used here, not because the acceptors are frozen out, but rather to compare the results with the self-consistent method. At very low hole concentration levels, the

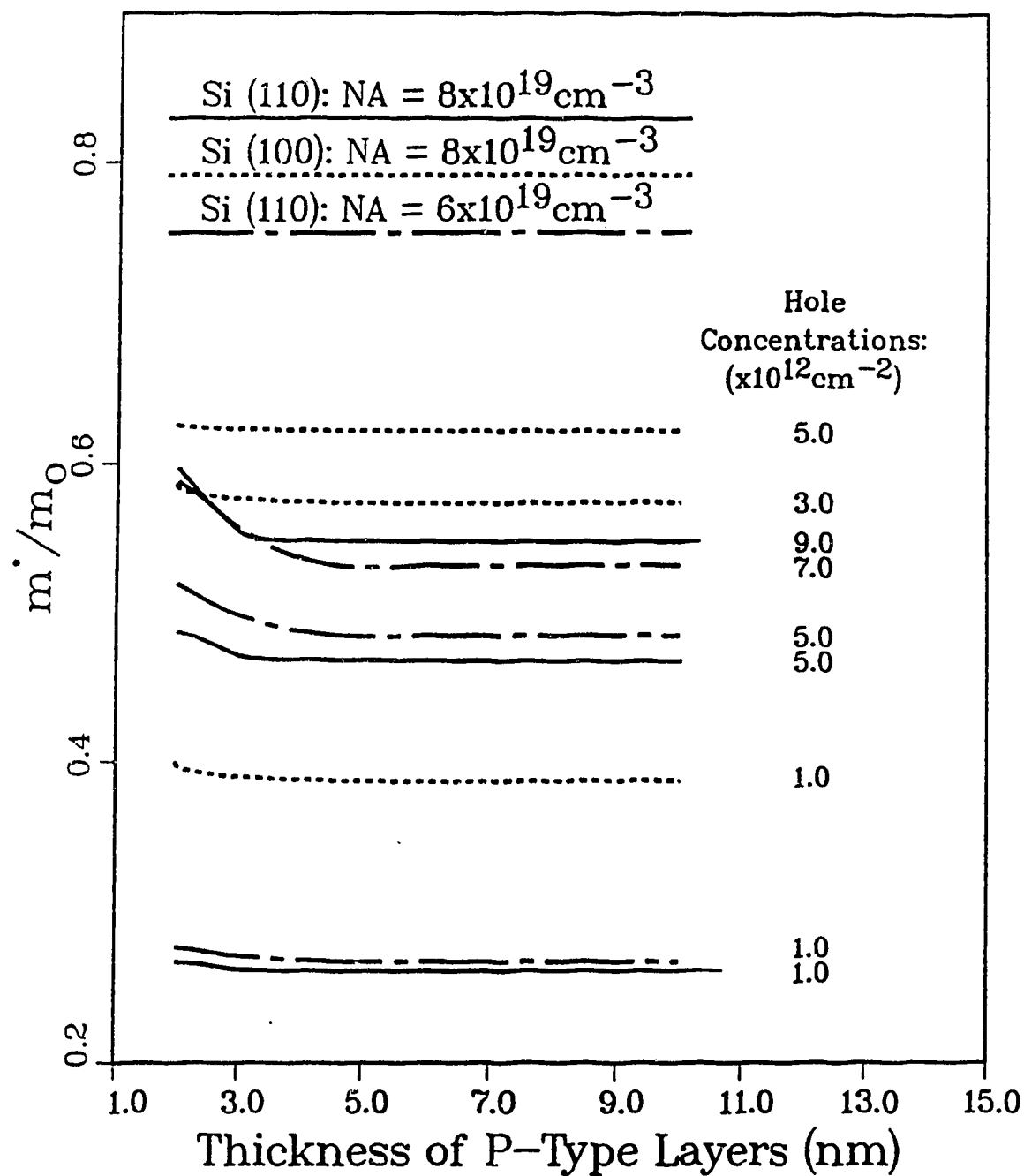


Fig. 6.12 The density-of-states masses of heavy holes of the first subband as a function of the thickness of p-type layers and hole concentration for (110) and (100) Si doping superlattices with $N_D = 1 \times 10^{19} \text{ cm}^{-3}$ and N_A 's are given in the Figure.

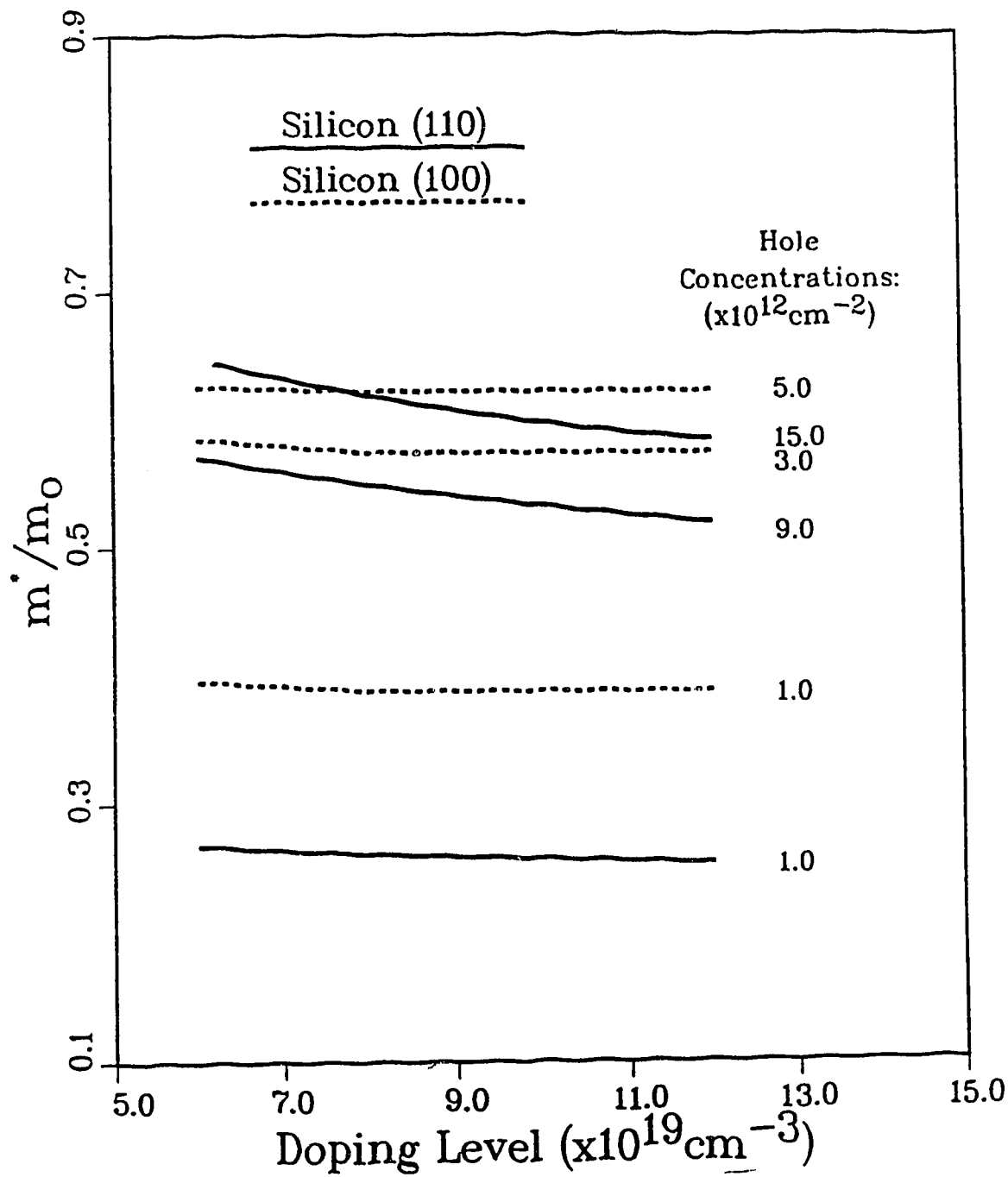


Fig. 6.13 The density-of-states masses of heavy holes of the first subband as a function of the doping level of the p-type layers (N_A) and hole concentration for (110) and (100) Si doping superlattices with $N_D = 1 \times 10^{19} \text{ cm}^{-3}$ and $d_p = 4 \text{ nm}$.

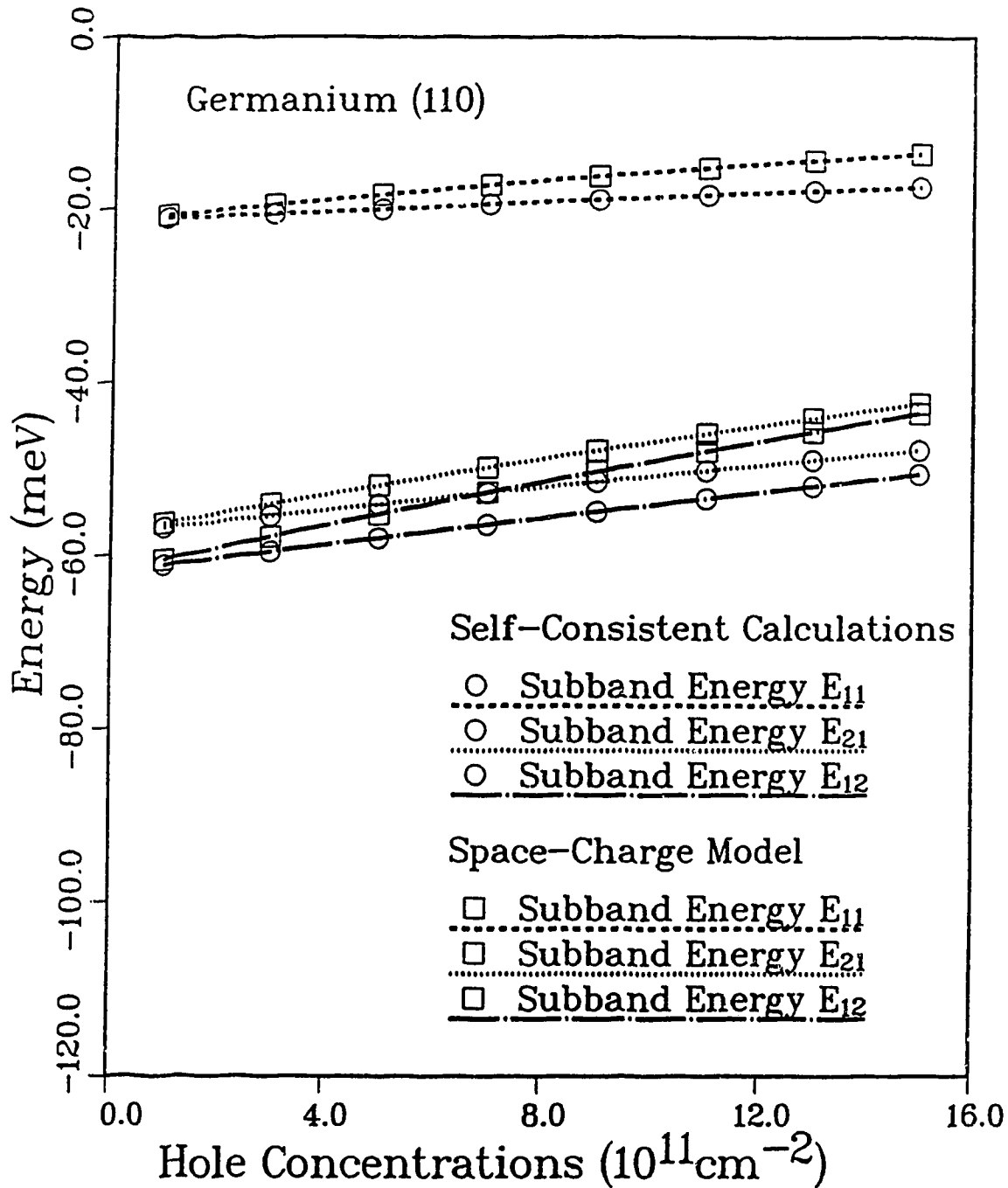


Fig. 6.14 Subband energies as a function of hole concentration calculated self-consistently and by the space-charge model for a (110) Ge doping superlattice with $N_A = 8 \times 10^{18} \text{cm}^{-3}$, $N_D = 1 \times 10^{17} \text{cm}^{-3}$ and $d_p = 6 \text{ nm}$. E_{11} and E_{12} are the energies of the first and second subbands of the heavy holes and E_{21} is the energy of the first subband of the light holes.

space charge model may give a good approximation to the self-consistent calculations. This is not surprising given the fact that the self-consistent potential is corrected by the Hartree potential whose magnitude will depend on the value of the hole concentration. Hence, the smaller the value of the hole concentration, the smaller the Hartree correction to the electric potential. As a result, the electric potential given by the self-consistent calculation and by the space-charge model becomes less significantly different. As for the density-of-states masses, they are again calculated by the self-consistent method. Unlike the Si doping superlattice, the Ge hole masses of the first subband for the (100) and (110) surfaces converge to almost a common value as the hole concentration decreases (see Figure 6.15). Aside from this, the properties of Ge doping superlattice holes are similar to those of Si doping superlattices.

Figures 6.16 and 6.17 show that the hole masses of the first subband are more sensitive functions of the layer thickness and doping level for both the (100) and (110) surfaces than in Si. (see Figure 6.12 and 6.13). This can be attributed to the fact that smaller doping levels of the p-type layers are used for the Ge doping superlattice. For both the Si and Ge doping superlattices considered in Figures 6.11 and 6.15, the doping levels of the n-type bulk do not seem to have any noticeable effect on the hole masses. However, as the thickness of the p-type layers narrows, this effect becomes more prominent. This is illustrated in Table 6.2. Notice that for $d_p = 6$ nm, the hole masses hardly change even with a three orders of change in magnitude in the n-type bulk doping level. As N_A increases at constant d_p and hole concentration (as a percentage of $N_A d_p$), it was determined that the

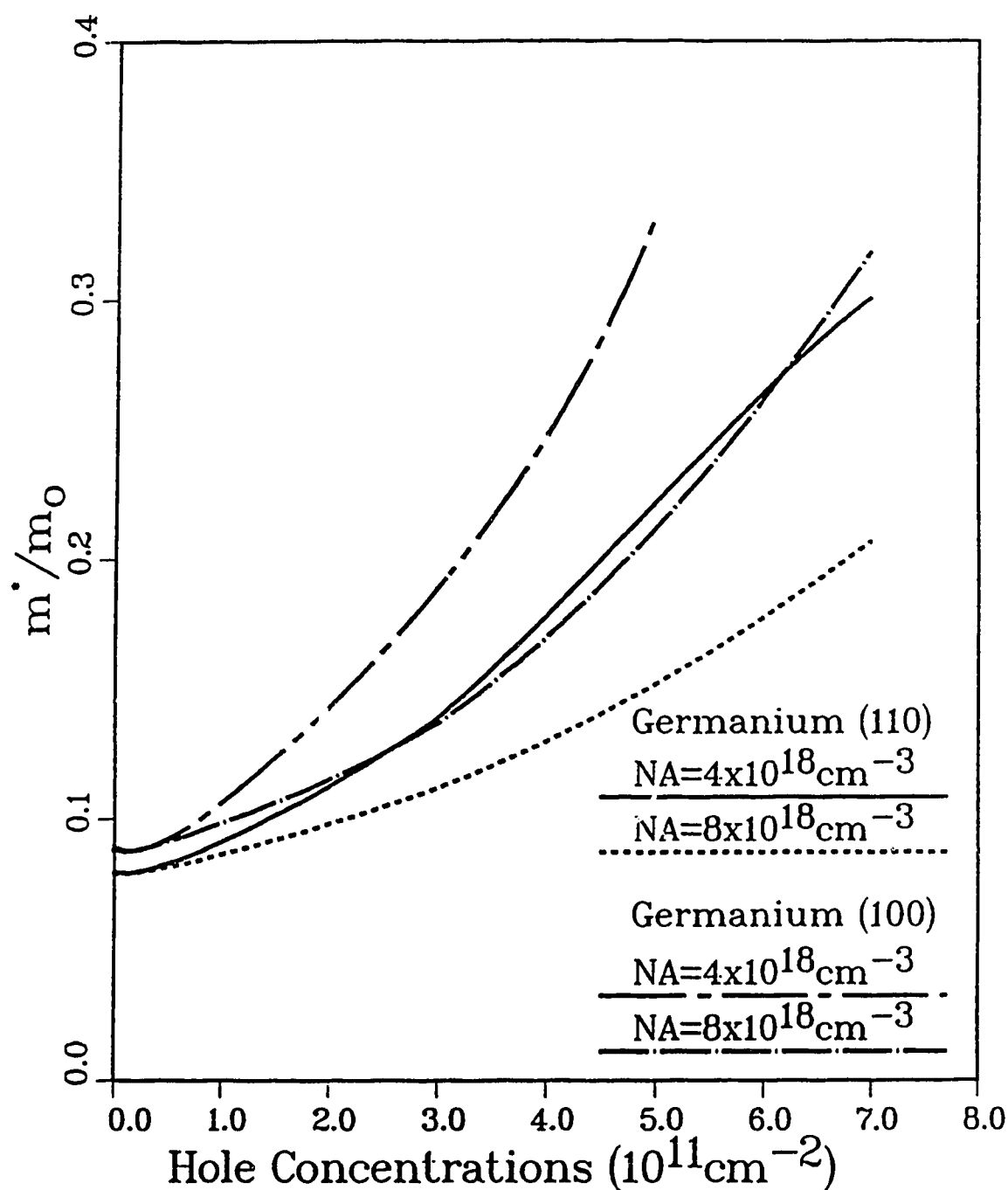


Fig. 6.15 The density-of-states masses of heavy holes of the first subband as a function of hole concentration for (110) and (100) Ge doping superlattices with $N_D = 1 \times 10^{17} \text{ cm}^{-3}$, $d_p = 6 \text{ nm}$ and N_A 's are given in the Figure.

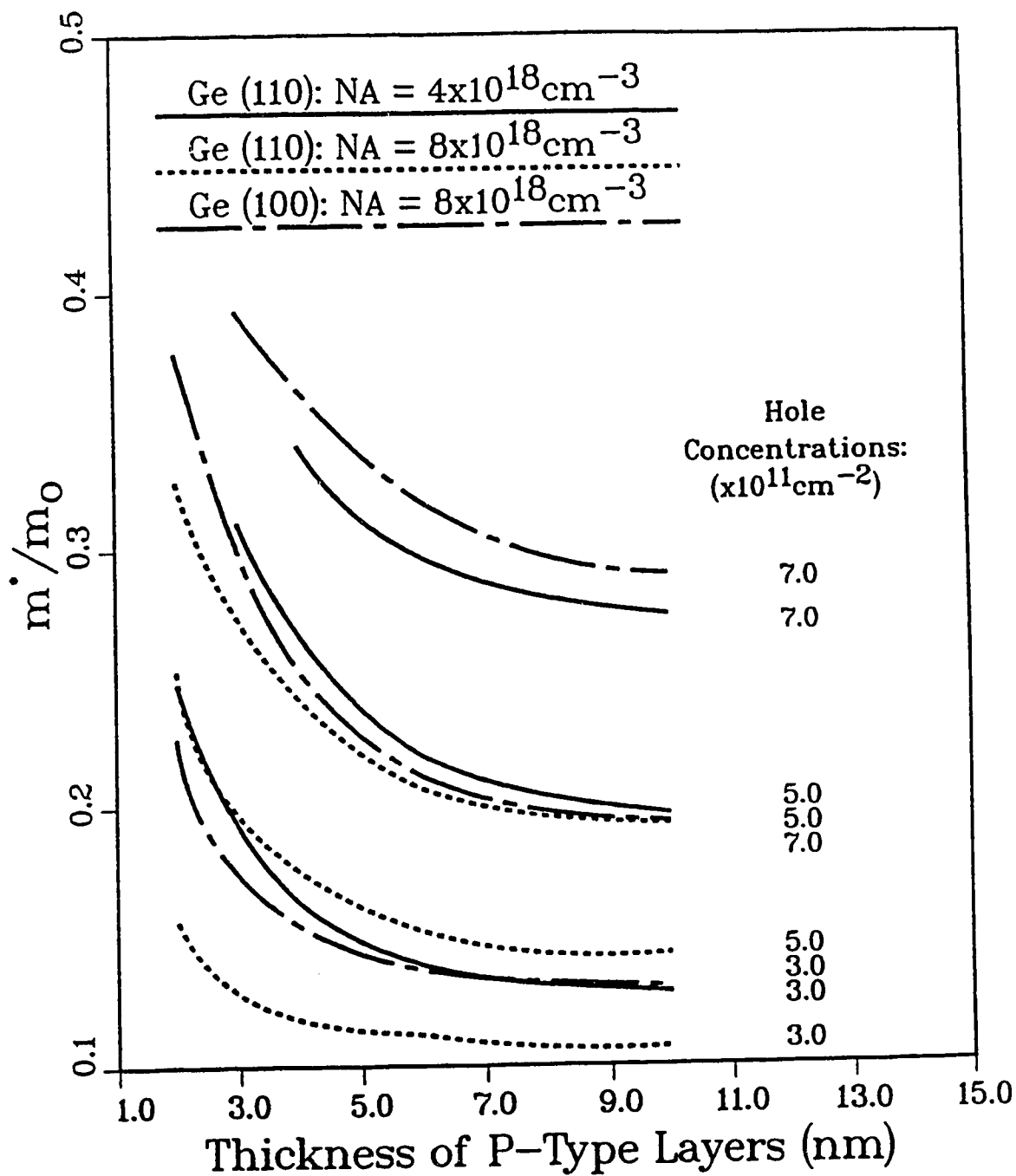


Fig. 6.16 The density-of-states masses of heavy holes of the first subband as a function of the thickness of p-type layers and hole concentration for (110) and (100) Ge doping superlattices with $N_D = 1 \times 10^{17} \text{ cm}^{-3}$ and N_A 's are given in the Figure.

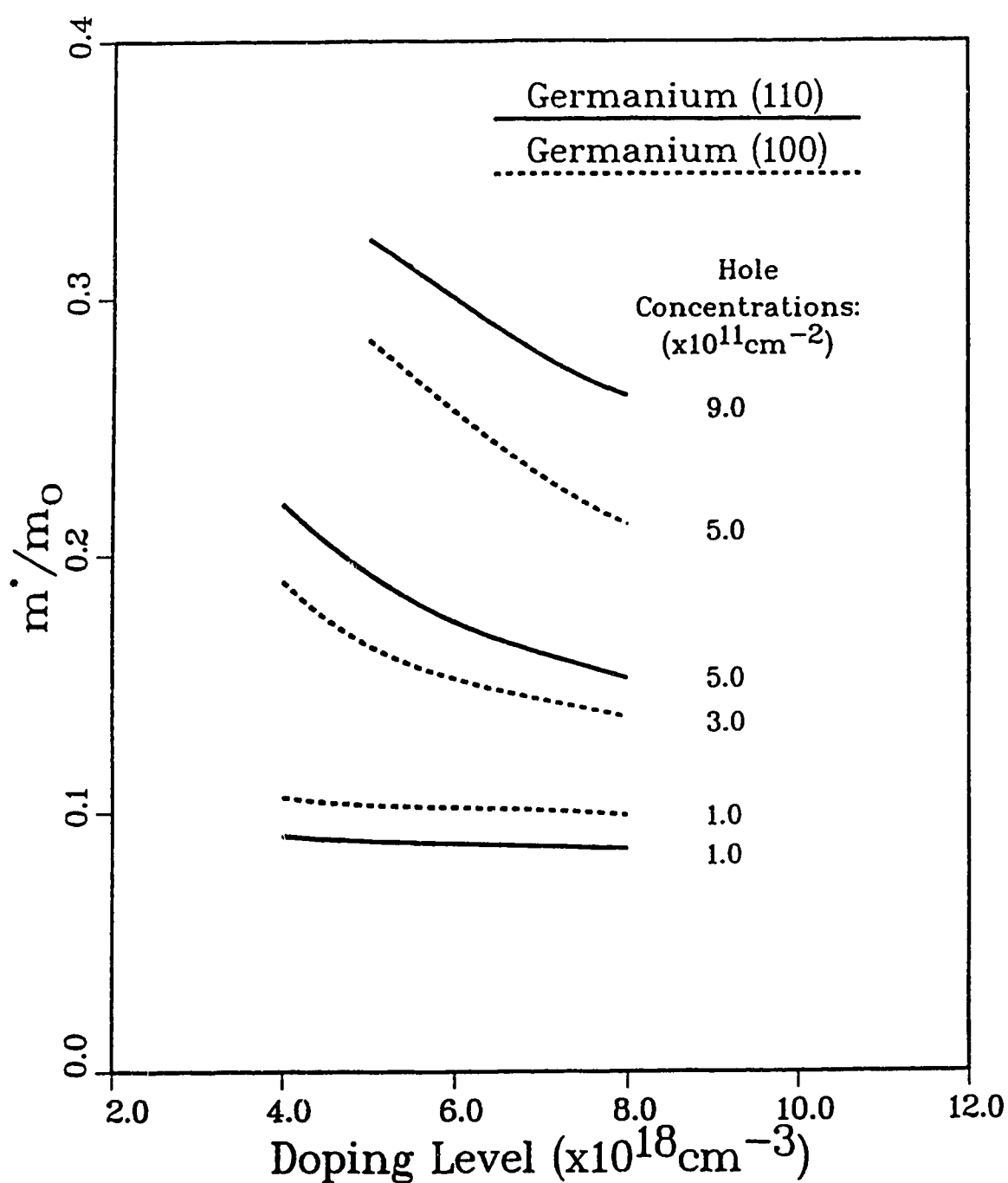


Fig. 6.17 The density-of-states masses of heavy holes of the first subband as a function of the doping level of the p-type layers (N_A) and hole concentration for (110) and (100) Ge doping superlattices with $N_D = 1 \times 10^{17} \text{cm}^{-3}$ and $d_p = 6 \text{ nm}$.

Table 6.2 Density-of-States Masses of the first subband in a (110) Ge doping superlattice with different doping level of the n-type bulk and for two different thicknesses of the p-type layers.

$N_A = 4 \times 10^{18} \text{ cm}^{-3}$		Density-of-States Hole Masses (m^*/m_0)					
Hole Concentration ($\times 10^{11} \text{ cm}^{-2}$)	$d_p = 3 \text{ nm}$			$d_p = 6 \text{ nm}$			
	$N_D (\text{cm}^{-3})$			$N_D (\text{cm}^{-3})$			
	1×10^{16}	1×10^{17}	1×10^{18}	1×10^{16}	1×10^{17}	1×10^{18}	
1.0	0.099	0.099	0.131	0.091	0.091	0.092	
3.0	0.188	0.193	0.302	0.139	0.139	0.145	
5.0	0.305	0.311	0.358	0.219	0.220	0.231	

change of hole mass with n-type doping level is less sensitive. For example, in the case of Si with $N_A = 8 \times 10^{19} \text{ cm}^{-3}$ and $d_p = 2 \text{ nm}$, there are hardly any noticeable changes in the hole masses when N_D varies from $1 \times 10^{19} \text{ cm}^{-3}$ to $1 \times 10^{17} \text{ cm}^{-3}$ and for hole concentrations of 1x, 3x and $5 \times 10^{12} \text{ cm}^{-2}$.

It is to be noted that the hole concentrations indicated for some of the parameters values used in Figures 6.12, 6.13, 6.16 and 6.17 and Table 6.2 may not be physically realisable due to the limit imposed by the breakdown voltage. Nevertheless, these results are useful in illustrating the general characteristics of the masses of holes as functions of the physical parameters of the superlattice. From these results, it can be generally concluded that the product of the doping level and the thickness of the p-type layers, $N_A d_p$, here referred to as the acceptor charge density, plays the dominant role in determining the characteristics of the hole masses. Hole masses generally increase with hole concentrations. When the hole concentration is a small percentage of the acceptor charge density, the hole masses remain independent of the thickness of the p-type layers d_p . This can be explained by the fact that as the computations are carried out at $T = 0^\circ \text{K}$, the self-consistent calculation is sensitive to only a small part of the electric potential, that is to the peak portion of the potential (see Figure 6.6). For a given hole concentration, the shape of this potential is going to remain approximately the same if N_A and d_p are large. Since the hole masses depend on the electric potential and the Fermi energy (which is dependent on the hole concentration) this explains the constant value of hole masses for a given hole concentration at large values of d_p . The values of d_p at which the

hole masses becomes constant for a given hole concentration will greatly depend on the value of N_A as illustrated in Figures 6.12 and 6.16. The smaller N_A is, the larger d_p will be before the hole mass become independent of d_p . As the value of N_A changes, so the shape at the peak of the electric potential changes for a given hole concentration. Hence the hole masses are affected until a point where the hole concentration becomes either such a small or such a large percentage of $N_A d_p$ that the values of the hole masses begin to saturate (see Figure 6.15 for very small value of hole concentration).

The same reasons can be used to explain the effect of the doping level of the n-type bulk on the hole masses. As long as changes in this doping level do not affect the shape of the peak portion of the electric potential, the hole masses will not be affected. Hence, for a large value of $N_A d_p$ and small hole concentration, changes in the doping level of n-type bulk should not affect the hole masses. In general, for a given hole concentration, the hole masses increase as the product $N_A d_p$ decreases, or in other words, as the hole concentration expressed as a percentage of $N_A d_p$ increases.

The above calculations do not include the effect of exchange-correlation energy. This effect, however, is shown to be not significant for the 2-D electron gas in the Si doping superlattice [20]. Moreover, it has been shown that exclusion of the exchange-correlation energy may affect the subband energies but has a smaller influence on the density-of-states masses of the holes, particularly at high hole concentrations [97].

Chapter 7

Conclusions

This project has attained a number of achievements where credits are due to the effort of the many people at the University of Alberta and the Division of Microstructural Science of the National Research Council in Ottawa. The successful fabrication of the Si doping superlattices and the many experimental studies and theoretical computations would not have been possible without this collective effort. I feel privileged to have been one of the participants in this collaboration.

This project began with the self-consistent calculation of electron subband energies in a Si doping superlattice using the effective mass and Hartree approximations. We studied the tunability of the effective bandgap and carrier concentration in pn^+p structures. The tunability of the effective bandgap relates the change in the effective bandgap of a doping superlattice to the change in the external bias. The tunability of the electron concentration relates the capacitance of a p-n layer of the doping superlattice to the capacitance of an equivalent p-n junction in the depletion approximation. For the cases considered here, these tunabilities are almost equal. By self-consistent calculation of the energy levels in the conduction subbands of a Si doping superlattice with narrow (50Å) heavily n-doped and wide (5000Å) lightly p-doped layers, we have shown that the tunability increases with higher values of the planar donor charge density, $N_D d_n$, and decreases with temperature. One problem with this pn^+p structure is that there will be hardly any overlapping of the

electron and hole wavefunctions and therefore experimental measurements of the tunability of the effective bandgap would not be possible. For the case of a doping superlattice with narrow p and n layers, it is expected that the variation of the tunability with temperature and the planar charge density in both the n and p-doped layers will be even greater. Unfortunately for our nipi samples the layer thickness is approximately 1000 Å, too large for the formation of any subbands and hence no meaningful test of these predictions could be carried out.

The exchange-correlation energy in the subbands of Si and GaAs doping superlattices was included in the self-consistent calculations at $T = 0^\circ\text{K}$. The results show that the exchange-correlation term is more important in Si than in GaAs in all three cases (pn^+p , pnpn , nipi) of doping superlattices considered. For the same doping levels, layer thicknesses and electron concentrations, the shift in the lowest subband energy from the value given by the Hartree Approximation is 20-50% greater in Si than in GaAs.

Next, recombination mechanisms of carrier lifetimes were investigated. It was determined that the dominant recombination mechanism is not the tunneling of the carriers through the barriers nor is it the thermionic emission of carriers over the barriers as described by Döhler for GaAs doping superlattices. It is the recombination of carriers by the shunting effect through or around the junctions in defects or in the substrate that is the factor that limits carrier lifetimes in Si doping superlattices. Hence, the carrier lifetime can be estimated by simply taking the product of the junction capacitance and the effective small signal resistance of the nipi

structure. Carrier lifetimes as long as 1.2 s have been observed at $T = 80^\circ\text{K}$. Traps do not seem to influence significantly the carrier lifetime in our Si doping superlattice sample.

We have developed a method using a system of linear functions and Finite Box (Finite Cell) calculations to solve a system of nonlinear second-order differential equations that described a two-dimensional hole system. As our method uses a system of piecewise linear function it is therefore more adaptable to different shapes of electric potential, hence, different two-dimensional structures. We employed a bisection method and linear interpolation to construct the Fermi energy contours and an approximate secant method to hasten the convergence process. Our method allows the Fermi contours to be obtained with enough precision that the hole concentration, as determined from the areas inside the contours, deviates by no more than 0.1% from the prescribed value. The density-of-states mass obtained from the calculated Fermi areas compares favourably with previously published experimental and theoretical results in the MOS inversion layer structure.

The above method of self-consistent calculations was used to determine the density-of-states masses of holes for Si and Ge doping superlattices. Generally, it was determined that the value of the planar acceptor density $N_A d_p$ of the doping superlattice affects the characteristics of the hole masses as a function of hole concentration. However, for large values of N_A ($> 5 \times 10^{19} \text{ cm}^{-3}$ for Si and $> 5 \times 10^{18} \text{ cm}^{-3}$ for Ge) and for moderate or large values of d_p ($> 5 \text{ nm}$) the hole mass characteristics are more affected by the value of N_A . Generally, the hole masses decrease with an increase in N_A for a given hole

concentration. It can also be said that the hole masses increase with hole concentration expressed as a percentage of the acceptor planar density, that is, $p^{(2)}/N_A d_p$. For both the Si and Ge doping superlattice, the hole mass is a more sensitive function of hole concentration for the (100) surface than for the (110) surface orientation. Due to the fact that the calculations were carried out at $T = 0^\circ\text{K}$, very high doping levels of the p-type layers were used to avoid having the acceptors frozen out. As a result, any possible improvement in the mobility of holes at small hole concentrations may be offset by the high scattering effect of the high density of impurity ions. This problem can be somewhat reduced by using a host material with smaller hole mass, such as germanium.

We have developed a simple small signal electrical circuit model to study the AC characteristics. Small signal AC measurements at different frequencies were carried out on reverse biased Si doping superlattices with selective ohmic contacts. The calculated results given by the model were shown to agree well with experiments. Parameters such as capacitance, doping profile and AC conductance of doping superlattices are obtained. It is determined that the choices of the operating frequency and the capacitance meter (serial or parallel) are important when one wishes to determine the values of these parameters. In general, we may conclude that information obtained from the AC measurements of a doping superlattice, in conjunction with a relatively simple lumped parameter model, will help to determine the physical properties and quality of a doping superlattice and its selective contacts.

DLTS measurements were carried out on Si doping superlattice

samples but no conclusive results were drawn. This may be due to the non-exponential capacitance transients, the temperature dependent capture cross sections of the traps and the spatially varying doping profile of the layers which made the analysis of the traps more difficult; it is beyond the scope of this thesis to deal with this problem. Nevertheless, DLTS measurements still remain one of the most reliable methods by which to measure deep traps and the quality of doping superlattice crystals.

Although this thesis deals mainly with Si doping superlattices, much of the results will be applicable to doping superlattices of other semiconductor materials. Conclusions drawn, for example, on the dependency of tunability and the masses of holes on the planar charge density should be, in general, applicable to other kinds of doping superlattices. The small signal circuit model for the analysis of AC characteristics should also be well-suited to other doping superlattices as long as they share similar physical designs.

To summarise, through the team effort of our group, we have managed to study a number of properties of Si doping superlattices. We have successfully fabricated Si doping superlattices with selective contacts using the shadow mask technique. We have studied the tunabilities of the effective bandgap and carrier concentrations, the enhanced optical absorption due to Franz-Keldysh effect for thick layered Si doping superlattice, the effect of the exchange-correlation energy on the subband energies of electrons and we have calculated self-consistently the density-of-states masses of holes using the Kohn-Luttinger Hamiltonian. In addition, we have developed simple electrical circuit models to estimate carrier lifetimes and to study

both the DC and AC characteristics. Although all these may be notable accomplishments in our research work in Si doping superlattices, much remains to be done. Experimental work on the two-dimensional properties of electrons and holes would be an interesting area to explore. Hetero nipi crystals using Si and Ge may be interesting structures to examine. New optical and electrical properties may also be observed in Si doping superlattices with thinner layers and more abrupt doping profiles. Experimental work on Si nipi with sandwiched contacts may help in the studies of these properties.

Reference

1. R. Dingle, IEEE Trans. on Electron Devices, **ED 31**, 1662, 1984.
2. J.J Harris, R.B. Beall, J.B. Clegg, C.T. Foxen, S.J. Batttersby, D.E. Lacklison, G. Duggan and C.M. Hellon, J. Cryst. Growth, **95**, 451, 1989.
3. A.Y. Cho, J. Cryst. Growth, **95**, 1, 1989.
4. L. Esaki, R. Tsu, IBM J. Res. Develop, **61**, 1970.
5. R. Dingle, H.L. Stormer, A.C. Gossard and W. Wiegmann, Appl. Phys. Lett., **33**, 665, 1978.
6. K. Nakagawa and Y. Shiraki, Solid State Comm., **58**, 819, 1986.
7. G. H. Döhler, Advances in Solid State Physics, **XXIII**, 207, 1983.
8. A. Yariv, IEEE Circuits and Devices Magazine, **5**, 25, 1989.
9. S. Luryi, Appl. Phys. Lett., **47**, 1196, 1985.
10. A.L. Lentine, H.S. Hinton, D.A.B. Miller, J.E. Henry, J.E. Cunningham and L.M.F. Chirovsky, IEEE J. Quantum Electron, **25**, 1928, 1989.
11. F. Capasso, W.T. Tsang and G.F. Williams, IEEE Trans. on Electron Devices, **ED 30**, 381, 1983.
12. S. Luryi, IEEE Electron Device Lett., **EDL-7**, 104, 1986.
13. G.H. Döhler, Phys. Stat. Sol. (B), **52**, 79, 1972.
14. K. Ploog, Collected Papers of MBE-CST (Tokyo), **2**, 17, 1982.
15. Y. Shiraki, J. Vac. Sci. Technol., **B**, **3**, 725, 1985.
16. H.G. Schmidt-Weinmar and K.H. Teo, Congress of the Can. Ass. of Phys., Edmonton, Alberta, 1986.
17. E. Wang and H. Huang, Chin.Phys., **6**, 226, 1986.
18. H.G. Schmidt-Weinmar, K.H. Teo, J.N. McMullen and G.H. McKinnon,

- Can. J. Phys., 65, 1064, 1987.
19. C. Priester, G. Allan, M. Lannoo and G. Fishman, Phys. Rev. B, 35, 2904, 1987.
 20. K.H. Teo, G.H. McKinnon, J.N. McMullin and H.G. Schmidt-Weinmar, Superlattices and Microstructures, 4, 275, 1988.
 21. K.H. Teo, W. Allegretto, J.N. McMullin, H.G. Schmidt-Weinmar, Comp. Phys. Comm., in print.
 22. K.H. Teo, W. Allegretto, J.N. McMullin, H.G. Schmidt-Weinmar, Surf. Sci, in print.
 23. D. Landheer, M.W. Denhoff, M. Buchanan, D.C. Houghton, N. Rowell, K.H. Teo, G.H. McKinnon and J.N. McMullin, SPIE, 943, 102, 1988.
 24. J.N. McMullin, G.H. McKinnon, H.G. Schmidt-Weinmar and K.H. Teo, Superlattices and Microstructures, 4, 269, 1988.
 25. G.H. McKinnon, M.Sc. Thesis, University of Alberta, 1988.
 26. G.H. McKinnon, J.N. McMullin, D. Landheer, M. Buchanan, P. Janega and M.W. Denhoff, Can. J. Phys., 67, 326, 1989.
 27. D. Landheer, M.W. Denhoff, M. Buchanan, T.E. Jackman, G.H. McKinnon, K.H. Teo and J.A. Jackman, Appl. Phys. Lett., 52, 910, 1988.
 28. K.H. Teo, J.N. McMullin, F.L. Weichman, H.G. Schmidt-Weinmar, D. Landheer and M.W. Denhoff, J. of Crystal Growth, 95, 486, 1989.
 29. G.A. Leith and S. Zukotynski, Appl. Phys. Lett., 54, 1558, 1989.
 30. E.D. Ahlers and F. G. Allen, Proc. of the 2nd Int. Silicon MBE Symposium, Hawaii, Oct. 1987.
 31. G.H. Döhler, G. Hasnain and J.N. Miller, Appl. Phys. Lett., 49, 704, 1986.
 32. K.H. Teo, J.N. McMullin, D. Landheer, M.W. Denhoff, J. of Appl.

Phys., in print.

33. G.H. Döhler, IEEE J. of Quantum Electronics, QE 22, 1682, 1986.
34. G.H. Döhler, CRC Crit. Rev. in Solid State and Mat. Sci., 13, 97, 1986.
35. R.O. Clark, C. Goradia and D.J. Brinker, Superlattices and Microstructures, 4, 187, 1988.
36. G.H. Döhler, Jap. J. of Appl. Phys. 22, 29, 1983.
37. J. Oswald, G. Bauer, W.C. Goltsoos and A.V. Nurmikko, Superlattices and Microstructures, 4, 159, 1988.
38. K. Ploog, A. Fischer, H. Kunzel, J. Electrochem. Soc., 128, 400, 1981.
39. A.Y. Cho, Appl. Phys. Lett., 19, 467, 1971.
40. L.L. Chang, Handbook of Semiconductors 3, (North-Holland Publ., Amsterdam, 1980) p. 563.
41. D.C. Houghton, D.J. Lockwood, M.W.C. Dharma-Wardana, E.W. Fenton, J.M. Baribeau and M.W. Denhoff, J. Crystal Growth, 81, 434, 1987.
42. P. Zwicknagl, W. Rehm and E. Bauser, J. Electr. Mater., 13, 545, 1984.
43. H. Kinoshita, T. Sakashita and H. Fujiyasu, J. Appl. Phys. 52, 2869, 1981.
44. H. Clemens, J. Crystal Growth, 88, 236, 1988.
45. Y. Yamauchi, K. Uwai, and O. Mikami, Jpn. J. Appl. Phys., 23, L785, 1984.
46. P. Roentgen, K.H. Goetz, h. Beneking, J. Appl. Phys., 58, 1696, 1985.
47. G. H. Döhler, Jpn. J. Appl Phys., 22, Supp 22-1, 29, 1983.
48. P.L. Janega, J. McCaffrey and D. Landheer, Appl Phys. Lett., 55,

- 1415, 1989.
49. H. Kunzel, G.H. Döhler, A. Fischer and K. Ploog, Appl. Phys. Lett., **38**, 171, 1981.
 50. H. Kunzel, A. Fischer and K. Ploog, J. Vac Sci. Technol. **B2(1)**, 1, 1984.
 51. H. Ando, H. Iwamura, H. Ohashi and H. Kanbe, IEEE J. of Quantum Electronics, **25**, 2135, 1989.
 52. G.H. Döhler, H. Kunzel and K. Ploog, Phys. Rev. B., **25**, 2616, 1982.
 53. G.H. Döhler and P. Ruden, Phys. Rev. B, **30**, 5932, 1984.
 54. G.H. Döhler, P. Kiesel, M. Heibmeier, G. Pototzky, P. Riel, SPIE, **943**, 129, 1988.
 55. G.H. Döhler, Superlattices and Microstructures, **1**, 279, 1985.
 56. R.A. Street, G.H. Döhler, J.N. Miller and P.P. Ruden, Phys. Rev. B, **33**, 7043, 1986.
 57. Y. Tokuda, K. Kanamoto, Y. Abe and N. Tsukada, Appl. Phys. Lett. **56**, 227, 1990.
 58. K. Kohler, G.H. Döhler, J.N. Miller and K. Ploog, Superlattices and Microstructures, **2**, 339, 1986.
 59. G.H. Döhler, G. Fasol, T.S. Low, J.N. Miller and K. Ploog, Solid State Commun., **57**, 563, 1986.
 60. G. Fasol, P. Ruden and K. Ploog, J. Phys. C, **17**, 1395, 1984.
 61. E.F. Schubert, A. Fischer, Y. Horikoshi and K. Ploog, Appl. Phys. Lett., **47**, 219, 1985.
 62. B. A. Vojak, G.W. Zajak, F.A. Chambers, J.M. Meese, P.E. Cumbley, R.W. Kaliski, N. Jr. Holonyak and D.W. Nam, Appl. Phys. Lett., **48**, 251, 1986.
 63. D. Landheer, unpublished.

64. S.M. Sze, Physics of Semiconductor Devices, (Wiley, New York, 1981)
p. 92.
65. Ibid. p. 89.
66. C.C. Tin, Ph.D. Thesis, University of Alberta, 1987.
67. S.M. Sze, Physics of Semiconductor Devices, (Wiley, New York, 1981)
p 750.
68. D.V. Lang, J. of Appl. Phys., 45, 3023, 1974.
69. H.H. Berger, Solid State Electron. 15, 145, 1972.
70. M.A. Green and J. Shewchun, Solid State Electron. 17, 941, 1974.
71. Herman E. Maes and Chih-Tang Sah, IEEE Trans. Electron Dev., ED-23,
1131, 1976.
72. D.D. Weiner and J.E. Spina, Sinusoidal Analysis and Modeling of
Weakly Nonlinear Circuit, (Van Nostrand Reinhold Company, New York,
1980) p. 211.
73. A. Broniatowski, A. Blossse, P.C. Srivastawa and J.C. Bourgoin, J.
Appl. Phys. 54, 2907, 1983.
74. S. Zukotynski, private communications.
75. A. Schary and C.A. Lee, J. Appl. Phys., 67, 200, 1990
76. F. Stern and W.E. Howard. Phys. Rev. B 163, 816, 1967.
77. E. Bangert, K.v. Klitzing, G. Landwehr, Proc. of the 12th Conf. on
the Phys. of Semiconductors, Stuttgart, 714, 1974.
78. D.A. Broido and L.J. Sham, Phys. Rev. B, 31, 888, 1985.
79. M. Jaffe, Y. Sekiguchi, J. East and J. Singh, Superlattices and
Microstructures, 4, 395, 1988.
80. K.v. Klitzing and G. Ebert, Springer Series in Solid-State
Sciences, 53, 242, 1984.
81. G.H. Döhler. Surf. Sci. 73, 97, 1978.

82. M. Altarelli. Adv. in Solid State Phys. XXV, 381, 1985.
83. S.M. Sze. Physics of Semiconductor Devices. (Wiley, New York, 1981)
p. 37.
84. T. Ando, A.B. Fowler and F. Stern, Rev. of Modern Phys., 54, 437,
1982.
85. P. Ruden and G.H. Döhler, Phys. Rev. B, 27, 3538, 1983.
86. P. Hohenberg, Phys. Rev., 136, 864, 1964.
87. L.J. Sham and W. Kohn, Phys. Rev., 145, 561, 1966.
88. T. Ando, Phys. Rev. B, 13, 3468, 1976.
89. N.W. Ashcroft and N.D. Mermin, Solid State Physics,
(Philadelphia, 1976: Holt, Rinehart and Winston), p.336.
90. R.K. Kalia, S. DasSarma, M. Nakayama and J.J. Quinn, Phys. Rev. B,
18, 5564, 1978.
91. G. Landwehr and E. Bangert, Springer Series in Solid-State
Sciences 53, 40, 1984.
92. F. J. Ohkawa and U. Uemura, Suppl. of the Prog. of Theoretical
Phys., 57, 164, 1975.
93. R.A. Smith, Semiconductors, 2nd Ed., (Cambridge University Press,
London, 1978) p. 421.
94. E.O. Kane, J. Phys. chem. Solids, 1, 82, 1956.
95. G.D. Mahan, J. Appl. Phys., 51, 2634, 1980.
96. S.M. Sze, Physics of Semiconductor Devices, 2nd Ed., John Wiley &
Sons, 101, 1981.
97. F.J. Ohkawa, J. of the Phys. Soc. Jpn., 41, 120, 1976.

APPENDIX A

A simplified understanding of the small signal AC electrical characteristics of Figure 4.3 can be achieved by analysing the properties of Figure 4.1. In fact if the width W of the superlattice is very small, circuit of Figure 4.1 may be used as a reasonably good approximation for Figure 4.3. The expression for the AC resistances and capacitances of an equivalent serial and parallel circuit of Figure 4.1 can be expressed as follow:

$$R_{si} = \frac{(R_{si} + R_L) + \omega^2 R_{si}^2 R_L^2 C_J^2}{1 + \omega^2 R_L^2 C_J^2} \quad (A1)$$

$$C_{si} = \frac{1 + \omega^2 R_L^2 C_J^2}{\omega^2 R_L^2 C_J^2} \quad (A2)$$

$$R_{pa} = \frac{(R_{si} + R_L)^2 + \omega^2 R_{si}^2 R_L^2 C_J^2}{(R_{si} + R_L) + \omega^2 R_{si}^2 R_L^2 C_J^2} \quad (A3)$$

$$C_{pa} = \frac{R_L^2 C_J^2}{(R_{si} + R_L)^2 + \omega^2 R_{si}^2 R_L^2 C_J^2} \quad (A4)$$

where R_{si} , C_{si} , R_{pa} , C_{pa} are the serial AC resistance and capacitance, and parallel AC resistance and capacitance, respectively. The 3 dB frequencies for each may be obtained from (A1) to (A4) respectively.

Appendix B

The Hamiltonian of (6.1) for the (100) surface orientation is given by

$$H(k_x, k_y, k_z) = \begin{bmatrix} H_{kp} & 0 \\ 0 & H_{kp} \end{bmatrix} + H_B, \quad (B1)$$

where

$$H_{kp} = \begin{bmatrix} H_1 & R & S \\ R & H_2 & T \\ S & T & H_3 \end{bmatrix}, \quad (B2)$$

$$H_B = -\frac{\Delta}{3} \begin{bmatrix} 1 & j & 0 & 0 & 0 & -1 \\ -j & 1 & 0 & 0 & 0 & j \\ 0 & 0 & 1 & 1 & -j & 0 \\ 0 & 0 & 1 & 1 & -j & 0 \\ 0 & 0 & j & j & 1 & 0 \\ -1 & -j & 0 & 0 & 0 & 1 \end{bmatrix} \quad (B3)$$

and

$$\begin{aligned} H_1 &= Lk_x^2 + M(k_y^2 + k_z^2) & R &= Nk_x k_y \\ H_2 &= Lk_y^2 + M(k_z^2 + k_x^2) & S &= Nk_x k_z \\ H_3 &= Mk_z^2 + M(k_x^2 + k_y^2) & T &= Nk_y k_z \end{aligned}$$

The values for L, M and N for Si are -6.5, -2.7, -7.3 [77], respectively, and Δ is taken to be 44 meV.

Vitae

Name: TEO, KOON HOO

Date and Place of Birth: Nov. 29, 1953, Singapore

Address: NovAtel Communications Ltd.
1020 - 64th Avenue N.E.,
Calgary Alberta, Canada T2E 7V8
Tel. no.: (403) 295-4500

EDUCATION

B.Sc. (Hons) in Telecommunication Engineering, June, 1978 University of Essex, Essex, United Kingdom.

M.Sc. (with thesis) in Electrical Engineering, Dec., 1984, University of Alberta, Edmonton, Canada. Major: Fiber Optic Communications.

Ph.D. in Electrical Engineering, June, 1990, University of Alberta, Edmonton, Canada. Major: Semiconductor Superlattices.

AWARDS

Izaak Walton Killam Memorial Scholarship, 1988 - 1990

Andrew Stewart Graduate Prize, 1987.

PROFESSIONAL EXPERIENCE

Industries

Fairchild Singapore Ltd., Singapore. (July, 1978 - Feb., 1979):
Product Engineer

Ministry of Defence. (Feb., 1979 - Aug., 1979):
Radio Communications Engineer

Teaching

Singapore Polytechnic, Singapore. (Dec., 1979 - Sept., 1982):
Lecturer: i) Courses Taught: Communications Engineering, Digital Computer Fundamentals & Electronics.
ii) Projects Supervised: Data Communications, Digital Filters & Microprocessor Applications.

University of Alberta, Canada (Sept. 1982 - April, 1988):

- i) Course Marker and Lab Assistant: Communication in Noise, Electronics II & III, Electromagnetics, Physics & Network.
- ii) Sessional Lecturer: Communication Systems (EE489)

Research and Development

Microstrip Technology (Oct., 1977 - June, 1978)

Measured relative permittivity and dielectric loss of Rexolite and Fibreglass using microstrip configurations. Designed and measured E- and H-fields of microstrip log periodic antennas for frequency range of 2 - 4 GHz.

Telecommunications (May, 1983 - Dec., 1984)

Modified the design of and studied the error mechanisms in an experimental four-level PWM communication system. Designed a clock recovery unit using a phase-locked loop. Measured and calculated the effect of clock jitter on the system bit error rate.

Semiconductor Doping Superlattices (May, 1985 - Jan, 1990)

Developed computer programs to study the two-dimensional properties of electron and hole carriers. Determined absorption coefficient and measured carrier lifetimes as functions of temperature and external bias using photoconductivity method. Developed simple electrical circuit models to estimate carrier lifetimes and to study AC characteristics. Measured AC and DC characteristics. Involved in the design of shadow-mask and photo-masks for fabricating the semiconductor superlattices. Measured traps with Deep Level Transient Spectroscopy technique.

Opto-electronics (Jan, 1987 - Dec, 1988)

Designed a high speed receiver using Ge APD for photon detection and studied the effects of traps on Ge APD recovery time.

Administration

Member of Department (Singapore Polytechnic, E.E.) Curriculum Committee.

Member of Singapore Polytechnic Computer Studies Committee.

Member of Department (U. of A., E.E.) Graduate Studies Standing Committee.

LIST OF REFEREED PUBLICATIONS

1. K.H. Teo, J.N. McMullin, D. Landheer and M.W. Denhoff, "Small Signal AC Analysis of a Silicon Doping Superlattice under Reverse Bias", *Journal of Applied Physics*, in print.
2. K.H. Teo, W. Allegretto, J.N. McMullin and H.G. Schmidt-Weinmar, "Theoretical Calculation of the Properties of Two-Dimensional Holes in Doping Superlattices", *Surface Science*, in print.
3. K.H. Teo, W. Allegretto, J.N. McMullin and H.G. Schmidt-Weinmar, "Self-Consistent Calculation of the Density-of-States Mass of Holes on 2-D Silicon Structures", *Computer Phys. Communications*, in print.
4. K.H. Teo, J.N. McMullin, F. L. Weichman, H.G. Schmidt-Weinmar, D. Landheer and M.W. Denhoff, "Measurement and Mechanism of Free Carrier Recombination in a Silicon Doping Superlattice" *The Journal of Crystal Growth*, Vol. 95, pp. 486-489, 1989.
5. K.H. Teo, C.G. Englefield and P.A. Goud, "Bit Error Rate in a Four-Level Pulse-Width-Modulated Fiber-Optic System Using a Phase-Locked Loop for Clock Recovery, *Proceedings of the International Conference on Communications Systems (ICCS '88)*, Paper 22.4, Singapore, Oct. 31 - Nov. 3, pp. 22.6.1-22.6.4, 1988.
6. K.H. Teo, C.G. Englefield and P.A. Goud, "Optimisation of a Phase-Locked Loop for Clock Recovery in a Pulse-Width-Modulated Fiber-Optic System, *Proceedings of the Fourteenth Biennial Symposium on Communications*, Paper C.3, Queen's University, Kingston, May 29 - June 1, pp. C.3.5-C.3.8, 1988.
7. K.H. Teo, G.H. McKinnon, J.N. McMullin and H.G. Schmidt-Weinmar, "Exchange-Correlation Energy in the Subbands of Silicon Doping Superlattices", *Superlattices and Microstructures*, Vol. 4, No. 3, pp. 275-279, 1988.
8. J.N. McMullin, G.H. McKinnon, H.G. Schmidt-Weinmar and K.H. Teo, "Optical Absorption in a Silicon Doping Superlattice", *Superlattices and Microstructures*, Vol. 4, No. 3, pp. 269-273, 1988.
9. D. Landheer, M.W. Denhoff, M. Buchanan, T.E. Jackman, G.H. McKinnon, K.H. Teo and J.A. Jackman, "Enhancement of Carrier Lifetime in Silicon Doping Superlattices", *Applied Physics Letters*, Vol 52, pp. 910-912, 1988.
10. D. Landheer, M.W. Denhoff, M. Buchanan, D.C. Houghton, N. Rowell, K.H. Teo, G.H. McKinnon and J.N. McMullin, "Analysis of Doping Superlattices grown by Si MBE", *SPIE*, Vol. 943, pp 102-106, 1988.
11. K.H. Teo, C.G. Englefield, P.A. Goud and X.D. Dai, "Error Mechanisms in a Four-Level Pulse Width Modulated Optical Fibre System", *Canadian Electrical Engineering Journal*, Vol. 12, No. 4, pp. 142-146, Oct., 1987.
12. H.G. Schmidt-Weinmar, K.H. Teo, J.N. McMullin and G.H. McKinnon, "Tuning the Effective Bandgap of a Silicon Doping Superlattice", *Canadian Journal of Physics*, Vol. 65, pp. 1064-1068, Aug., 1987.

NON-REFEREED PUBLICATION

1. H.G. Schmidt-Weinmar and K.H. Teo, "Quasi Two-Dimensional Electron Gas in a NIPI Superlattice", *Congress of the Canadian Association of Physicists*, Edmonton, Alberta, June, 1986.